

Dust Properties of Comets Observed by Spitzer

DAVID E. HARKER ¹, DIANE H. WOODEN ², MICHAEL S. P. KELLEY ³, AND CHARLES E. WOODWARD ⁴

¹*Center for Astrophysics and Space Sciences, University of California, San Diego, 9500 Gilman Drive, La Jolla, CA 92093-0424, USA*

²*NASA Ames Research Center, Space Science Division, MS 245-1, Moffett Field, CA 94035-1000, USA*

³*University of Maryland, Department of Astronomy, 4254 Stadium Dr, College Park, MD 20742-2421, USA*

⁴*Minnesota Institute for Astrophysics, School of Physics and Astronomy, 116 Church Street, S.E., University of Minnesota, Minneapolis, MN 55455, USA*

(Received 2023-06-12; Revised 2023-09-24; Accepted 2023-09-26)

Submitted to To Appear in The Planetary Science Journal

ABSTRACT

As comets journey into the inner solar system, they deliver particulates and volatile gases into their comae that reveal the most primitive materials in the solar system. Cometary dust particles provide crucial information for assessing the physico-chemical conditions in the outer disk from which they formed. Compared to the volatiles and soluble organics, the refractory dust particles are more robust and may be traceable to other small bodies. Using data from the Spitzer Heritage Archive, we present thermal dust models of 57 observations of 33 comets observed spectroscopically with the NASA Spitzer Space Telescope. This comet spectral survey offers the opportunity to study comets with data from the same instrument, reduced by the same methods, and fitted by the same thermal model using the same optical constants. The submicron dust tends to be dominated by amorphous carbon, and the submicron silicate mass tends to be dominated by amorphous silicate materials. We discuss the implications of these findings as they relate to Mg-rich crystalline silicates, which are high-temperature condensates, as well as to potential ion irradiation of amorphous Mg:Fe silicates prior to their incorporation into comets. These results impact our understandings of the protoplanetary disk conditions of planetesimal formation. Lastly, we cannot definitively conclude that a distinct difference exists in the dust composition between Oort cloud and Jupiter-family comet dynamical population as a whole.

Keywords: Long period comets (933), Short period comets (1452), Comet origins (2203), Dust composition (2271), Infrared spectroscopy (2285)

1. INTRODUCTION

Solar system formation is an engine that simultaneously preserves and transforms interstellar (ISM) dust grains into planetesimals and, ultimately, planets. Being a mixture of ISM dust and solar nebula processed material, comets allow us to investigate both the inputs and outputs of dust transformation in the young solar system. Dust grains in the ISM are dominated by “amorphous” silicates, i.e., they have chemical composition (stoichiometry) similar to pyroxene ($[\text{Mg}_x, \text{Fe}_{1-x}] \text{SiO}_3$) and olivine ($[\text{Mg}_y, \text{Fe}_{1-y}]_2 \text{SiO}_4$). Studies of silicates in the galaxy measured the silicate crystalline fraction to be $f_{\text{cryst}} \leq 5\%$ by mass in the ISM (Kemper et al. 2004). In contrast, dust ejected by comets, such as

C/1995 O1 (Hale-Bopp) and 9P/Tempel 1, have significant crystalline mass fractions, both near 30% (Harker et al. 2007, 2005; Woodward et al. 2021). Moreover, laboratory studies of GEMS (glass with embedded metal and sulfides), an abundant amorphous silicate material in interplanetary dust particles thought to be derived from comets, have isotopic composition indicative of formation the protosolar nebula (Keller & Messenger 2011). They also have elemental compositions and lower densities that make them candidates of processed ISM silicates (Bradley et al. 2022). In aggregate, observations of ISM and of comets strongly suggest that ISM amorphous silicates were extant in the icy outer-disk as well as were destroyed and re-condensed as Mg-rich crystals in the inner protoplanetary disk, or annealed, prior to accretion of comets in the icy outer-disk. Thus, determination of comet dust characteristics enables deeper understanding of a) how dust was processed in the inner-solar system, and b) how that

dust was transported to the outer-solar system; processes that are apparently ubiquitous in observations of external protoplanetary disks (e.g., Olofsson et al. 2010; Kóspál et al. 2023).

Common taxonomy schemes are based on the abundances of primary volatiles (water, CO₂, methanol, ethane, etc.; Mumma et al. 2011), molecular daughter species (C₂, CN, etc.; A’Hearn et al. 1995; Dello Russo et al. 2016; Bockelée-Morvan & Biver 2017; Lippi et al. 2021), or the physical properties of molecules (isotopic ratios, atomic spin states; Busemann et al. 2009; Bonev et al. 2007). However, a dust based taxonomy utilizes species that are resistant to chemical alteration up to at least the melting point of water, and complements studies of the more volatiles species. Development of a comet dust taxonomy classification could provide a powerful constraint for solar system formation scenarios more robust than any conclusion based on derived inferences from a single taxonomy in isolation. For example, identification of a relationship between organic D-to-H ratios and silicate dust crystallinity (f_{cryst}) may delineate the location and epoch in the disk evolution during which different comet nuclei formed (Busemann et al. 2009).

In this paper, we investigate the dust characteristics of comets uniformly observed with the same platform, the NASA Spitzer Space Telescope (hereafter Spitzer, Werner et al. 2004), with the goal to assess whether classification of comets into dynamical families is possible using dust taxonomy. A companion manuscript explores deeper nuances of the statistical, machine-learning methodology and interpretations. This spectroscopic survey of comets presented herein serves as a guide to potential JWST studies, although the total number of JWST-observed comets to date does not yet eclipse those observed by Spitzer.

2. ARCHIVAL SELECTION

Grain characteristics of dust in comet comae can be determined from moderate resolution IR spectroscopy covering wavelength ranges from 8.0 to 28 μm where broad and narrow band features from mineral solid state resonances occur (Engrand et al. 2023; Wooden et al. 2017). These materials are lofted into the coma from nuclei surface regions through sublimation, volatile out gassing, and other processes. Within the Spitzer Heritage Archive¹ lies a substantial set of comet observations from which one can construct a sample of objects to study.

Comets selected for analysis in this manuscript were observed with the Spitzer Infrared Spectrograph (IRS; Houck et al. 2004) using the short-wavelength low-resolution (SL) and long-wavelength low-resolution (LL) modules ($\Delta\lambda/\lambda \sim 64\text{--}128$). The short-low modules cover 5.1–

14.3 μm , split between two separately observed spectral regions named SL2 (covering 5.1–7.6 μm) and SL1 (covering 7.4–14.3 μm). The long-low modules cover 13.9–39.9 μm , similarly named LL2 (covering 13.9–21.3 μm), and LL1 (covering 19.9–39.9 μm). Each spectral region is observed separately through its own entrance slit: 3''6×17'' and 3''7×17'' for SL2 and SL1, respectively, and 10.5''×52'' and 10.7''×52'' for LL2 and LL1, respectively.

We use the work of Kelley et al. (2021) as the basis for our analysis. They presented a uniform reduction of 57 observations of 33 comets. Their methodology is detailed in the data set documentation, as described in the NASA PDS Small Bodies Node.² In summary, observations were: (a) background subtracted; (b) spectra extracted from individual exposures using constant width aperture sizes; (c) exposures were combined with outlier rejection; (d) spectra were cleaned for bad data (e.g., radiation hits, and the scattered light artifact at 14- μm); (e) a model nucleus subtracted when possible; (f) spectral order-to-order discontinuities removed by scaling orders as needed; and (g) a 1.8% relative calibration uncertainty was added in quadrature. Three aspects of the reduction present potential issues for spectral analysis: (1) corrections for spectral fringing were not attempted for these data, and fringing will be most apparent at 21 to 25 μm ; (2) the edges of some spectral orders were trimmed to avoid potentially unphysical features in regions most likely to be affected by data calibration or background subtraction issues, and the trimmed data tends to vary by observation; (3) as a consequence of the spectral trimming, the order-to-order scaling near 19 to 22 μm could potentially remove or enhance real spectral structure present in cometary data. Details on these points and all aspects of the data selection and reduction are given in the archive documentation (Kelley et al. 2021).

We have significantly improved reductions for four comets. Here, comets 17P/Holmes and C/2003 K4 on 2005 September 13 have improved background removals, and comet C/2003 T4 on 2006 January 29 has an improved SL to LL scaling. The archive will be updated accordingly (Kelley et al. in prep.). Table 1 lists the observational summary of each spectrum analyzed in this work including the comet name, UT date, the heliocentric (r_h) and geocentric (Δ) distances, and phase angle of the observations. Not every comet observation in our sample covers both the short-low (SL) and long-low (LL) modules. In Section 4.2, we discuss the model fits in relation to the different wavelength coverage between spectra of a given comet and the ensemble of the survey comets.

² <https://pdssbn.astro.umd.edu/holdings/pds4-spitzer:spitzer-spec-comet-v1.0/SUPPORT/dataset.shtml>.

¹ <https://irsa.ipac.caltech.edu/Missions/spitzer.html>

Table 1. Spitzer IRS observational summary

Comet	Date	Start time ^a	End time ^b	Module	r_h	Δ	Phase
	(UTC)	(hr:min:sec)	(hr:min:sec)				
6P/d'Arrest	2008 Sep 12	07:05:47	07:41:54	SL2 SL1	1.392	0.596	41.5
8P/Tuttle	2007 Nov 02	18:11:18	18:18:33	SL2 SL1 LL2 LL1	1.606	1.322	39.4
9P/Tempel 1	2005 Jul 02	12:22:18	13:19:35	SL2 SL1 LL2 LL1	1.506	0.711	35.8
9P/Tempel 1	2005 Jul 03	06:48:18	07:47:29	SL2 SL1 LL2 LL1	1.506	0.714	36.0
17P/Holmes	2007 Nov 10	19:51:12	20:16:06	SL2 SL1 LL2 LL1	2.505	1.867	21.3
21P/Giacobini-Zinner	2005 Dec 18	20:18:04	21:12:09	SL2 SL1 LL2 LL1	2.292	1.907	25.9
29P/Schwassmann-Wachmann 1	2003 Nov 23	07:17:55	07:25:05	... SL1 LL2 LL1	5.734	5.540	10.1
37P/Forbes	2005 Oct 14	15:11:40	16:09:38	SL2 SL1 LL2 LL1	1.735	1.185	35.0
41P/Tuttle-Giacobini-Kresák	2006 Apr 18	02:13:37	02:24:02	SL2 SL1	1.275	0.866	51.8
46P/Wirtanen	2007 Dec 08	11:44:10	11:48:25	SL2 SL1	1.290	0.585	50.0
46P/Wirtanen	2008 Jan 17	20:41:48	20:45:11	SL2 SL1	1.078	0.446	69.1
46P/Wirtanen	2008 Apr 24	15:27:14	15:41:21	SL2 SL1 LL2 LL1	1.494	0.807	39.0
46P/Wirtanen	2008 May 24	01:26:01	03:05:22	SL2 SL1 LL2 LL1	1.742	1.227	34.5
46P/Wirtanen	2008 Jul 02	13:08:13	14:36:56	... SL1 LL2 LL1	2.076	1.912	29.1
48P/Johnson	2004 Oct 04	14:47:42	15:01:34	... SL1 LL2 LL1	2.311	1.740	24.4
62P/Tsuchinshan 1	2005 Feb 13	08:38:28	08:43:34	SL2 SL1	1.650	0.921	32.4
65P/Gunn	2004 Aug 10	15:53:16	16:09:31	... SL1 LL2 LL1	3.478	3.003	16.1
67P/Churyumov-Gerasimenko	2008 Jun 29	19:41:18	20:05:08 LL2 LL1	2.784	2.492	21.3
67P/Churyumov-Gerasimenko	2008 Nov 28	09:03:56	09:57:57	SL2 SL1 LL2 LL1	1.652	1.005	35.7
67P/Churyumov-Gerasimenko	2008 Nov 29	02:36:16	03:30:17	SL2 SL1 LL2 LL1	1.647	1.006	35.9
67P/Churyumov-Gerasimenko	2008 Nov 29	16:49:13	17:43:13	SL2 SL1 LL2 LL1	1.643	1.007	36.1
67P/Churyumov-Gerasimenko	2008 Nov 30	11:41:08	12:35:09	SL2 SL1 LL2 LL1	1.637	1.008	36.4
71P/Clark	2006 May 27	13:29:37	14:41:21	SL2 SL1 LL2 LL1	1.566	0.910	37.6
73P/Schwassmann-Wachmann 3 B	2006 Apr 17	14:07:47	14:32:37	SL2 SL1	1.192	0.441	54.8
73P/Schwassmann-Wachmann 3 B	2006 Aug 06	04:14:47	07:09:09	SL2 SL1 LL2 LL1	1.259	0.846	53.9
73P/Schwassmann-Wachmann 3 C	2006 Mar 17	00:58:00	01:22:50	SL2 SL1	1.466	0.784	40.0
73P/Schwassmann-Wachmann 3 C	2006 Aug 06	01:14:07	01:52:14	SL2 SL1	1.267	0.864	53.4
78P/Gehrels 2	2004 Sep 01	14:22:55	14:36:45	... SL1 LL2 LL1	2.059	1.531	28.6
88P/Howell	2004 Sep 01	14:47:34	15:01:26	... SL1 LL2 LL1	1.996	1.391	28.7
105P/Singer Brewster	2005 Jul 14	13:37:52	13:51:26	... SL1	2.091	1.918	29.1
121P/Shoemaker-Holt 2	2005 Apr 22	22:16:45	22:23:26	... SL1	2.989	2.357	17.0
123P/West-Hartley	2004 Feb 04	08:00:33	08:04:28 LL2 LL1	2.176	1.600	25.2
132P/Helin-Roman-Alu 2	2005 Nov 20	03:18:28	04:16:28	SL2 SL1 LL2 LL1	2.074	1.480	27.3
144P/Kushida	2008 Dec 06	05:56:00	06:48:03	SL2 SL1	1.552	0.827	36.9
C/2001 Q4 (NEAT)	2004 Oct 23	09:21:43	09:26:54	SL2 SL1	2.622	2.528	22.7
C/2003 K4 (LINEAR)	2004 Jul 16	05:01:23	05:06:33	SL2 SL1	1.760	1.409	35.4
C/2003 K4 (LINEAR)	2005 Sep 13	06:01:33	06:59:49	... SL1 LL2 LL1	4.501	4.283	13.1
C/2003 T3 (Tabur)	2005 Jan 11	18:04:17	18:27:57	... SL1 LL2 LL1	3.560	2.961	14.3
C/2003 T4 (LINEAR)	2005 Nov 22	17:29:15	19:14:02	... SL1 LL2 LL1	3.514	3.265	16.7
C/2003 T4 (LINEAR)	2006 Jan 29	19:56:50	21:08:35	... SL1 LL2 LL1	4.257	3.774	12.6
C/2003 T4 (LINEAR)	2006 Mar 07	07:18:09	07:48:34 LL2 LL1	4.636	4.385	12.4
C/2004 B1 (LINEAR)	2005 Oct 15	05:35:43	06:27:38	SL2 SL1	2.210	2.031	27.5

Table 1 continued

Table 1 (*continued*)

Comet	Date	Start time ^a	End time ^b	Module	r_h	Δ	Phase
	(UTC)	(hr:min:sec)	(hr:min:sec)				
C/2004 B1 (LINEAR)	2006 May 16	05:34:25	05:45:32	SL2 SL1	2.058	1.608	28.7
C/2004 B1 (LINEAR)	2006 Jul 26	03:51:11	05:07:13	... SL1 LL2 LL1	2.689	2.234	21.5
C/2004 B1 (LINEAR)	2007 Mar 08	08:19:30	09:24:57	... SL1 LL2 LL1	4.814	4.766	12.0
C/2004 B1 (LINEAR)	2007 Jun 09	20:14:04	21:44:38 LL2 LL1	5.643	5.395	10.2
C/2004 Q2 (Machholz)	2005 Jul 01	07:52:33	08:05:48	SL2 SL1	2.547	2.297	23.6
C/2006 P1 (McNaught)	2007 May 04	19:58:18	20:17:35	SL2 SL1 LL2 LL1	2.398	2.224	24.8
C/2006 P1 (McNaught)	2007 Aug 02	17:01:50	19:32:18	SL2 SL1 LL2 LL1	3.624	3.137	15.3
C/2006 P1 (McNaught)	2007 Sep 06	07:41:38	10:22:07	... SL1 LL2 LL1	4.044	3.849	14.7
C/2006 Q1 (McNaught)	2007 Mar 22	02:05:15	03:30:47 LL2 LL1	5.279	5.174	10.9
C/2006 Q1 (McNaught)	2008 Jan 17	14:30:12	15:10:15	... SL1 LL2 LL1	3.253	3.214	18.0
C/2006 Q1 (McNaught)	2008 Feb 25	07:56:36	08:01:45	... SL1	3.066	2.673	18.6
C/2006 Q1 (McNaught)	2008 Jul 02	02:41:55	02:54:30	SL2 SL1 LL2 LL1	2.764	2.375	21.1
C/2006 Q1 (McNaught)	2008 Jul 09	16:50:43	17:31:30	SL2 SL1	2.764	2.475	21.5
C/2007 N3 (Lulin)	2008 Oct 04	06:45:36	07:40:09	SL2 SL1	1.901	1.673	32.6
C/2008 T2 (Cardinal)	2009 Apr 04	08:25:04	09:25:08	SL2 SL1 LL2 LL1	1.607	1.088	37.9

^a Start time of integration.

^b End time of integration.

3. THERMAL DUST MODEL

Derivations of comae dust properties are achieved by computing and fitting thermal models to observed IR spectral energy distributions (SEDs, Harker et al. 2007, 2011; Engrand et al. 2023, see sections 2.5.1-2.5.5). Dust properties include the relative mass fractions of five primary dust compositions: amorphous Mg:Fe olivine (ao50), amorphous Mg:Fe pyroxene (ap50), Mg-rich crystalline olivine (forsterite, co), Mg-rich crystalline pyroxene (enstatite, cp), and amorphous carbon (ac), as well as the particle differential size distribution parameters and the particle porosity (Harker et al. 2002, 2004; Wooden et al. 2004; Harker et al. 2007, 2011; Woodward et al. 2021).

3.1. Dust Composition

The dust composition used in thermal models is derived from laboratory studies of interplanetary dust particles (IDPs, Wooden et al. 2000), micrometeorites (Bradley et al. 1999), the NASA Stardust mission (Brownlee et al. 2006) and other remote sensing modeling efforts (e.g., Hanner et al. 1994; Harker et al. 2002; Wooden et al. 2004). Our selection of basic dust grain components is consistent with the major mineral groups used by other modelers to generate synthetic SEDs arising from dust thermal emission in the 10 μm region (Min et al. 2005; Sugita et al. 2005; Lisse et al. 2006; Werner et al. 2006). Amorphous silicates with chemical composition (stiochiometry) similar to olivine ($\text{Mg}_y\text{Fe}_{(1-y)}\text{SiO}_4$ and pyroxene ($\text{Mg}_x\text{Fe}_{(1-x)}\text{SiO}_3$ with $x = y = 0.5$ (i.e.,

$\text{Mg}/(\text{Mg}+\text{Fe}) = 0.5$) reproduce the broad width of the 10 μm feature. Mg-rich orthopyroxene is detected through its 9.3 and 10.5 μm features (Wooden et al. 1999; Harker et al. 2002). Mg-rich crystalline olivine is uniquely identified through its distinct, relatively narrow 11.2 μm silicate feature (Hanner et al. 1994). Mg-rich crystalline species are defined as grains with a stoichiometry of $0.9 \leq x \lesssim 1.0$ ($\text{Mg}/(\text{Mg}+\text{Fe}) = 0.9$) (Chihara et al. 2002; Koike et al. 2003; Wooden 2008; Wooden et al. 2017).

The model does not include grain species that have either not been well constrained through remote sensing, or are found only through laboratory analyses. Several species thought to possibly exist within comets do not have detected spectral signatures in the mid-IR region in order to be adequately constrained through thermal emission modeling. Such species are found in significant amounts through the laboratory analysis of Stardust return samples (Brownlee 2014), interplanetary dust particles (IDPs) (Zolensky & Barrett 1994; Brownlee & Joswiak 2017), and ultra-carbonaceous micro-meteorites (UCAMMs) (Dobrică et al. 2012). They include metal sulfides (e.g., submicron sized FeS grains which produce a broad 23 μm feature), refractory organics found in cometary IDPs (Matrajt et al. 2005) with features between 3.3–3.6 μm and Fe-rich crystalline olivine ($\text{Fe}/(\text{Mg}+\text{Fe}) > 90$ to $\text{Fe}/(\text{Mg}+\text{Fe}) \approx 50$) which produce a distinct feature at 11.35–11.4 μm as well as features in the mid-infrared, all of which are shifted to wavelengths longer than those produced by Mg-rich crystalline olivine.

A similar argument is made for species detected in trace amounts in laboratory spectra, including Mg-carbonates, PAHs, and Fe metal: spectral features from Mg-carbonates and polycyclic aromatic hydrocarbons (PAHs) have not been detected incontrovertibly and Fe metal is featureless. Lastly, phyllosilicates are not detected in laboratory examinations of Stardust return samples and their stronger broad far-infrared features are not centered at the wavelengths of observed resonances.

Comparing various techniques to thermal emission modeling of cometary IR spectral energy distributions (SEDs) shows that different approaches applied to the same comet yield the same composition, i.e., the same relative abundances of the primary grain components, as long as the same range of particle sizes are employed. Small grains tend to dominate the resonant features and the short wavelength spectral flux whereas the mass is dominated by the larger grains. Generally, a size distribution from 0.1–100 μm is considered because grains larger than 100 μm are presumed to not contribute significantly to Spitzer IRS spectra. However, this interpretation is a consequence of the use of Mie theory in the model.

Recent observations of comet 67P/Churyumov-Gersimenko with the Rosetta spacecraft show a phase effect in the thermal emission from dust indicating that large dust grains can support a thermal gradient (Bockelée-Morvan et al. 2019), and may be hotter and thereby brighter, than the isothermal temperatures assumed in the model. The relative abundances of grain components derived from thermal emission models of cometary comae, which compute composition-dependent radiative equilibrium temperatures, yield similar compositions for the same comet for the major species that include olivine and pyroxene, and a dark absorbing carbonaceous grain material. However, challenges in outcomes and interpretations arise when inter-comparing models that use considerably different maximum grain sizes in their size distributions, $n(a)da$, or when grain temperatures are modified by highly absorptive coatings. The relative abundances of the grain components depend on their relative temperatures, and in turn, on the optical constants employed in the calculations. Our methods and optical constants are carefully documented so that our results can be clearly compared to those of other investigators.

3.2. Absorption Efficiency

A grain’s composition, mineral structure (crystalline or amorphous), porosity, and radius determine its absorption and emission efficiency, Q_{abs} (a grain’s absorption efficiency and emission efficiency are equivalent at any given wavelength by Kirchoff’s Law). The model assumes individual porous grains having a single mineral composition (i.e., no mixtures of carbon and silicate). Mie theory combined

with effective medium approximation is sufficient to calculate Q_{abs} for amorphous porous grains (Bruggeman mixing formula; Bohren & Huffman 1983). Amorphous porous grains are modeled with an increasing vacuous content as expected for hierarchical aggregation, using the fractal porosity prescription or fractional filled volume given by $f = 1 - (a/0.1 \mu\text{m})^{D-3}$ with the fractal dimension parameter D ranging from $D = 3$ (solid) to $D = 2.5$ (fractal porous but still spherical enough to be within the applicability of Mie scattering computations; Harker et al. 2002). Grain porosity is a critical parameter that uniquely affects the observed spectra from comets (Wooden 2008; Lindsay et al. 2013; Güttler et al. 2019). A large porous grain and a small compact grain of the same composition can have the same temperature. A size distribution of porous grains compared to compact grains produces enhanced emission at longer wavelengths while producing the silicate emission features. Hence, the shape of the observed spectrum constrains the porosity and slope of the grain size distribution of amorphous grains.

Crystals, however, are not well modeled by Mie Theory nor by mixing theory because of their anisotropic optical constants and irregular shapes. Discrete solid crystals from 0.1–1 μm in radius are considered in the coma, since crystals of larger sizes do not fit the observed SEDs. Discrete solid crystals are better computed using the continuous distribution of ellipsoids (CDE) approach (Harker et al. 2007) or discrete dipole approximation (DDA; Lindsay et al. 2013). CDE reasonably reproduces laboratory spectra of crystalline powders and is a good starting point for our models (Fabian et al. 2001).

3.3. Grain-size Distribution

For each grain, its flux density emitted at the heliocentric distance (r_h [au]) of the comet at the time of observation is the product of Q_{abs} with a Planck function evaluated at the radiative equilibrium temperature T_d of the dust grain, $B_\lambda(T_d)$. The total flux from a particular mineral species is calculated by integrating over the grain size distribution. The differential grain size distribution we use in the model is the Hanner modified power law (hereafter HGSD; Hanner et al. 1994) in which the relative number of each grain size is computed from: $n(a) = (1 - a_o/a)^M (a_o/a)^N$, where a is the grain radius, $a_o = 0.1 \mu\text{m}$, the minimum grain radius, and M and N are independent parameters. N is considered the differential size distribution slope for larger radii sized grains ($\gtrsim 10 \mu\text{m}$) and is better constrained at wavelengths longer than 13 μm . M is used with N to calculate the peak of the HGSD; $a_{peak} = a_o(M + N)/N$.

Finally, correcting for the distance between the observer and the comet, a linear combination of discrete mineral components, porous amorphous materials and solid crystals, is least-squares fit to the observed SED. To manage the extent

of parameters in our thermal model grids, we choose five values for D ranging from solid to porous (3.0, 2.857, 2.727, 2.609, and 2.5), eight values for N ranging from a broad to narrow grain size distribution (3.4–4.2 in increments of 0.1), and increment M such that a_p begins at $0.1 \mu\text{m}$ and is incremented by $0.1 \mu\text{m}$. The relative mass fractions, their correlated errors, the porosity, and the size distribution are given as a prescription for the composition of coma grains. We quote the relative masses of the small grain portion of the size distribution ($0.1\text{--}1 \mu\text{m}$) that includes discrete crystals, which is a standard practice in the literature.

3.4. Model-fitting and Monte Carlo Uncertainties

The model is fit to the observed spectra using a least-squares method. If observed, emission from the ν_2 water band around $6 \mu\text{m}$ is masked out of the model fit. In addition, an emissivity feature is seen at $13.5\text{--}15.7 \mu\text{m}$ (covered by the LL2 module) that appears to be emission from a not yet identified material. To test whether the $14 \mu\text{m}$ feature should be masked or not during the modeling, we applied the Akaike Information Criteria (Section 4.5, Appendix A). Thermal models affected by this feature are 78P, 88P, C2003K4-20050913, C2003T4-20051122, and C2006P1-20070802.

Model compositional uncertainties are estimated with a Monte Carlo (bootstrap) analysis. For each spectrum, 10,000 alternate realizations are generated by adding noise to each data point, picked from a normally distributed variate with a width equal to the estimated spectral uncertainty. Each spectrum is re-fit, holding N , a_p , and D constant, but allowing the relative mass fraction of each dust component to vary. The final compositional uncertainties are the inner 95% confidence intervals for each parameter.

4. RESULTS AND DISCUSSION

4.1. Silicate feature shapes

We first present an empirical analysis of the data set, before later employing the dust thermal emission model to interpret spectral features. First, the 7 to $13 \mu\text{m}$ region of each spectrum was examined for evidence of common dust emission features, especially the broad amorphous silicate band and narrow emission features from Mg-rich olivine. For each spectrum, a scaled Planck function is fit to the pseudo-continuum defined as spanning $\lambda = 7.3\text{--}7.7 \mu\text{m}$ and $12.3\text{--}13.0 \mu\text{m}$. These pseudo-continuum points were chosen through experimentation on the data, but are similar to those used by other comet modelers (e.g., Sitko et al. 2004). In particular, the shape of the best-quality Spitzer spectra suggests the blue edge of the $10\text{-}\mu\text{m}$ feature is near $7.5 \mu\text{m}$ for most comets. Such a minimum would be difficult to observe at a ground-based facility due to strong telluric methane absorption around $\simeq 7.64 \mu\text{m}$. The silicate strength and local color temperature are summarized in Table 2.

The ability to extract the shape of the $10\text{-}\mu\text{m}$ band is primarily affected by the S/N ratio near $7.5 \mu\text{m}$ and the relative strength of the band above the local continuum, i.e., comet spectra with band strengths $\lesssim 5\%$, perhaps due to large grain sizes, and/or low silicate-to-amorphous carbon ratios tend to lack sufficient S/N for a band shape analysis. Therefore, our examination of the silicate feature strengths may represent a biased subset of the comet population. The analysis is limited to a subset of the survey comets only including: 9P, 17P, 21P, 37P, 46P, 67P, 71P, 73P-B, 73P-C, 78P, C/2001 Q4, C/2003 K4, C/2006 P1, C/2007 N3, and C/2008 T2.

Table 2. Color Temperature and Silicate Strength

Comet Name	T_{fit}^a (K)	T_{BB}^b (K)	T_{fit}/T_{BB}	$F_{10.5}/F_c$
6P	261 ± 1	236	1.106 ± 0.003	1.134 ± 0.046
8P	291 ± 2	219	1.328 ± 0.009	1.061 ± 0.065
9P-20050702	265 ± 1	227	1.169 ± 0.003	1.194 ± 0.044
9P-20050703	258 ± 1	227	1.140 ± 0.003	1.189 ± 0.045
17P	196 ± 1	176	1.113 ± 0.006	2.113 ± 0.122
21P	222 ± 9	184	1.209 ± 0.050	1.213 ± 0.411
29P	214 ± 15	116	1.841 ± 0.126	1.603 ± 0.926
37P	252 ± 1	211	1.195 ± 0.004	1.242 ± 0.043
41P	276 ± 3	246	1.120 ± 0.011	1.104 ± 0.083
46P-20071208	267 ± 0	245	1.093 ± 0.002	1.123 ± 0.025
46P-20080117	285 ± 0	268	1.063 ± 0.001	1.124 ± 0.023
46P-20080424	252 ± 0	227	1.109 ± 0.002	1.107 ± 0.026
46P-20080524	232 ± 0	211	1.100 ± 0.001	1.096 ± 0.024
46P-20080702	218 ± 2	193	1.128 ± 0.010	1.056 ± 0.084
48P	219 ± 2	183	1.196 ± 0.013	1.310 ± 0.128
62P	247 ± 3	216	1.140 ± 0.013	1.150 ± 0.107
65P	149 ± 5	149	0.999 ± 0.034	1.272 ± 0.525
67P-20080629.82	166 ± 0	167	0.996 ± 0.002	...
67P-20081128.38	229 ± 1	216	1.057 ± 0.004	1.229 ± 0.057
67P-20081129.11	230 ± 1	217	1.063 ± 0.003	1.201 ± 0.042
67P-20081129.70	228 ± 1	217	1.050 ± 0.004	1.217 ± 0.054
67P-20081130.48	233 ± 1	217	1.074 ± 0.004	1.190 ± 0.050
71P	256 ± 0	222	1.151 ± 0.001	1.107 ± 0.021
73P(B)-20060417.59	286 ± 0	255	1.122 ± 0.001	1.235 ± 0.024
73P(B)-20060806.18	280 ± 1	248	1.132 ± 0.006	1.178 ± 0.051
73P(C)-20060317.04	263 ± 0	230	1.144 ± 0.001	1.336 ± 0.027
73P(C)-20060806.05	268 ± 0	247	1.085 ± 0.001	1.239 ± 0.025
78P	209 ± 1	194	1.081 ± 0.003	1.234 ± 0.039
88P	208 ± 0	197	1.059 ± 0.002	1.104 ± 0.032
105P	237 ± 2	192	1.231 ± 0.008	1.084 ± 0.065
121P	187 ± 5	161	1.166 ± 0.028	1.222 ± 0.297
123P	205 ± 1	188	1.086 ± 0.007	...

Table 2 continued

Table 2 (continued)

Comet	T_{fit}^a	T_{BB}^b		
Name	(K)	(K)	T_{fit}/T_{BB}	$F_{10.5}/F_c$
132P	227 ± 4	193	1.176 ± 0.019	1.258 ± 0.200
144P	260 ± 1	223	1.167 ± 0.002	1.052 ± 0.026
C2001Q4	200 ± 1	172	1.162 ± 0.003	1.250 ± 0.046
C2003K4-20040716	234 ± 0	210	1.116 ± 0.002	1.095 ± 0.028
C2003K4-20050913	132 ± 2	131	1.010 ± 0.019	1.160 ± 0.299
C2003T3	167 ± 2	147	1.136 ± 0.013	1.113 ± 0.140
C2003T4-20051122	181 ± 2	148	1.218 ± 0.012	1.081 ± 0.109
C2003T4-20060129	153 ± 4	135	1.136 ± 0.030	1.151 ± 0.360
C2003T4-20060307	139 ± 1	129	1.076 ± 0.007	...
C2004B1-20051015	203 ± 0	187	1.088 ± 0.002	1.097 ± 0.034
C2004B1-20060516	210 ± 0	194	1.081 ± 0.002	1.111 ± 0.029
C2004B1-20060726	171 ± 1	170	1.010 ± 0.007	1.201 ± 0.089
C2004B1-20070308	148 ± 5	127	1.168 ± 0.036	1.044 ± 0.399
C2004B1-20070609	134 ± 3	117	1.141 ± 0.027	...
C2004Q2	188 ± 0	174	1.080 ± 0.003	1.190 ± 0.038
C2006P1-20070504	200 ± 1	180	1.114 ± 0.003	1.127 ± 0.042
C2006P1-20070802	157 ± 1	146	1.077 ± 0.008	1.219 ± 0.118
C2006P1-20070906	251 ± 62	138	1.816 ± 0.451	0.682 ± 1.218
C2006Q1-20070322	124 ± 1	121	1.024 ± 0.005	...
C2006Q1-20080117	170 ± 1	154	1.103 ± 0.007	1.036 ± 0.078
C2006Q1-20080225	164 ± 2	159	1.034 ± 0.015	1.141 ± 0.190
C2006Q1-20080702	178 ± 1	167	1.064 ± 0.005	1.138 ± 0.059
C2006Q1-20080709	173 ± 0	167	1.032 ± 0.001	1.183 ± 0.030
C2007N3	220 ± 0	202	1.090 ± 0.001	1.084 ± 0.023
C2008T2	246 ± 0	219	1.123 ± 0.002	1.069 ± 0.024

^a Temperature of BB fit to local continuum points defined as between 7.8–8.0 μm and 12.4–12.8 μm .

^b $T_{BB} = 278/\sqrt{r_h}$; where the heliocentric distance, r_h , is in AU.

Each spectrum was normalized by a best-fit Planck function, then offset and scaled so that the continuum was set to 0, and the band strength at 9.3 μm scaled to 1.0. Figure 1 shows an example this band-shape analysis and the range of band-shapes that are possible. Comet spectra in the 10 μm region exhibit a range of silicate feature shapes. No single feature is representative of the whole sample ensemble, corroborating conclusions reached by Hanner et al. (1994) and Sitko et al. (2004). The spectra of three comets serve to general categorize 10 μm spectral shapes: 46P, with a nearly trapezoidal feature; 17P, with strong narrow (~ 0.3 μm) features and a stronger 9- μm shoulder; and, 73P-C, with stronger emission at 8.2 μm .

The 8.2- μm excess in the spectra of 73P-C and 73P-B was noted by Kelley et al. (2017). They described the spectra as being more rounded or triangular, as opposed to trapezoidal. To further investigate this difference, we have re-normalized

the spectra at 11.1 μm as Figure 1 (right). Here, rather than 73P-C standing out from 17P and 46P, there is a progression in the relative 8.2- μm emission strength from 46P to 17P to 73P-C. Ortho-pyroxene has strong emission at 9.3 μm and Mg-rich crystalline olivine at 10 μm ; however, the shape of these features varies between comets. Narrow and triangular shapes of the 10 μm feature, like those evident in comet 17P, are indicative of a preponderance of submicron crystalline silicates (which have narrower solid state bands) being present in the coma. This is in contrast to comet 73P, which has a flatter, broader feature, the signature of amorphous silicates.

4.2. Thermal Model Fit Outcomes

Thermal models (Section 3) are fitted to the observed IRS SEDs that have full wavelength coverage (SL+LL, hereafter called SLLL) and to those that only have short wavelength coverage (SL). In addition, independent thermal models are fitted to the short wavelength portion of the full wavelength data (hereafter designated as SLLL–SL), which is instructive for investigating systematic differences between thermal model parameters derived from fits to data limited to the mid-infrared wavelength range. The sensitivity of wavelength range fitting is discussed in detail in Section 4.5.

The parameters of the thermal model and dust composition derived from analysis of the spectral energy distribution (SED) for each survey comet and epoch are summarized in Tables 3 and 4. The best-fits obtained from the Monte Carlo (Section 3) analysis allow us to examine correlations between compositional abundances for each spectrum. In Figure 2, the probability distributions for 10,000 spectral fit trials, plotted versus model composition is presented illustrating compositional interdependencies. For completeness, similar tables are provided in the appendix (Tables A2, A3) for comets observed with SLLL but only modeled over SLLL–SL wavelengths.

Not every model fit is included in the subsequent analysis. Comets only observed with the LL modules (67P-20080629.82, 123P, C/2003T4-20060307, C/2004B1-20070609, and C/2006Q1-20070322) are not included because the SL1 module includes strong and overlapping mineral features from crystalline silicates and amorphous silicates that are key for mineralogical identification as well as the fluxes in 10 μm region being critical to constraining the dust temperatures. In addition, comet 132P was not included in the analysis due to its very low S/N which results in an ill-defined model fit.

Comparisons of the compositions retrieved from the full wavelength range (SLLL, ~ 5 –35 μm) to those retrieved from fits restricted to the short wavelengths (SLL–SL, ~ 5 –13 μm) are shown in Figure 3. Rarely are the spectral features in the 15–33 μm region of sufficient spectral contrast to allow

Table 3. All Comets Observed in Survey: Best-Fit Thermal Emission Model Parameters

Comet Name	N	M	a_p	D	$N_p(\times 10^{16})$						χ^2_ν
					Amorphous Pyroxene	Amorphous Olivine	Amorphous Carbon	Crystalline Olivine	Crystalline Orthopyroxene		
6P	4.2	29.4	0.8	2.727	6.508e + 01 ^{+9.103e+00} _{-2.072e+01}	2.651e + 00 ^{+1.119e+01} _{-2.651e+00}	2.104e + 02 ^{+2.757e+00} _{-2.504e+00}	1.785e + 01 ^{+2.098e+01} _{-1.785e+01}	0.000e + 00 ^{+3.748e+01} _{-0.000e+00}	0.54	
8P	3.4	6.8	0.3	2.857	0.000e + 00 ^{+0.000e+00} _{-0.000e+00}	1.730e + 02 ^{+9.477e+01} _{-1.228e+02}	6.842e + 03 ^{+1.083e+02} _{-9.815e+01}	7.847e + 01 ^{+1.263e+02} _{-7.847e+01}	3.132e + 01 ^{+2.081e+02} _{-3.132e+01}	0.77	
9P-20050702	3.6	14.4	0.5	2.857	1.268e + 03 ^{+1.598e+02} _{-2.005e+02}	9.497e + 01 ^{+1.342e+02} _{-9.497e+01}	3.948e + 03 ^{+3.893e+01} _{-3.912e+01}	1.684e + 02 ^{+1.120e+02} _{-1.134e+02}	0.000e + 00 ^{+6.723e+01} _{-0.000e+00}	1.78	
9P-20050703	3.9	19.5	0.6	2.857	1.197e + 03 ^{+5.168e+01} _{-5.202e+01}	0.000e + 00 ^{+0.000e+00} _{-0.000e+00}	3.427e + 03 ^{+3.364e+01} _{-3.297e+01}	1.224e + 02 ^{+1.023e+02} _{-1.009e+02}	0.000e + 00 ^{+0.000e+00} _{-0.000e+00}	3.54	
17P	3.6	7.2	0.3	2.857	2.841e + 05 ^{+2.605e+04} _{-2.603e+04}	3.954e + 05 ^{+1.604e+04} _{-1.579e+04}	2.526e + 05 ^{+3.791e+03} _{-3.701e+03}	1.180e + 05 ^{+1.026e+04} _{-1.069e+04}	0.000e + 00 ^{+3.425e+03} _{-0.000e+00}	7.55	
21P	4.2	25.2	0.7	2.727	1.059e + 02 ^{+4.959e+01} _{-5.158e+01}	1.312e + 02 ^{+2.638e+01} _{-2.711e+01}	7.992e + 02 ^{+8.661e+00} _{-8.103e+00}	0.000e + 00 ^{+2.012e+01} _{-0.000e+00}	4.399e + 01 ^{+5.952e+01} _{-4.399e+01}	2.83	
29P	3.3	3.3	0.2	2.857	7.407e + 05 ^{+1.444e+05} _{-1.502e+05}	6.095e + 05 ^{+1.033e+05} _{-1.036e+05}	1.173e + 06 ^{+2.990e+04} _{-2.978e+04}	4.293e + 05 ^{+4.576e+04} _{-4.699e+04}	2.763e + 04 ^{+7.237e+04} _{-2.763e+04}	2.04	
37P	3.9	19.5	0.6	2.727	6.007e + 01 ^{+1.641e+01} _{-1.812e+01}	4.846e + 01 ^{+9.374e+00} _{-9.073e+00}	2.473e + 02 ^{+2.934e+00} _{-2.676e+00}	1.628e + 01 ^{+9.254e+00} _{-9.257e+00}	4.603e + 00 ^{+1.731e+01} _{-4.603e+00}	1.86	
41P	3.4	10.2	0.4	3.0	0.000e + 00 ^{+2.360e+01} _{-0.000e+00}	3.011e + 01 ^{+4.046e+00} _{-1.318e+01}	2.408e + 02 ^{+3.833e+00} _{-3.969e+00}	1.238e + 01 ^{+9.276e+00} _{-8.913e+00}	0.000e + 00 ^{+0.000e+00} _{-0.000e+00}	1.40	
46P-20071208	4.1	28.7	0.8	2.727	1.930e + 01 ^{+7.201e+00} _{-7.268e+00}	6.492e + 00 ^{+4.185e+00} _{-4.481e+00}	1.418e + 02 ^{+9.976e-01} _{-9.827e-01}	5.801e + 00 ^{+9.428e+00} _{-5.801e+00}	1.025e + 01 ^{+1.802e+01} _{-1.025e+01}	0.47	
46P-20080117	3.8	22.8	0.7	2.727	2.300e + 01 ^{+9.855e+00} _{-9.575e+00}	9.890e + 00 ^{+6.208e+00} _{-6.315e+00}	2.370e + 02 ^{+1.376e+00} _{-1.440e+00}	1.389e + 01 ^{+1.228e+01} _{-1.259e+01}	3.851e + 01 ^{+2.342e+01} _{-2.386e+01}	0.52	
46P-20080424	3.5	17.5	0.6	2.727	2.930e + 01 ^{+7.532e+00} _{-7.567e+00}	6.290e + 00 ^{+4.493e+00} _{-4.627e+00}	1.691e + 02 ^{+1.179e+00} _{-1.160e+00}	0.000e + 00 ^{+4.952e+00} _{-0.000e+00}	0.000e + 00 ^{+2.089e+00} _{-0.000e+00}	1.48	
46P-20080524	4.0	36.0	1.0	2.727	1.542e + 01 ^{+1.887e+00} _{-2.353e+00}	0.000e + 00 ^{+1.006e+00} _{-0.000e+00}	1.369e + 02 ^{+8.240e-01} _{-8.361e-01}	0.000e + 00 ^{+5.258e+00} _{-0.000e+00}	2.687e + 01 ^{+2.127e+01} _{-2.139e+01}	2.08	
46P-20080702	3.4	17.0	0.6	3.0	3.879e + 01 ^{+7.478e+00} _{-2.145e+01}	1.312e + 01 ^{+5.174e+00} _{-5.583e+00}	1.680e + 02 ^{+2.618e+00} _{-2.618e+00}	0.000e + 00 ^{+0.000e+00} _{-0.000e+00}	0.000e + 00 ^{+0.000e+00} _{-0.000e+00}	2.02	
48P	3.3	9.9	0.4	3.0	0.000e + 00 ^{+0.000e+00} _{-0.000e+00}	1.678e + 03 ^{+1.108e+02} _{-1.069e+02}	4.171e + 03 ^{+1.103e+02} _{-1.122e+02}	6.141e + 02 ^{+1.583e+02} _{-1.525e+02}	4.646e + 02 ^{+2.163e+02} _{-2.157e+02}	1.22	
62P	3.3	9.9	0.4	3.0	3.879e + 01 ^{+7.478e+00} _{-2.145e+01}	0.000e + 00 ^{+0.000e+00} _{-0.000e+00}	5.807e + 01 ^{+6.528e+00} _{-6.528e+00}	1.750e + 00 ^{+4.118e+00} _{-1.750e+00}	7.777e + 00 ^{+8.414e+00} _{-7.777e+00}	0.61	
65P	3.7	37.0	1.1	3.0	0.000e + 00 ^{+0.000e+00} _{-0.000e+00}	1.120e + 02 ^{+1.074e+01} _{-1.089e+01}	3.778e + 02 ^{+1.113e+01} _{-1.085e+01}	1.719e + 02 ^{+1.023e+02} _{-1.003e+02}	4.544e + 02 ^{+1.503e+02} _{-1.566e+02}	2.95	
67P-20080629.82	3.3	16.5	0.6	3.0	1.622e + 02 ^{+3.101e+01} _{-4.886e+01}	0.000e + 00 ^{+5.428e+01} _{-0.000e+00}	9.351e + 01 ^{+2.864e+01} _{-4.318e+01}	5.980e + 01 ^{+5.811e+01} _{-5.980e+01}	0.000e + 00 ^{+0.000e+00} _{-0.000e+00}	0.84	
67P-20081128.38	4.2	37.8	1.0	2.727	2.798e + 01 ^{+1.447e+01} _{-1.550e+01}	4.097e + 01 ^{+8.921e+00} _{-8.667e+00}	2.473e + 02 ^{+2.926e+00} _{-2.732e+00}	0.000e + 00 ^{+0.000e+00} _{-0.000e+00}	1.598e + 01 ^{+5.437e+01} _{-1.598e+01}	3.09	
67P-20081129.11	3.7	25.9	0.8	2.727	0.000e + 00 ^{+2.481e+00} _{-0.000e+00}	5.960e + 01 ^{+3.635e+00} _{-3.635e+00}	2.569e + 02 ^{+3.118e+00} _{-3.118e+00}	0.000e + 00 ^{+1.519e+01} _{-0.000e+00}	2.290e + 01 ^{+3.764e+01} _{-2.290e+01}	1.90	
67P-20081129.70	4.2	42.0	1.1	2.727	1.069e + 01 ^{+1.008e+01} _{-1.031e+01}	3.593e + 01 ^{+6.001e+00} _{-6.293e+00}	1.712e + 02 ^{+1.879e+00} _{-1.824e+00}	0.000e + 00 ^{+0.000e+00} _{-0.000e+00}	0.000e + 00 ^{+2.744e+01} _{-0.000e+00}	2.78	
67P-20081130.48	3.5	21.0	0.7	2.727	4.739e + 01 ^{+1.873e+01} _{-1.876e+01}	4.762e + 01 ^{+1.155e+01} _{-1.173e+01}	3.042e + 02 ^{+3.542e+00} _{-3.505e+00}	0.000e + 00 ^{+6.446e+00} _{-0.000e+00}	0.000e + 00 ^{+0.000e+00} _{-0.000e+00}	2.78	
71P	3.7	18.5	0.6	2.727	4.766e + 02 ^{+9.243e+01} _{-9.227e+01}	6.911e + 01 ^{+5.567e+01} _{-5.622e+01}	2.491e + 03 ^{+1.498e+01} _{-1.495e+01}	8.001e + 01 ^{+6.996e+01} _{-6.772e+01}	0.000e + 00 ^{+0.000e+00} _{-0.000e+00}	2.27	
73P(B)-20060417.59	4.3	25.8	0.7	2.727	5.319e + 01 ^{+1.638e+00} _{-2.764e+00}	0.000e + 00 ^{+0.000e+00} _{-0.000e+00}	1.258e + 02 ^{+6.590e-01} _{-5.952e-01}	9.576e + 00 ^{+4.200e+00} _{-4.171e+00}	2.018e - 01 ^{+8.586e+00} _{-2.018e-01}	1.16	
73P(B)-20060806.18	3.8	15.2	0.5	2.857	1.038e + 02 ^{+3.019e+00} _{-3.013e+00}	0.000e + 00 ^{+0.000e+00} _{-0.000e+00}	2.816e + 02 ^{+1.796e+00} _{-1.807e+00}	5.965e + 00 ^{+4.670e+00} _{-4.585e+00}	0.000e + 00 ^{+0.000e+00} _{-0.000e+00}	2.52	

Table 3 continued

Table 3 (continued)

Comet Name	N	M	a_p	D	Amorphous			Amorphous			Amorphous			χ^2	
					Pyroxene	Olivine	Carbon	Pyroxene	Olivine	Carbon	Olivine	Olivine	Orthopyroxene		
73P(C)-20060317.04	4.3	25.8	0.7	2.727	3.134e + 02	-1.263e+01	0.000e + 00	0.000e + 00	5.054e + 02	-2.459e+00	5.649e + 01	+2.121e+01	6.845e + 01	+4.133e+01	2.08
						-1.274e+01	-0.000e+00	-0.000e+00		-2.456e+00		-2.073e+01	-4.242e+01		
73P(C)-20060806.05	3.3	72.6	2.3	2.609	1.181e + 00	-4.355e-02	0.000e + 00	0.000e + 00	1.973e + 00	+9.653e-03	8.511e + 01	+1.234e+02	0.000e + 00	+2.079e+02	1.56
						-0.000e+00	-0.000e+00	-0.000e+00		-9.049e-03		-8.511e+01	-0.000e+00	-0.000e+00	
78P	3.8	22.8	0.7	3.0	1.275e + 03	-2.051e+02	1.576e + 03	+1.562e+02	5.128e + 03	-5.983e+01	1.442e + 03	+2.491e+02	2.749e + 02	+3.728e+02	1.83
						-1.986e+02	-1.580e+02	-1.580e+02		-5.775e+01		-2.440e+02	-2.749e+02	-2.749e+02	
88P	3.4	20.4	0.7	3.0	1.380e + 02	-2.538e+01	1.412e + 02	+2.288e+01	6.439e + 02	-1.118e+01	6.478e + 01	+4.476e+01	0.000e + 00	+0.000e+00	1.23
						-2.511e+01	-2.344e+01	-2.344e+01		-1.129e+01		-4.641e+01	-4.641e+01	-4.641e+01	
105P	3.3	9.9	0.4	3.0	3.560e + 02	-7.779e+01	0.000e + 00	+4.371e+01	9.173e + 02	-4.657e+01	0.000e + 00	+1.857e+01	1.034e + 02	+9.495e+01	1.04
						-1.174e+02	-0.000e+00	-0.000e+00		-4.096e+01		-0.000e+00	-9.569e+01	-9.569e+01	
121P	3.3	16.5	0.6	3.0	4.769e + 02	-1.968e+02	0.000e + 00	+1.968e+02	2.846e + 02	-1.055e+02	1.748e + 02	+1.224e+02	1.792e + 02	+2.310e+02	0.77
						-4.769e+02	-0.000e+00	-0.000e+00		-6.917e+01		-1.331e+02	-1.792e+02	-1.792e+02	
123P	3.3	9.9	0.4	3.0	1.572e + 03	-3.445e+02	9.833e + 02	+3.249e+02	6.517e + 03	-2.692e+02	9.647e + 02	+2.367e+02	2.009e + 02	+3.712e+02	1.04
						-3.423e+02	-3.361e+02	-3.361e+02		-2.577e+02		-2.439e+02	-2.439e+02	-2.439e+02	
132P	3.3	33.0	1.1	2.609	6.374e + 00	-6.374e+00	6.364e - 01	+2.627e+00	9.691e + 00	-8.333e-01	0.000e + 00	+3.036e+01	6.645e + 01	+9.299e+01	0.61
						-6.374e+00	-6.374e+00	-6.374e+00		-7.153e-01		-0.000e+00	-6.645e+01	-6.645e+01	
144P	3.3	9.9	0.4	2.727	1.481e + 02	-9.487e+00	0.000e + 00	+0.000e+00	5.666e + 02	-4.506e+00	0.000e + 00	+0.000e+00	0.000e + 00	+0.000e+00	2.05
						-9.444e+00	-0.000e+00	-0.000e+00		-4.539e+00		-0.000e+00	-0.000e+00	-0.000e+00	
C2001Q4	3.3	13.2	0.5	3.0	9.086e + 03	-1.135e+03	2.267e + 03	-7.557e+02	1.016e + 04	-1.139e+02	2.950e + 03	+8.416e+02	2.826e + 03	+1.416e+03	1.99
						-1.150e+03	-1.150e+03	-7.557e+02		-1.139e+02		-8.416e+02	-1.416e+03	-1.416e+03	
C2003K4-20040716	3.6	21.6	0.7	2.727	8.842e + 02	-6.539e+01	0.000e + 00	+0.000e+00	3.640e + 03	-2.259e+01	0.000e + 00	+1.490e+02	3.256e + 02	+4.489e+02	2.07
						-7.802e+01	-0.000e+00	-0.000e+00		-2.210e+01		-0.000e+00	-3.256e+02	-3.256e+02	
C2003K4-20050913	3.3	39.6	1.3	3.0	7.149e + 02	-1.843e+02	2.049e + 03	+2.229e+02	2.825e + 03	-1.193e+02	0.000e + 00	+6.095e+02	0.000e + 00	+0.000e+00	2.70
						-1.843e+02	-1.843e+02	-2.319e+02		-1.159e+02		-0.000e+00	-0.000e+00	-0.000e+00	
C2003T3	3.5	31.5	1.0	2.857	5.670e + 02	-3.161e+01	0.000e + 00	+0.000e+00	7.589e + 02	-2.457e+01	4.062e + 02	+2.504e+02	0.000e + 00	+3.703e+02	1.41
						-3.694e+01	-0.000e+00	-0.000e+00		-2.345e+01		-2.677e+02	-0.000e+00	-0.000e+00	
C2003T4-20051122	3.6	28.8	0.9	3.0	1.337e + 03	-9.425e+01	2.054e + 02	+9.407e+01	1.444e + 03	-3.780e+01	1.337e + 03	+2.570e+02	1.036e + 03	+3.918e+02	5.45
						-9.456e+01	-0.000e+00	-0.000e+00		-3.921e+01		-2.561e+02	-3.918e+02	-3.918e+02	
C2003T4-20060129	3.7	40.7	1.2	2.727	0.000e + 00	-0.000e+00	1.295e + 02	+1.786e+01	1.118e + 03	-1.895e+01	1.319e + 03	+4.511e+02	0.000e + 00	+4.933e+02	3.59
						-0.000e+00	-0.000e+00	-0.000e+00		-1.727e+01		-4.531e+02	-0.000e+00	-0.000e+00	
C2003T4-20060307	3.3	16.5	0.6	2.857	2.196e + 03	-1.261e+02	0.000e + 00	+0.000e+00	3.002e + 03	-8.929e+01	8.969e + 02	+2.926e+02	6.357e + 02	+4.511e+02	4.72
						-1.253e+02	-0.000e+00	-0.000e+00		-8.929e+01		-3.003e+02	-4.566e+02	-4.566e+02	
C2004B1-20051015	4.2	46.2	1.2	2.727	2.222e + 02	-2.362e+01	0.000e + 00	+0.000e+00	9.621e + 02	-6.104e+00	0.000e + 00	+2.111e+02	1.984e + 02	+6.119e+02	3.42
						-2.362e+01	-0.000e+00	-0.000e+00		-6.104e+00		-0.000e+00	-1.984e+02	-6.119e+02	
C2004B1-20060516	4.2	42.0	1.1	2.727	1.780e + 02	-1.528e+01	0.000e + 00	+7.585e+00	6.609e + 02	-5.986e+00	0.000e + 00	+1.546e+02	1.630e + 02	+3.030e+02	1.08
						-2.453e+01	-0.000e+00	-0.000e+00		-5.986e+00		-0.000e+00	-1.630e+02	-3.030e+02	
C2004B1-20060726	3.5	31.5	1.0	2.727	0.000e + 00	-0.000e+00	5.426e + 01	+5.314e+00	3.363e + 02	-4.718e+00	4.315e + 00	+7.078e+01	8.920e + 01	+1.206e+02	1.67
						-0.000e+00	-0.000e+00	-0.000e+00		-4.718e+00		-4.315e+00	-8.920e+01	-1.206e+02	
C2004B1-20070308	3.6	32.4	1.0	2.857	0.000e + 00	-0.000e+00	0.000e + 00	+0.000e+00	2.310e + 03	-7.767e+00	0.000e + 00	+8.210e+01	0.000e + 00	+0.000e+00	5.46
						-0.000e+00	-0.000e+00	-0.000e+00		-7.767e+00		-0.000e+00	-0.000e+00	-0.000e+00	
C2004B1-20070609	3.3	19.8	0.7	3.0	1.912e + 03	-1.276e+02	0.000e + 00	+0.000e+00	1.980e + 03	-1.149e+02	0.000e + 00	+0.000e+00	5.937e + 02	+5.193e+02	27.07
						-1.276e+02	-0.000e+00	-0.000e+00		-1.149e+02		-0.000e+00	-5.193e+02	-5.193e+02	
C2004Q2	4.3	60.2	1.5	2.727	8.320e + 02	-2.727e+01	0.000e + 00	+0.000e+00	1.199e + 03	-1.438e+01	0.000e + 00	+0.000e+00	0.000e + 00	+5.452e+02	4.96
						-2.727e+01	-0.000e+00	-0.000e+00		-1.438e+01		-0.000e+00	-0.000e+00	-5.452e+02	
C2006P1-20070504	3.6	28.8	0.9	2.727	2.159e + 03	-1.195e+02	0.000e + 00	+2.079e+01	8.451e + 03	-5.688e+01	1.981e + 02	+9.666e+02	0.000e + 00	+0.000e+00	2.47
						-1.195e+02	-0.000e+00	-0.000e+00		-5.334e+01		-1.981e+02	-0.000e+00	-0.000e+00	
C2006P1-20070802	3.6	32.4	1.0	3.0	0.000e + 00	-0.000e+00	1.923e + 03	+6.671e+01	2.819e + 03	-7.241e+01	1.826e + 02	+6.355e+02	0.000e + 00	+0.000e+00	4.01
						-0.000e+00	-0.000e+00	-0.000e+00		-7.241e+01		-6.355e+02	-0.000e+00	-0.000e+00	
C2006P1-20070906	4.0	48.0	1.3	3.0	8.127e + 00	-1.137e+02	4.505e + 02	+5.352e+01	1.999e + 03	-5.219e+01	6.600e + 02	+9.028e+02	3.097e + 03	+1.265e+03	7.52
						-1.137e+02	-1.137e+02	-5.352e+01		-5.219e+01		-9.028e+02	-1.265e+03	-1.265e+03	
C2006Q1-20070322	3.7	48.1	1.4	2.857	5.170e + 02	-7.135e+01	0.000e + 00	+1.233e+02	2.751e + 03	-5.992e+01	1.735e + 03	+2.131e+03	0.000e + 00	+1.100e+03	2.93
						-7.135e+01	-0.000e+00	-0.000e+00		-5.992e+01		-2.131e+03	-0.000e+00	-1.100e+03	
C2006Q1-20080117	4.0	44.0	1.2	2.857	3.305e + 02	-1.536e+02	4.224e + 01	+1.149e+02	3.030e + 03	-4.444e+01	1.402e + 02	+6.824e+02	0.000e + 00	+7.945e+02	0.90
						-1.536e+02	-1.149e+02	-1.149e+02		-4.444e+01		-6.824e+02	-7.945e+02	-7.945e+02	

Table 3 continued

Table 3 (continued)

Comet Name	N	M	a_p^a	D	Amorphous		Amorphous		Amorphous		Crystalline		Crystalline		χ^2_L
					Pyroxene	Olivine	Olivine	Carbon	Olivine	Olivine	Orthopyroxene				
C2006Q1-20080225	3.4	27.2	0.9	3.0	1.915e + 03 ^{+3.372e+02} _{-5.831e+02}	0.000e + 00 ^{+2.369e+02} _{-0.000e+00}	1.917e + 03 ^{+2.365e+02} _{-2.000e+02}	2.227e + 02 ^{+7.057e+02} _{-2.227e+02}	0.000e + 00 ^{+1.367e+02} _{-0.000e+00}	1.18					
C2006Q1-20080702	3.5	28.0	0.9	3.0	0.000e + 00 ^{+1.658e+01} _{-0.000e+00}	1.001e + 03 ^{+4.165e+01} _{-4.650e+01}	2.738e + 03 ^{+4.120e+01} _{-4.060e+01}	2.536e + 02 ^{+3.453e+02} _{-2.536e+02}	4.930e + 02 ^{+5.056e+02} _{-4.930e+02}	1.39					
C2006Q1-20080709	3.3	23.1	0.8	3.0	2.439e + 03 ^{+4.492e+02} _{-4.467e+02}	4.807e + 02 ^{+2.945e+02} _{-3.072e+02}	2.113e + 03 ^{+4.296e+01} _{-4.152e+01}	3.281e + 02 ^{+5.855e+02} _{-3.281e+02}	7.939e + 02 ^{+9.225e+02} _{-7.939e+02}	1.24					
C2007N3	4.0	36.0	1.0	2.727	8.039e + 02 ^{+6.671e+01} _{-9.628e+01}	0.000e + 00 ^{+1.859e+01} _{-0.000e+00}	4.229e + 03 ^{+2.448e+01} _{-2.249e+01}	6.668e + 01 ^{+6.136e+02} _{-6.668e+01}	6.034e + 02 ^{+1.094e+03} _{-6.034e+02}	1.26					
C2008T2	3.6	18.0	0.6	2.857	1.620e + 02 ^{+4.142e+01} _{-4.281e+01}	4.025e + 01 ^{+2.714e+01} _{-2.662e+01}	1.138e + 03 ^{+9.314e+00} _{-9.569e+00}	0.000e + 00 ^{+0.000e+00} _{-0.000e+00}	0.000e + 00 ^{+0.000e+00} _{-0.000e+00}	1.95					

NOTE— Bold values indicate values constrained to a confidence level of 95%.

^a Derived parameter.

Table 4. All Comets Observed in Survey: Mass of Submicron Grains

Comet	Total Mass	Mass Relative to Total Mass					Crystalline	Crystalline	Silicate/Carbon	f_{crist}^a
		Amorphous	Amorphous	Amorphous	Crystalline	Crystalline				
Name	($\times 10^7$ kg)	Pyroxene	Olivine	Carbon	Olivine	Orthopyroxene	Ratio			
6P	$3.393e + 03^{+1.267e+03}_{-3.393e+03}$	$0.334^{+0.078}_{-0.126}$	$0.014^{+0.064}_{-0.014}$	$0.491^{+0.098}_{-0.133}$	$0.162^{+0.128}_{-0.162}$	$0.000^{+0.257}_{-0.000}$	$1.039^{+0.761}_{-0.341}$	$0.318^{+0.325}_{-0.318}$		
8P	$2.398e + 04^{+1.683e+03}_{-2.398e+04}$	$0.000^{+0.000}_{-0.000}$	$0.050^{+0.028}_{-0.036}$	$0.908^{+0.039}_{-0.058}$	$0.030^{+0.045}_{-0.030}$	$0.012^{+0.075}_{-0.012}$	$0.102^{+0.076}_{-0.045}$	$0.454^{+0.421}_{-0.454}$		
9P-20050702	$5.740e + 04^{+2.683e+03}_{-5.740e+04}$	$0.375^{+0.046}_{-0.055}$	$0.028^{+0.042}_{-0.028}$	$0.531^{+0.025}_{-0.025}$	$0.066^{+0.040}_{-0.044}$	$0.000^{+0.026}_{-0.000}$	$0.885^{+0.091}_{-0.086}$	$0.141^{+0.084}_{-0.089}$		
9P-20050703	$5.907e + 04^{+2.375e+03}_{-5.907e+04}$	$0.410^{+0.027}_{-0.026}$	$0.000^{+0.000}_{-0.000}$	$0.534^{+0.023}_{-0.022}$	$0.056^{+0.043}_{-0.046}$	$0.000^{+0.000}_{-0.000}$	$0.873^{+0.079}_{-0.077}$	$0.120^{+0.084}_{-0.097}$		
17P	$6.212e + 06^{+9.948e+04}_{-6.212e+06}$	$0.299^{+0.024}_{-0.025}$	$0.417^{+0.022}_{-0.022}$	$0.121^{+0.003}_{-0.003}$	$0.163^{+0.012}_{-0.013}$	$0.000^{+0.005}_{-0.000}$	$7.263^{+0.204}_{-0.195}$	$0.185^{+0.015}_{-0.015}$		
21P	$1.150e + 04^{+1.630e+03}_{-1.150e+04}$	$0.156^{+0.078}_{-0.079}$	$0.194^{+0.052}_{-0.049}$	$0.536^{+0.060}_{-0.065}$	$0.000^{+0.050}_{-0.000}$	$0.114^{+0.123}_{-0.114}$	$0.866^{+0.259}_{-0.189}$	$0.246^{+0.221}_{-0.246}$		
29P	$6.037e + 06^{+1.993e+05}_{-6.037e+06}$	$0.300^{+0.054}_{-0.058}$	$0.246^{+0.047}_{-0.046}$	$0.216^{+0.008}_{-0.008}$	$0.224^{+0.021}_{-0.023}$	$0.014^{+0.037}_{-0.014}$	$3.638^{+0.175}_{-0.158}$	$0.304^{+0.044}_{-0.034}$		
37P	$3.998e + 03^{+4.529e+02}_{-3.998e+03}$	$0.233^{+0.063}_{-0.073}$	$0.188^{+0.047}_{-0.042}$	$0.437^{+0.036}_{-0.043}$	$0.110^{+0.053}_{-0.060}$	$0.031^{+0.105}_{-0.031}$	$1.290^{+0.251}_{-0.173}$	$0.251^{+0.158}_{-0.126}$		
41P	$2.511e + 03^{+2.181e+02}_{-2.511e+03}$	$0.000^{+0.146}_{-0.000}$	$0.198^{+0.030}_{-0.095}$	$0.720^{+0.037}_{-0.066}$	$0.081^{+0.053}_{-0.058}$	$0.000^{+0.000}_{-0.000}$	$0.388^{+0.141}_{-0.068}$	$0.291^{+0.141}_{-0.200}$		
46P-20071208	$2.070e + 03^{+6.781e+02}_{-2.070e+03}$	$0.163^{+0.072}_{-0.062}$	$0.055^{+0.053}_{-0.041}$	$0.543^{+0.156}_{-0.134}$	$0.087^{+0.109}_{-0.087}$	$0.153^{+0.177}_{-0.153}$	$0.841^{+0.602}_{-0.412}$	$0.524^{+0.213}_{-0.490}$		
46P-20080117	$3.998e + 03^{+8.501e+02}_{-3.998e+03}$	$0.099^{+0.045}_{-0.040}$	$0.042^{+0.039}_{-0.029}$	$0.463^{+0.125}_{-0.081}$	$0.105^{+0.075}_{-0.092}$	$0.291^{+0.106}_{-0.153}$	$1.161^{+0.461}_{-0.459}$	$0.737^{+0.089}_{-0.201}$		
46P-20080424	$1.787e + 03^{+1.531e+02}_{-1.787e+03}$	$0.261^{+0.056}_{-0.065}$	$0.056^{+0.042}_{-0.042}$	$0.683^{+0.020}_{-0.054}$	$0.000^{+0.071}_{-0.000}$	$0.000^{+0.031}_{-0.000}$	$0.463^{+0.126}_{-0.042}$	$0.000^{+0.216}_{-0.000}$		
46P-20080524	$1.966e + 03^{+5.928e+02}_{-1.966e+03}$	$0.123^{+0.066}_{-0.039}$	$0.000^{+0.008}_{-0.000}$	$0.495^{+0.202}_{-0.114}$	$0.000^{+0.070}_{-0.000}$	$0.382^{+0.145}_{-0.272}$	$1.019^{+0.605}_{-0.586}$	$0.757^{+0.105}_{-0.378}$		
46P-20080702	$2.880e + 03^{+2.602e+02}_{-2.880e+03}$	$0.133^{+0.054}_{-0.058}$	$0.127^{+0.050}_{-0.057}$	$0.740^{+0.020}_{-0.060}$	$0.000^{+0.000}_{-0.000}$	$0.000^{+0.089}_{-0.000}$	$0.352^{+0.120}_{-0.035}$	$0.000^{+0.283}_{-0.000}$		
48P	$7.841e + 04^{+3.219e+03}_{-7.841e+04}$	$0.000^{+0.000}_{-0.000}$	$0.361^{+0.033}_{-0.031}$	$0.408^{+0.019}_{-0.018}$	$0.132^{+0.032}_{-0.031}$	$0.100^{+0.042}_{-0.045}$	$1.454^{+0.115}_{-0.112}$	$0.391^{+0.057}_{-0.064}$		
62P	$1.259e + 03^{+9.606e+01}_{-1.259e+03}$	$0.519^{+0.110}_{-0.253}$	$0.000^{+0.147}_{-0.000}$	$0.353^{+0.099}_{-0.037}$	$0.023^{+0.054}_{-0.023}$	$0.104^{+0.106}_{-0.104}$	$1.830^{+0.333}_{-0.620}$	$0.197^{+0.196}_{-0.180}$		
65P	$2.321e + 04^{+4.028e+03}_{-2.321e+04}$	$0.000^{+0.000}_{-0.000}$	$0.123^{+0.034}_{-0.024}$	$0.189^{+0.039}_{-0.027}$	$0.189^{+0.104}_{-0.106}$	$0.499^{+0.104}_{-0.124}$	$4.299^{+0.903}_{-0.913}$	$0.848^{+0.033}_{-0.051}$		
67P-20080629.82	$7.420e + 03^{+1.561e+03}_{-7.420e+03}$	$0.613^{+0.183}_{-0.189}$	$0.000^{+0.216}_{-0.000}$	$0.161^{+0.077}_{-0.078}$	$0.226^{+0.148}_{-0.226}$	$0.000^{+0.000}_{-0.000}$	$5.222^{+5.864}_{-2.012}$	$0.269^{+0.173}_{-0.269}$		
67P-20081128.38	$3.260e + 03^{+1.442e+03}_{-3.260e+03}$	$0.133^{+0.084}_{-0.082}$	$0.195^{+0.070}_{-0.068}$	$0.536^{+0.097}_{-0.162}$	$0.000^{+0.000}_{-0.000}$	$0.136^{+0.280}_{-0.136}$	$0.867^{+0.812}_{-0.287}$	$0.293^{+0.372}_{-0.293}$		
67P-20081129.11	$3.815e + 03^{+1.224e+03}_{-3.815e+03}$	$0.000^{+0.011}_{-0.000}$	$0.275^{+0.075}_{-0.077}$	$0.538^{+0.122}_{-0.129}$	$0.000^{+0.115}_{-0.000}$	$0.187^{+0.191}_{-0.187}$	$0.857^{+0.585}_{-0.343}$	$0.405^{+0.259}_{-0.405}$		
67P-20081129.70	$1.719e + 03^{+6.593e+02}_{-1.719e+03}$	$0.086^{+0.074}_{-0.083}$	$0.289^{+0.057}_{-0.089}$	$0.625^{+0.024}_{-0.173}$	$0.000^{+0.000}_{-0.000}$	$0.000^{+0.285}_{-0.000}$	$0.599^{+0.610}_{-0.058}$	$0.000^{+0.523}_{-0.000}$		
67P-20081130.48	$4.044e + 03^{+2.146e+02}_{-4.044e+03}$	$0.203^{+0.072}_{-0.077}$	$0.204^{+0.056}_{-0.056}$	$0.593^{+0.024}_{-0.031}$	$0.000^{+0.046}_{-0.000}$	$0.000^{+0.000}_{-0.000}$	$0.687^{+0.094}_{-0.064}$	$0.000^{+0.108}_{-0.000}$		
71P	$2.856e + 04^{+1.900e+03}_{-2.856e+04}$	$0.262^{+0.048}_{-0.047}$	$0.038^{+0.033}_{-0.031}$	$0.623^{+0.043}_{-0.039}$	$0.077^{+0.059}_{-0.064}$	$0.000^{+0.000}_{-0.000}$	$0.605^{+0.107}_{-0.104}$	$0.204^{+0.126}_{-0.167}$		
73P(B)-20060417.59	$2.158e + 03^{+2.505e+02}_{-2.158e+03}$	$0.417^{+0.028}_{-0.060}$	$0.000^{+0.000}_{-0.000}$	$0.448^{+0.023}_{-0.047}$	$0.132^{+0.046}_{-0.055}$	$0.003^{+0.107}_{-0.003}$	$1.231^{+0.259}_{-0.107}$	$0.244^{+0.157}_{-0.083}$		
73P(B)-20060806.18	$3.984e + 03^{+8.683e+01}_{-3.984e+03}$	$0.433^{+0.017}_{-0.016}$	$0.000^{+0.000}_{-0.000}$	$0.534^{+0.013}_{-0.012}$	$0.033^{+0.025}_{-0.025}$	$0.000^{+0.000}_{-0.000}$	$0.873^{+0.044}_{-0.044}$	$0.071^{+0.051}_{-0.054}$		
73P(C)-20060317.04	$1.290e + 04^{+1.228e+03}_{-1.290e+04}$	$0.411^{+0.059}_{-0.048}$	$0.000^{+0.000}_{-0.000}$	$0.301^{+0.032}_{-0.026}$	$0.130^{+0.044}_{-0.044}$	$0.158^{+0.076}_{-0.092}$	$2.321^{+0.314}_{-0.320}$	$0.412^{+0.087}_{-0.116}$		
73P(C)-20060806.05	$2.295e + 02^{+6.318e+02}_{-2.295e+02}$	$0.006^{+0.565}_{-0.004}$	$0.000^{+0.000}_{-0.000}$	$0.004^{+0.425}_{-0.003}$	$0.990^{+0.006}_{-0.990}$	$0.000^{+0.976}_{-0.000}$	$2.263e + 02^{+6.248e+02}_{-2.249e+02}$	$0.994^{+0.004}_{-0.994}$		
78P	$2.084e + 05^{+1.197e+04}_{-2.084e+05}$	$0.185^{+0.029}_{-0.029}$	$0.228^{+0.031}_{-0.030}$	$0.338^{+0.019}_{-0.018}$	$0.209^{+0.030}_{-0.032}$	$0.040^{+0.050}_{-0.040}$	$1.960^{+0.171}_{-0.156}$	$0.376^{+0.056}_{-0.060}$		
88P	$1.946e + 04^{+1.333e+03}_{-1.946e+04}$	$0.217^{+0.038}_{-0.038}$	$0.222^{+0.046}_{-0.042}$	$0.460^{+0.036}_{-0.030}$	$0.102^{+0.059}_{-0.071}$	$0.000^{+0.000}_{-0.000}$	$1.175^{+0.151}_{-0.158}$	$0.188^{+0.096}_{-0.127}$		
105P	$1.477e + 04^{+1.057e+03}_{-1.477e+04}$	$0.406^{+0.098}_{-0.128}$	$0.000^{+0.052}_{-0.000}$	$0.476^{+0.057}_{-0.040}$	$0.000^{+0.021}_{-0.000}$	$0.118^{+0.098}_{-0.109}$	$1.102^{+0.191}_{-0.226}$	$0.225^{+0.191}_{-0.202}$		
121P	$2.694e + 04^{+5.065e+03}_{-2.694e+04}$	$0.497^{+0.213}_{-0.497}$	$0.000^{+0.290}_{-0.000}$	$0.135^{+0.118}_{-0.034}$	$0.182^{+0.133}_{-0.131}$	$0.187^{+0.200}_{-0.187}$	$6.423^{+2.495}_{-3.465}$	$0.426^{+0.278}_{-0.270}$		
123P	$1.126e + 05^{+5.295e+03}_{-1.126e+05}$	$0.235^{+0.051}_{-0.052}$	$0.147^{+0.051}_{-0.051}$	$0.443^{+0.026}_{-0.025}$	$0.144^{+0.032}_{-0.035}$	$0.030^{+0.053}_{-0.030}$	$1.256^{+0.134}_{-0.123}$	$0.313^{+0.085}_{-0.076}$		
132P	$1.865e + 03^{+2.634e+03}_{-1.865e+03}$	$0.039^{+0.589}_{-0.039}$	$0.004^{+0.099}_{-0.004}$	$0.027^{+0.313}_{-0.015}$	$0.000^{+0.476}_{-0.000}$	$0.931^{+0.045}_{-0.931}$	$36.293^{+49.018}_{-34.352}$	$0.956^{+0.035}_{-0.956}$		
144P	$4.003e + 03^{+8.483e+01}_{-4.003e+03}$	$0.365^{+0.016}_{-0.018}$	$0.000^{+0.000}_{-0.000}$	$0.635^{+0.017}_{-0.017}$	$0.000^{+0.000}_{-0.000}$	$0.000^{+0.000}_{-0.000}$	$0.575^{+0.044}_{-0.040}$	$0.000^{+0.006}_{-0.000}$		
C2001Q4	$5.081e + 05^{+4.183e+04}_{-5.081e+05}$	$0.418^{+0.043}_{-0.042}$	$0.104^{+0.044}_{-0.039}$	$0.212^{+0.020}_{-0.017}$	$0.136^{+0.033}_{-0.034}$	$0.130^{+0.053}_{-0.062}$	$3.708^{+0.399}_{-0.402}$	$0.337^{+0.063}_{-0.077}$		

Table 4 continued

Table 4 (continued)

Comet	Total Mass	Mass Relative to Total Mass						Silicate/Carbon	f_{cryst}^a
		Amorphous	Amorphous	Amorphous	Crystalline	Crystalline			
Name	($\times 10^7$ kg)	Pyroxene	Olivine	Carbon	Olivine	Orthopyroxene	Ratio		
C2003K4-20040716	$5.377e + 04^{+1.349e+04}_{-5.377e+04}$	$0.284^{+0.077}_{-0.073}$	$0.000^{+0.000}_{-0.000}$	$0.532^{+0.112}_{-0.106}$	$0.000^{+0.078}_{-0.000}$	$0.184^{+0.168}_{-0.184}$	$0.880^{+0.470}_{-0.327}$	$0.393^{+0.238}_{-0.393}$	
C2003K4-20050913	$8.181e + 04^{+1.226e+04}_{-8.181e+04}$	$0.177^{+0.046}_{-0.048}$	$0.506^{+0.054}_{-0.085}$	$0.317^{+0.016}_{-0.042}$	$0.000^{+0.131}_{-0.000}$	$0.000^{+0.000}_{-0.000}$	$2.152^{+0.485}_{-0.149}$	$0.000^{+0.183}_{-0.000}$	
C2003T3	$3.072e + 04^{+1.129e+04}_{-3.072e+04}$	$0.388^{+0.114}_{-0.113}$	$0.000^{+0.000}_{-0.000}$	$0.236^{+0.065}_{-0.063}$	$0.376^{+0.114}_{-0.000}$	$0.000^{+0.268}_{-0.000}$	$3.239^{+1.557}_{-0.916}$	$0.493^{+0.174}_{-0.207}$	
C2003T4-20051122	$1.388e + 05^{+1.336e+04}_{-1.388e+05}$	$0.292^{+0.031}_{-0.026}$	$0.045^{+0.024}_{-0.022}$	$0.144^{+0.014}_{-0.012}$	$0.293^{+0.047}_{-0.048}$	$0.227^{+0.063}_{-0.069}$	$5.967^{+0.648}_{-0.634}$	$0.606^{+0.043}_{-0.053}$	
C2003T4-20060129	$3.749e + 04^{+1.372e+04}_{-3.749e+04}$	$0.000^{+0.000}_{-0.000}$	$0.043^{+0.019}_{-0.015}$	$0.169^{+0.057}_{-0.045}$	$0.788^{+0.045}_{-0.197}$	$0.000^{+0.235}_{-0.000}$	$4.921^{+2.125}_{-1.489}$	$0.948^{+0.020}_{-0.028}$	
C2003T4-20060307	$1.176e + 05^{+1.213e+04}_{-1.176e+05}$	$0.391^{+0.062}_{-0.050}$	$0.000^{+0.000}_{-0.000}$	$0.243^{+0.028}_{-0.023}$	$0.214^{+0.064}_{-0.066}$	$0.152^{+0.089}_{-0.105}$	$3.114^{+0.421}_{-0.423}$	$0.483^{+0.077}_{-0.103}$	
C2004B1-20051015	$1.213e + 04^{+1.375e+04}_{-1.213e+04}$	$0.219^{+0.133}_{-0.125}$	$0.000^{+0.000}_{-0.000}$	$0.430^{+0.236}_{-0.228}$	$0.000^{+0.291}_{-0.000}$	$0.351^{+0.336}_{-0.351}$	$1.325^{+2.624}_{-0.824}$	$0.617^{+0.267}_{-0.617}$	
C2004B1-20060516	$1.065e + 04^{+8.753e+03}_{-1.065e+04}$	$0.231^{+0.155}_{-0.117}$	$0.000^{+0.010}_{-0.000}$	$0.390^{+0.232}_{-0.175}$	$0.000^{+0.283}_{-0.000}$	$0.379^{+0.246}_{-0.379}$	$1.566^{+2.098}_{-0.959}$	$0.622^{+0.233}_{-0.622}$	
C2004B1-20060726	$5.965e + 03^{+4.012e+03}_{-5.965e+03}$	$0.000^{+0.000}_{-0.000}$	$0.145^{+0.126}_{-0.067}$	$0.409^{+0.313}_{-0.163}$	$0.021^{+0.274}_{-0.021}$	$0.426^{+0.207}_{-0.426}$	$1.447^{+1.623}_{-1.062}$	$0.755^{+0.141}_{-0.755}$	
C2004B1-20070308	$2.198e + 04^{+2.318e+03}_{-2.198e+04}$	$0.000^{+0.000}_{-0.000}$	$0.000^{+0.000}_{-0.000}$	$1.000^{+0.000}_{-0.096}$	$0.000^{+0.096}_{-0.000}$	$0.000^{+0.000}_{-0.000}$	$0.000^{+0.106}_{-0.000}$	nan_{nan}^{+nan}	
C2004B1-20070609	$1.044e + 05^{+1.480e+04}_{-1.044e+05}$	$0.561^{+0.110}_{-0.110}$	$0.000^{+0.000}_{-0.000}$	$0.264^{+0.044}_{-0.036}$	$0.000^{+0.000}_{-0.000}$	$0.174^{+0.111}_{-0.149}$	$2.783^{+0.587}_{-0.545}$	$0.237^{+0.137}_{-0.200}$	
C2004Q2	$9.059e + 03^{+6.473e+03}_{-9.059e+03}$	$0.604^{+0.010}_{-0.253}$	$0.000^{+0.000}_{-0.000}$	$0.396^{+0.010}_{-0.165}$	$0.000^{+0.000}_{-0.000}$	$0.000^{+0.418}_{-0.000}$	$1.527^{+1.806}_{-0.065}$	$0.000^{+0.542}_{-0.000}$	
C2006P1-20070504	$1.084e + 05^{+2.880e+04}_{-1.084e+05}$	$0.340^{+0.029}_{-0.079}$	$0.000^{+0.003}_{-0.000}$	$0.605^{+0.043}_{-0.126}$	$0.055^{+0.204}_{-0.055}$	$0.000^{+0.000}_{-0.000}$	$0.654^{+0.437}_{-0.110}$	$0.140^{+0.359}_{-0.140}$	
C2006P1-20070802	$9.605e + 04^{+1.755e+04}_{-9.605e+04}$	$0.000^{+0.000}_{-0.000}$	$0.568^{+0.043}_{-0.093}$	$0.378^{+0.031}_{-0.058}$	$0.054^{+0.150}_{-0.054}$	$0.000^{+0.000}_{-0.000}$	$1.643^{+0.483}_{-0.199}$	$0.087^{+0.213}_{-0.087}$	
C2006P1-20070906	$9.516e + 04^{+2.593e+04}_{-9.516e+04}$	$0.002^{+0.022}_{-0.002}$	$0.088^{+0.035}_{-0.033}$	$0.177^{+0.056}_{-0.036}$	$0.129^{+0.160}_{-0.129}$	$0.604^{+0.133}_{-0.173}$	$4.639^{+1.435}_{-1.346}$	$0.891^{+0.033}_{-0.055}$	
C2006Q1-20070322	$4.917e + 04^{+3.700e+04}_{-4.917e+04}$	$0.125^{+0.181}_{-0.064}$	$0.000^{+0.036}_{-0.000}$	$0.303^{+0.397}_{-0.129}$	$0.572^{+0.179}_{-0.572}$	$0.000^{+0.283}_{-0.000}$	$2.305^{+2.452}_{-1.876}$	$0.821^{+0.101}_{-0.821}$	
C2006Q1-20080117	$3.115e + 04^{+2.121e+04}_{-3.115e+04}$	$0.170^{+0.058}_{-0.094}$	$0.022^{+0.061}_{-0.022}$	$0.710^{+0.095}_{-0.286}$	$0.098^{+0.288}_{-0.098}$	$0.000^{+0.358}_{-0.000}$	$0.409^{+0.952}_{-0.167}$	$0.339^{+0.478}_{-0.339}$	
C2006Q1-20080225	$9.176e + 04^{+1.927e+04}_{-9.176e+04}$	$0.636^{+0.097}_{-0.200}$	$0.000^{+0.084}_{-0.000}$	$0.290^{+0.075}_{-0.058}$	$0.074^{+0.187}_{-0.074}$	$0.000^{+0.042}_{-0.000}$	$2.454^{+0.875}_{-0.712}$	$0.104^{+0.261}_{-0.104}$	
C2006Q1-20080702	$9.104e + 04^{+1.605e+04}_{-9.104e+04}$	$0.000^{+0.005}_{-0.000}$	$0.335^{+0.073}_{-0.057}$	$0.416^{+0.081}_{-0.062}$	$0.085^{+0.105}_{-0.085}$	$0.165^{+0.131}_{-0.165}$	$1.405^{+0.421}_{-0.390}$	$0.427^{+0.141}_{-0.233}$	
C2006Q1-20080709	$1.570e + 05^{+3.622e+04}_{-1.570e+05}$	$0.488^{+0.103}_{-0.088}$	$0.096^{+0.085}_{-0.066}$	$0.192^{+0.048}_{-0.036}$	$0.066^{+0.100}_{-0.066}$	$0.159^{+0.130}_{-0.159}$	$4.208^{+1.200}_{-1.039}$	$0.278^{+0.155}_{-0.224}$	
C2007N3	$6.137e + 04^{+3.569e+04}_{-6.137e+04}$	$0.205^{+0.101}_{-0.087}$	$0.000^{+0.005}_{-0.000}$	$0.490^{+0.207}_{-0.180}$	$0.030^{+0.223}_{-0.030}$	$0.275^{+0.240}_{-0.275}$	$1.041^{+1.183}_{-0.607}$	$0.598^{+0.231}_{-0.598}$	
C2008T2	$1.481e + 04^{+3.171e+02}_{-1.481e+04}$	$0.225^{+0.052}_{-0.056}$	$0.056^{+0.039}_{-0.037}$	$0.719^{+0.020}_{-0.019}$	$0.000^{+0.000}_{-0.000}$	$0.000^{+0.000}_{-0.000}$	$0.391^{+0.038}_{-0.037}$	$0.000^{+0.000}_{-0.000}$	

^aDefined as $f_{silicates}^{cryst} \equiv (\text{crystalline})/(\text{crystalline} + \text{amorphous})$.

unique identifications of minerals from just the far-infrared, with comet C1995 O1 (Hale-Bopp) being an exception. The mineral features in the 10 μm region are key in mineralogical identifications but also these vibrational stretching modes overlap such that the Mg:Fe content, crystal shape, and grain size all affect the range and co-dependence of fitted model relative mass fractions. In the far-infrared, the vibrational bending modes of crystalline olivine and crystalline pyroxene, as well as amorphous Mg:Fe olivine and pyroxene, occur at more distinctive wavelengths than in the mid-infrared. When the full wavelength range is available then the mineralogical identification is more secure. Extended spectral coverage provided by the longer wavelengths is used to better constrain grain parameters such as the slope of the grain size distribution and the porosity parameter D . Differences between model results obtained by using SLLL versus SLLL–SL SED fits are evident as shown in Figure 3.

There are 22 comet spectra with SLLL and 20 comet spectra with SL, and both with $r_h \lesssim 3.5$ au. We will motivate why we analyze these models as 22 SLLL with $r_h \lesssim 3.5$ au.

4.3. Analysis restricted to $r_h \lesssim 3.5$ au

We restrict analyses of thermal models to $r_h \lesssim 3.5$ au. For $r_h \geq 3.5$ au, the thermal model parameters may exhibit degeneracies between amorphous carbon and amorphous silicates in the mid-infrared. For example, degeneracies in model parameters in SLLL–SL spectra are apparent when comparing SLLL spectra to SLLL–SL spectra; at $r_h \geq 3.5$ au the shape of the short wavelength onset of the 10 μm amorphous pyroxene may be degenerate with the shape of the thermal rise of the significantly warmer amorphous carbon emission. Representative example of this complication is illustrated in Figure 4 for comet C2006P1-20070906 (C/2006 P1 (McNaught)) at $r_h = 4.0$ au, where amorphous carbon dominates the model fitted to the full

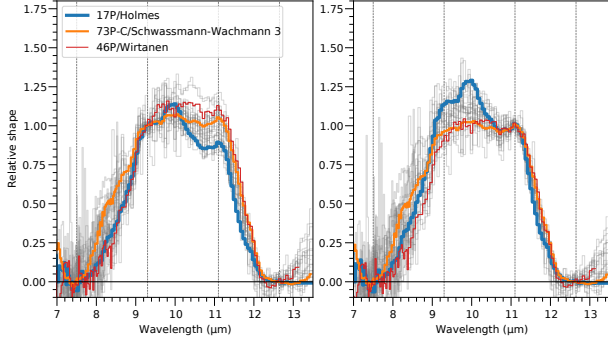


Figure 1. Comparison of 10- μm silicate emission feature shapes: (left) the feature is normalized to 1.0 at 9.3 μm , (right) the feature is normalized to 1.0 at 11.1 μm , regions devoid of sharp resonances. All spectra with well-defined silicate bands are shown as thin gray lines. Comets 9P/Tempel 1, 17P/Holmes, and 73P/Schwassmann-Wachmann 3-C are highlighted with thick lines of varying width and color. The complete figure set highlighting each spectrum individually (26 spectra in all), including uncertainties, is available in the online journal.

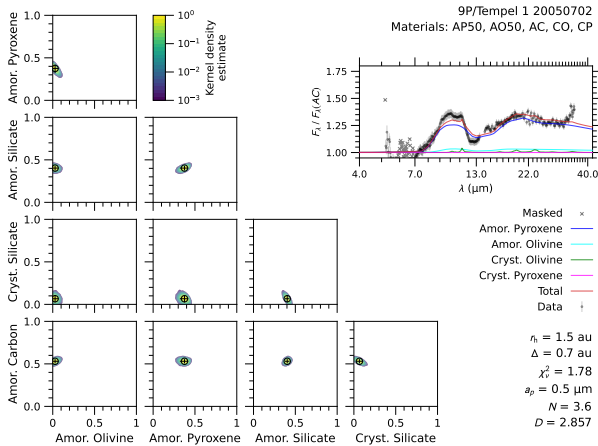


Figure 2. Model best-fit and parameter correlations based on our Monte Carlo (bootstrap) spectral fit trials. In the upper right spectrum, the grey filled dots are the spectral data points used in the fit, while the grey ‘x’ are the spectral data that are masked for fitting purposes. The upper-right inset is the spectral data normalized by the best-fit amorphous carbon model, $F_{\lambda}(AC)$. Each model component is also shown normalized by $F_{\lambda}(AC)$. The silicate models are offset by +1 for clarity. The complete figure set (55 images for all comet spectra modeled for the survey) is available in the online journal. (The data used to create the figure(s) in the upper right are available.)

wavelength range (SLLL). In contrast, the models fit to solely the mid-infrared (SLLL–SL) is better reproduced by amorphous olivine. Thermal models for (SLLL) full wavelength spectra resolves this degeneracy (Sections 4.2, 4.9.2) by as-

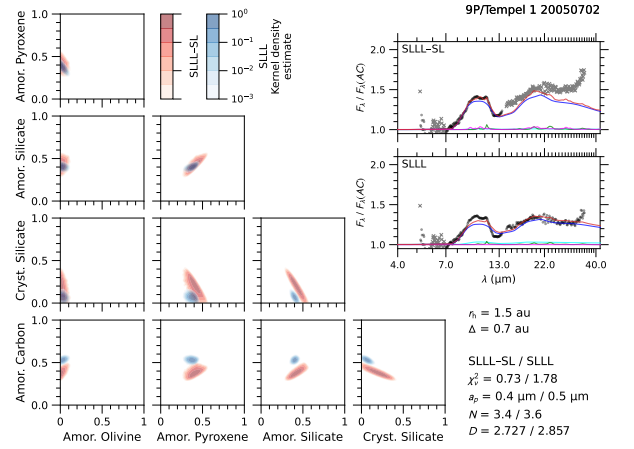


Figure 3. Same as Figure 2 but for comparisons of model compositions based on fits to the full-wavelength range (SLLL) to those based on fits to a limited wavelength range (SLLL–SL). The model results are shown as filled contours based on a kernel density estimate: SLLL–SL in red, SLLL in blue. The contour shading is log-scaled as indicated by the color bars. In the upper right, the spectra and their best-fits are shown after normalization with the amorphous carbon model spectrum in order to emphasize spectral features from silicates. In these panels the grey filled dots are the spectral data points used in the fit, while the grey ‘x’ are the spectral data that are masked for fitting purposes. For most comet spectra, the SLLL–SL and SLLL fits are generally comparable, with systematic decreases in amorphous carbon (AC), as well as anti-correlated changes in crystalline silicates (CP) and correlated changes in Amorphous Silicates (AS), see section 4.3. Generally, SLLL–SL fits have larger 3σ ranges of parameters and significantly lower AICc values (see text). The complete figure set (31 images) is available in the online journal. (The data used to create the figure(s) in the upper right are available.)

sessing the shape and contrast of the 20 μm amorphous pyroxene band.

4.4. Analysis restricted to $2.7 \lesssim D \lesssim 3.0$

Grain fractal porosity (D) is an important thermal model parameter. It is a parameter that captures the fact that cometary grains are aggregate structures. Sample analysis in situ in terrestrial laboratories and comet rendezvous encounters corroborate this physical state (Bockelée-Morvan et al. 2017a,b; Brownlee et al. 2006).

Models with $D = 2.6$ and $a_{peak} \geq 1.5 \mu\text{m}$, in our view, yield unrealistically high f_{cryst} or crystalline silicates (CS) values. Highly porous particles approach the behavior of their monomers both in their higher particle temperatures (Harker et al. 2002) and their higher spectral contrast features (Kolokolova et al. 2004). Highly porous particles with $a_{peak} \geq 1.5 \mu\text{m}$ can contribute to the SEDs and spectral features. In thermal models with $D = 2.6$ compared to $D = 2.7$ or $D = 2.8$, less of the mass fraction is required to fit the fea-

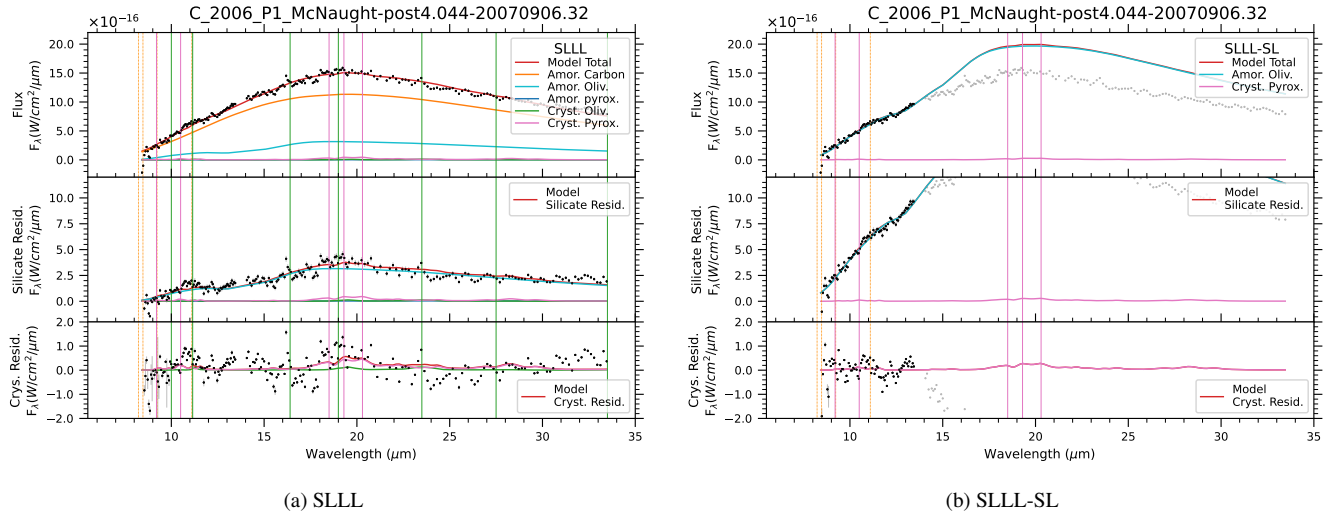


Figure 4. C2006P1-20070906 (C/2006 P1 (McNaught)) at $r_h = 4.0$ au (two models, in flux density ($\text{W m}^{-2} \mu\text{m}^{-1}$) versus wavelength (μm), showing how models can exhibit degeneracies for comets at $r_h \geq 3.5$ au. Degeneracies in parameters for models may occur between amorphous carbon and amorphous silicates at these r_h . Each figure consists of 3 panels, where the top is the observed spectra (black symbols) and thermal model dust decomposition, the middle panel the residual silicate (brown solid line), defined as the total thermal model spectra (red solid line in each panel) minus the contribution from amorphous carbon (orange solid line in each panel), while the bottom panel the residual crystalline fraction (steel blue solid line) defined as the total thermal model flux minus the sum of the amorphous carbon + amorphous olivine (cyan solid line in each panel) + amorphous pyroxene (blue solid line in each panel) components. (a) Model fitted to SLLL, dominated by amorphous carbon with some contribution from amorphous silicates. (b) Model fitted to SLLL–SL, fitted solely by amorphous olivine. The vertical lines designate the wavelength position of features from various refractory species (from the left to the right) at: 9.30 (pink; crystalline pyroxene); 8.20 and 8.47 (olive; PAH features), 10.05 (green; crystalline olivine), 10.50 (pink; crystalline pyroxene), 11.15 (green; crystalline olivine), and $19.50 \mu\text{m}$ (green; crystalline olivine). The latter feature is also near the order splicing of the IRS. Derived model parameters are inset top right. (The data used to create these figures are available.)

ture contrast for amorphous materials because highly porous particles produce higher contrast resonances in SEDs, which results in a significantly higher portion of the mass fraction being assigned to the solid crystals. In our thermal models of ensembles of discrete materials, the solid crystals only contribute to particle radii (ellipsoidal effective radii) of $0.1\text{--}1 \mu\text{m}$ (as solid crystals larger than this effective radii fail to match the observed spectral features, Lindsay et al. 2013). Solid crystals will yield a high mass fraction ($f(\text{co})$ or $f(\text{cp})$) compared to the porous amorphous carbon ($f(\text{ac})$) or amorphous silicates ($f(\text{ao}50)$, $f(\text{ap}50)$). Each crystal produces relatively less thermal emission than porous amorphous particles of similar radii, even if the optical properties are similar. For instance, a representative case is provided by examining the optical constants of crystalline Mg:Fe-olivine (fayalitic) compared to those of amorphous Mg:Fe-olivine, with the caveat that spectral features of fayalitic olivine are not yet identified in cometary spectra despite their presence in Stardust return samples (Frank et al. 2014a). Thus, we restrict thermal models to consider amorphous materials with fractal dimensions in the range $2.7 \lesssim D \lesssim 3.0$.

Omitting $D = 2.6$ only omits the best-fit model for comet 17P (SLLL) and one best-fit model (SL) for comet 73P-

C/SW3 (1.267 au). In some comets higher porosity grains are known to exist. For comet 67P, Rosetta’s in-situ investigations suggest that higher porosity particles comprise $\sim 25\%$ by number (Bockelée-Morvan et al. 2017a,b). The imaged extremely porous (fractal-like, Güttler et al. 2019) hierarchical aggregates comprise only a handful of Rosetta particles measured with the Micro-Imaging Dust Analysis System (MIDAS) atomic force microscope (Mannel et al. 2016). Of the 22 SLLL models as well as those models constrained to fit only SLLL–SL, the majority of models are best-fit with $D = 2.7$ (see Table 3), with 10 of 22 for SLLL and 13 of 20 for SL.

For the Spitzer survey models, best-fit HGSD parameters (a_p , D , N) are distinguishable with 95% or greater confidence from non-best-fit choices of HGSD parameters. A positive correlation exists between higher porosity (lower D) and larger a_p and larger N because increase in porosity causes increased particle temperatures whereas an increase in a_p results in lower particle temperatures for the grain size distribution and a steepening of the slope lessens the emphasis on the largest and coolest particles. Figure 5 shows the HGSD parameters of slope N versus peak grain size a_p (in

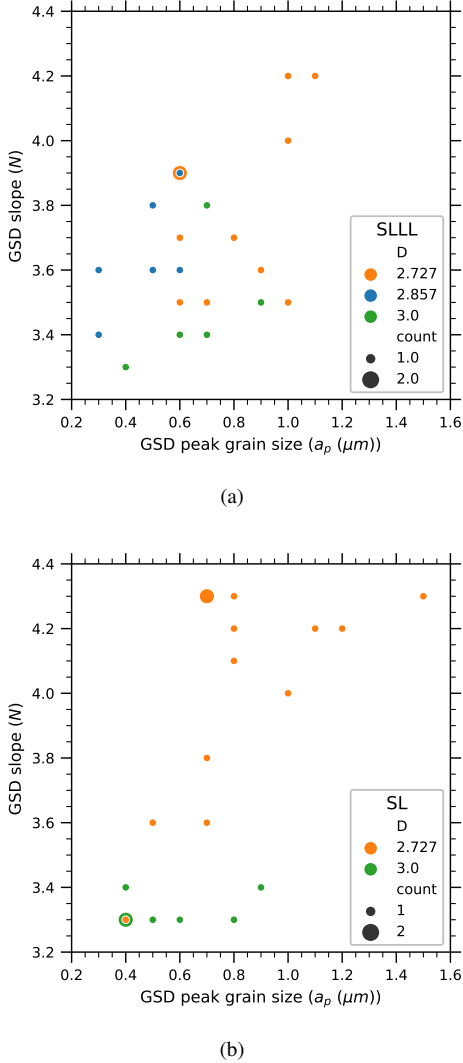


Figure 5. Grain size distribution slope (N) versus peak grain size, a_p (μm), colored by porosity parameter D that characterizes the amorphous materials. (a) SLLL models. (b) SL models.

μm) and colored by D for best-fit SLLL models and SL models to demonstrate their relationship with D .

4.5. Sensitivity to fitted wavelength ranges

The Akaike Information Criterion (AICc; Appendix A) may be used to compare the relative suitability of two different model analyses of the same spectrum, or model analyses of two renditions of the spectra. In our analysis, we have used the AICc to demonstrate that even though models fitted to fewer data points in SLLL–SL may have lower χ^2_ν , these models have less information than models fitted to SLLL.

The relative likelihood of SLLL–SL referenced to SLLL, i.e., the probability that the SLLL–SL model minimizes the (estimated) information loss is $\exp((AIC_{SLLL} -$

$AIC_{SLLL-SL})/2) = \exp(\Delta AICc/2)$. On average, for a subset of 20 of the 22 comet spectra, $\Delta AICc = -514 \pm 186$, so the probability that the SLLL–SL minimizes the information loss is an extremely small probability. However, comet 9P/Tempel 1 has a $\Delta AICc = 4.5$, so the SLLL–SL model fits the data better than the SLLL model. The SLLL model has insufficient crystalline silicate flux in the $10 \mu\text{m}$ feature, or alternatively, the model predictions of the far-infrared crystalline features are in excess of the observed flux. Thus, a larger mass of crystals is excluded from the SLLL model fit. An extreme exception is comet 17P/Holmes (Section 4.11.1), which is discussed later, where $\Delta AICc = 468$ so the SLLL–SL model fit is superior to SLLL model.

In some comets, there appears to be some emission in the $13.5\text{--}15.7 \mu\text{m}$ region, which is not attributable to the Si–O vibration modes in Mg-crystalline and amorphous Mg:Fe silicates and therefore not predicted by the thermal model. For only a handful of comets is the ‘ $14.5 \mu\text{m}$ ’ emission strong enough to affect the thermal model fitting of the mid-infrared $10 \mu\text{m}$ silicate features, which typically extend to about $12.8\text{--}13.2 \mu\text{m}$, and the far-infrared silicate features, which include the $16.5 \mu\text{m}$ crystalline olivine peak. To assess whether the model fitted to SLLL without the $13.5\text{--}15.7 \mu\text{m}$ data points minimizes the information loss, we assess whether $\exp(\Delta AICc/2) \geq 0.1$ or $\Delta AICc \geq -4.6$, i.e., if the relative probability of the model with fewer data points is greater than 0.1 then that model cannot be ruled out. The comets with $\Delta AICc \geq -4.6$ include: 78P, 88P, C2003K4-20050913, C2003T4-20051122, and C2006P1-20070802. Vibration modes of minerals with Ti–O and Al–O bonds occur near these wavelengths but modeling this $\sim 14.5 \mu\text{m}$ emission is beyond the scope of this paper.

In Figure 6, we present these five spectra, normalized by their best-fit thermal models to emphasize the unidentified spectral feature. The feature spans two of the spectral settings (SL1 and LL2), from 12 to $17 \mu\text{m}$, with a peak around $14.45 \mu\text{m}$. Two additional spectra are shown, 67P-20081128.38 and 37P, for comparison. The feature may also be present in these additional data, but at a weaker level.

4.5.1. Model parameters and wavelength coverage

Roughly half of the IRS spectra in this survey are observed with the SL module only, and lack the far-infrared spectral coverage that LL observations would have provided. To increase the sample size, the thermal models for the SL need to be placed in context with the thermal model parameters for SLLL. Furthermore, the systematic differences in the model parameters between full wavelength coverage and only mid-infrared need to be evaluated and discussed. In many circumstances, especially non-space based observatories, spectra of comets are obtained only in the mid-infrared.

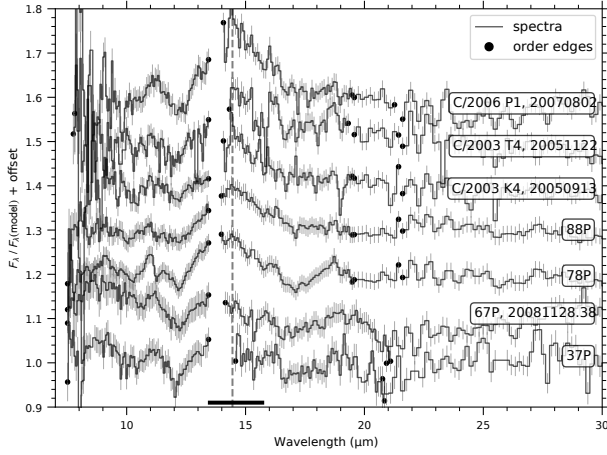


Figure 6. Unidentified 14- μm feature. Seven spectra have been normalized by their best-fit thermal models to emphasize deviations from the model. Five of the spectra (C/2006 P1, C/2003 T4, C/2003 K4, 88P, and 78P) were identified with our Akaike Information Criterion (AIC) tests, which compared model fits with and without the spectral data from 13.5–15.7 μm (marked with a thick horizontal bar). A vertical dashed line marks a proposed feature peak at 14.45 μm . Two additional high-quality spectra (67P and 37P) are shown for comparison. These additional comets may also have evidence for a weak feature.

Table 5 gives the median, mean, and standard deviation for the sets of models designated by SLLL, SLLL–SL, SL, and SLLL–SL & SL (combined), employing the thermal model mean parameters for each model for a designated comet and epoch. In principle, compositional variant populations may be revealed from modeling studies of a large sample of comets. The standard deviations of the model population’s composition parameters are large, so we investigate the cumulative distribution functions (CDF) for each parameter and apply the Kolmogorov-Smirnov (KS) test to compare the distributions of comae dust compositions revealed by the thermal models fitted to SLLL, SLLL–SL, SL, and SLLL–SL & SL (combined) data sets, where SLLL and SLLL–SL are for the same set of spectra and SL is a distinct set of comets.

Taking crystalline pyroxene $f(\text{cp})$ for example, the median and mean of SLLL shows SLLL–SL and SL have greater mass fractions than for SLLL. The KS test passes for $f(\text{ao50})$ and $f(\text{ac})$ while the KS tests fails in other model parameters so when considering all the parameters the SLLL and SL are not drawn from the same distribution of models (Table 5). For model pairs of SLLL–SL and SLLL, forming the differences between model pair parameters, namely SLLL–SL minus SLLL, shows that there is a decrease in amorphous carbon, together with changes in the crystalline silicates that are anti-correlated with changes in amorphous silicates. The response of the thermal models to fitting a wavelength range limited to SL reveals the interplay between the changes in

the grain size distribution parameters a_p and slope N , the changes of which are positively correlated (if a_p is larger, then the slope N is steeper), as well as changes in compositional mass fractions.

We consider the possibility that the model’s predictions of the spectral behavior of the thermal emission from crystalline pyroxene in cometary comae may be better predicted in the SLLL–SL spectral range compared to the SLLL full spectral range as a component to understanding the model’s response of fitting greater mass fractions of crystalline pyroxene to SLLL–SL models compared to the SLLL models. Our choice of optical constants for crystalline ortho-pyroxene is consistent with other modelers of cometary SEDs. However, optical constants for crystalline pyroxene do show variation (Jäger et al. 1998; Chihara et al. 2001; Juhász et al. 2009; Enggrand et al. 2023) with significant variations depending on ortho-pyroxene versus clino-pyroxene and depending on Fe-content. Given these caveats about crystalline pyroxene and the co-dependence of grain size distribution parameters and compositional mass fractions, the population of models for SL-only are combined into SLLL–SL & SL and presented here for consideration.

4.5.2. Fitting outcomes as represented by six comets

Selecting six comet spectra from the survey ensemble, the differences between models fitted to SLLL and SLLL–SL can be highlighted. These six comet spectra include crystalline olivine rich $f(\text{co}) > 0.1$, crystalline pyroxene rich $f(\text{cp}) > 0.1$, and crystal poor $f(\text{co}) < 0.1$ and $f(\text{cp}) < 0.1$. Figure 7 shows in the left panel the comet spectral silicate residual and model silicate residual and in the right panel the comet spectral crystalline silicate residual and the model crystalline silicate residual (Figure 7(a) is SLLL; Figure 7(b) is SLLL–SL). The silicate residual is defined as the modeled amorphous carbon subtracted from the observed flux $\text{resid}_{\text{sil}} = [\text{flux} - \text{flux}(\text{ac})]$, and the crystalline silicate residual, is defined as the modeled amorphous carbon plus modeled amorphous silicates subtracted from the observed flux $\text{resid}_{\text{cryst}} = [\text{flux} - (\text{flux}(\text{ac}) + \text{flux}(\text{ao50}) + \text{flux}(\text{ap50}))]$.

The 11.15–11.2 μm peak is well fit by a crystalline olivine component, which also produces two of the three resonances at $\lambda \gtrsim 15 \mu\text{m}$ (16.5 μm , 19.5 μm , 23.5 μm , 27.5 μm , and 33.5 μm). The three crystalline olivine peaks span the width of the far-infrared amorphous olivine feature. The shorter wavelength far-infrared resonance (16.5 μm , 19.5 μm) can be affected by the emission features from the far-infrared amorphous silicate bands. The two or three far-infrared crystalline pyroxene peaks occur nearly spectrally coincident with the far-infrared amorphous pyroxene feature and at slightly longer wavelengths than the far-infrared amorphous olivine feature. Even if a weak contribution, the relative mass fraction of crystalline pyroxene is significant if the

Table 5. Statistical summary of model parameters for different spectral data sets.

Statistic	Set 0	Set 1	Set 2	f(ap50)	f(ao50)	f(co)	f(cp)	f(ac)	AS	CS	f_{cryst}
Median	SL			0.409	0.000	0.070	0.124	0.439	0.409	0.173	0.305
Mean	SL			0.367	0.025	0.067	0.125	0.416	0.393	0.191	0.326
Std.	SL			0.173	0.052	0.063	0.126	0.145	0.156	0.130	0.217
Median		SLLL		0.194	0.136	0.044	0.000	0.535	0.337	0.088	0.196
Mean		SLLL		0.186	0.147	0.056	0.067	0.544	0.333	0.123	0.250
Std		SLLL		0.137	0.132	0.060	0.124	0.164	0.137	0.125	0.224
Median			SLLL-SL	0.328	0.000	0.079	0.188	0.345	0.352	0.321	0.496
Mean			SLLL-SL	0.332	0.017	0.083	0.210	0.358	0.349	0.293	0.465
Std			SLLL-SL	0.180	0.037	0.061	0.154	0.142	0.191	0.171	0.260
Median			SLLL-SL & SL	0.358	0.000	0.076	0.158	0.393	0.374	0.239	0.387
Mean			SLLL-SL & SL	0.349	0.021	0.075	0.169	0.386	0.370	0.245	0.399
Std			SLLL-SL & SL	0.175	0.045	0.062	0.146	0.145	0.174	0.159	0.248
KS ^a pair		SLLL	SLLL-SL	0.020	0.001	0.394	0.001	0.007	0.872	0.007	0.007
KS pair		SLLL	SL	0.012	0.001	0.869	0.080	0.009	0.109	0.133	0.246
KS pair		SLLL-SL	SL	0.518	0.995	0.820	0.216	0.312	0.518	0.125	0.133
KS pair		SLLL	SLLL-SL & SL	0.003	0.000	0.472	0.002	0.001	0.221	0.013	0.056
KS pair		SLLL (JFC)	SLLL (OCC)	0.961	0.705	0.803	0.841	0.754	0.094	0.656	0.754
KS pair		SLLL-SL (JFC)	SLLL-SL (OCC)	0.325	1.000	0.371	0.878	0.239	0.754	0.878	0.705
KS pair		SL (JFC)	SL (OCC)	0.897	0.998	0.091	0.214	0.324	0.324	0.324	0.743
KS pair		SLLL-SL & SL (JFC)	SLLL-SL & SL (OCC)	0.300	0.935	0.273	0.273	0.386	0.386	0.700	0.508
KS pair		SLLL (JFC)	SLLL-SL & SL (JFC)	0.002	0.000	0.258	0.009	0.006	0.602	0.034	0.097
KS pair		SLLL (OCC)	SLLL-SL & SL (OCC)	0.211	0.136	0.800	0.373	0.087	0.319	0.438	0.681
KS pair		SLLL (JFC)	SLLL-SL (JFC)	0.016	0.001	0.751	0.005	0.016	0.963	0.016	0.045
KS pair		SLLL (OCC)	SLLL-SL (OCC)	0.873	0.357	0.357	0.357	0.357	0.873	0.357	0.357
KS pair		SLLL (JFC)	SL (JFC)	0.011	0.011	0.216	0.372	0.076	0.556	0.237	0.237
KS pair		SLLL (OCC)	SL (OCC)	0.165	0.235	0.851	0.769	0.126	0.316	0.769	0.997
KS pair		SLLL-SL (JFC)	SL (JFC)	0.766	0.996	0.641	0.086	0.216	0.766	0.147	0.237
KS pair		SLLL-SL (OCC)	SL (OCC)	0.586	0.963	0.235	0.851	0.769	0.586	0.586	0.500
KS pair		SLLL (JFC)	SLLL-SL & SL (JFC)	0.002	0.000	0.258	0.009	0.006	0.602	0.034	0.097
KS pair		SLLL (OCC)	SLLL-SL & SL (OCC)	0.211	0.136	0.800	0.373	0.087	0.319	0.438	0.681

^aKolmogorov-Smirnov (KS) test pair probability or pvalue (see text Section 4.6.1).

far-infrared crystalline pyroxene features successfully can be fitted by the model.

To show the model parameters and how they change depending on the wavelength range for the six comet spectra in Figure 7, the ternary diagram, first in 3-D and then in 2-D, is introduced. Projecting the 5-dimensional parameter space onto 3-dimensions enables visualization of the shifts in relative mass fractions between models fitted to SLLL and SLLL-SL. Using the definitions $CS=f(co)+f(cp)$ and $AS=f(ao50)+f(ap50)$, and simply $AC=f(ac)$, the model parameters are shown in Figure 8 as coordinates a 3-dimensional space to demonstrate that they lay in a 2-dimensional plane because $AC+AS+CS=1$ (by definition of relative mass fractions). Model parameters for SLLL are

squares and SLLL-SL are circles with arrows showing the shifts between SLLL and SLLL-SL.

Rods perpendicular to the 2-d plane in 3D-space show the summands of amorphous silicates and the summands of crystalline silicates (Figure 8(a), and $f(co)$ and $f(cp)$ in Figure 8(b)). Between SLLL and SLLL-SL, crystalline olivine may increase and often crystalline pyroxene increases; amorphous olivine decreases and amorphous pyroxene increases because the short wavelength shoulder of the Spitzer IRS SL mode is systematically better fitted by amorphous pyroxene.

For each of the six comets, shifts in model parameters between for SLLL and for SLLL-SL are shown by squares for SLLL and circles for SLLL-SL as well as shown by dots are a randomly selected 1K subset of the 10K MC trials, Fig-

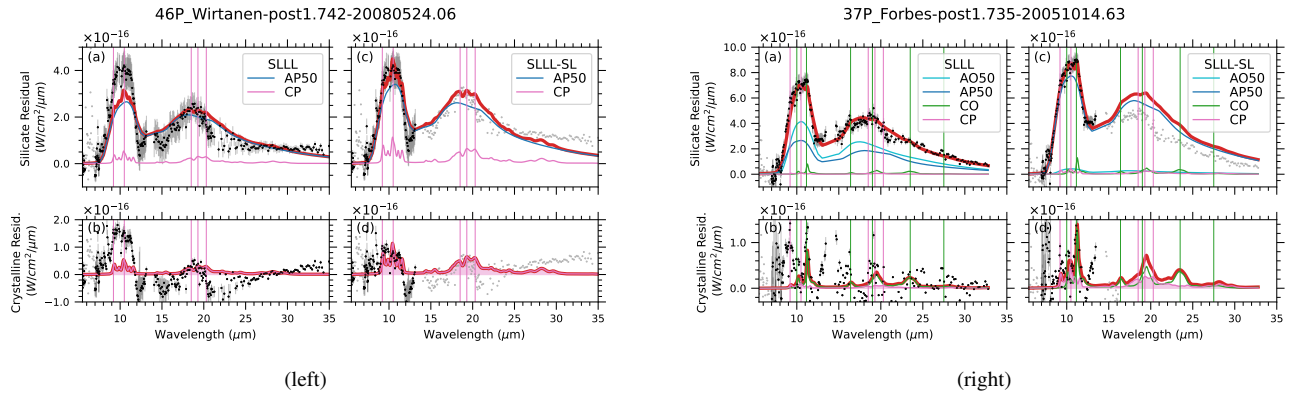


Figure 7. Crystalline features constrained by thermal modeling fitting for comets 46P/Wirtanen (right) and 37P/Forbes (left). (a, b) SLLL. Models using the mid- and far-infrared SEDs. (c, d) SLLL–SL. Models using the mid-infrared SEDs. Upper panels (a, c) show the silicate residuals for the comet spectra (black points with error bars) and for the thermal model silicate residual and its decomposition. Points without error bars (gray) are not used in the fit, e.g., the ν_2 bands of water and restricted wavelengths for SLLL–SL. The lower panels (b, d) present the silicate crystalline residuals. The vertical colored lines are at positions of mineral resonances. The solid lines depict the contribution to the total residual (solid red line) of the silicate dust component comprising submicron crystalline olivine (green) and crystalline pyroxene (pink), and amorphous olivine (cyan), and amorphous pyroxene (blue). Model fitting SLLL–SL yields increased contrasts in the crystalline features and higher crystal mass fractions. A complete figure set for six comets is available in the online journal.

ure 8(c) and (d). For a given comet, the shape of parameter correlations are preserved but the domains in parameter space defined by models for SLLL are more compact, reflecting the smaller 2σ uncertainties (95% extrema of the trials) for SLLL models for these comets (Table 5). The SLLL models, which have tighter parameter confidence intervals, are proven to have higher information content than their SLLL–SL counterpart models by application of the AICc. Analysis of the SLLL models, which have tighter parameter confidence intervals, are the focus of this paper.

4.5.3. Model correlation analyses for SLLL

There are no positive correlation values greater than 0.8 between model mass fraction parameters for SLLL. Spearman Rank tests provide the correlation matrix values and permutation tests yield the correlation p-values. Figure 9 shows the correlation matrix with check marks for parameter combinations with p-values lower than 0.003 (97.7%) used to reject the null hypothesis. When the probabilities are too low for a random chance for there to be a correlation, the values of the correlation for the subset of parameters is in Table 6.

There is a moderate positive correlation between $f(\text{cp})$ and derived model parameter CS. Specifically, by doing Spearman Rank tests (computing the correlation matrix), we find $f(\text{cp})$ is anti-correlated with $f(\text{ap50})$ with a moderate value for the correlation parameter of -0.70 . There is an anti-correlation between $f(\text{co})$ and $f(\text{ac})$: modeled comets with higher amorphous carbon have less crystalline olivine. This is commensurate with a bulk compositional study of anhydrous IDPs that shows higher mineral modality of crystalline olivine is correlated with lower wt% of carbon ($\lesssim 10$ wt%) (Thomas et al. 1993a). Other plots show $f(\text{co})$ does not

Table 6. Spearman Rank Correlation Values^a

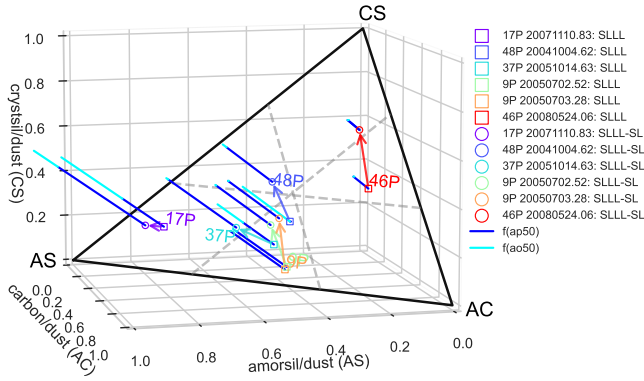
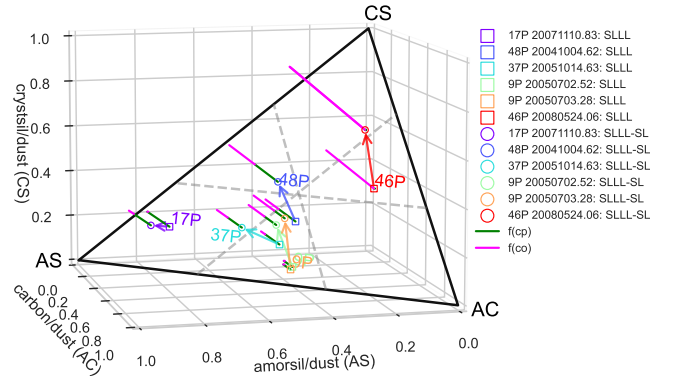
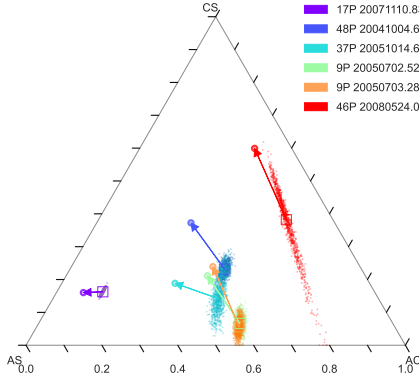
	$f(\text{ac})$	$f(\text{cp})$
$f(\text{co})$	-0.62	...
CS	-0.77	0.79
$f(\text{ap50})$...	-0.70

^aSpearman Rank correlation values considered not attributable to random chance at 3σ for parameters in the set of SLLL models.

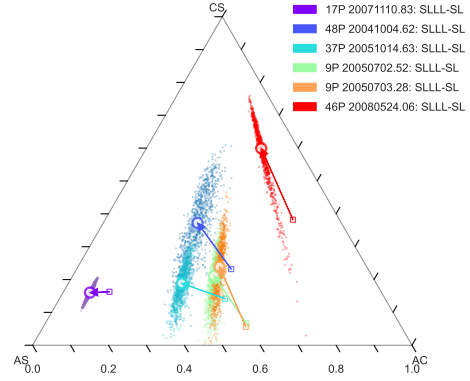
change its KDE (kernel density estimation) from SLLL to SLLL–SL and SL; $f(\text{cp})$ is not correlated with $f(\text{co})$ in SLLL. Otherwise, correlations and anti-correlations are as expected from correlations of model parameters being mass fractions. This is shown by the full range of parameters spanned by the Monte Carlo trials in Figure 9(c).

4.6. Dynamical Taxonomy

The large sample of comets modeled herein enables a robust assessment of whether comets have a taxonomy based on refractory species composition and their relative abundances fractions as measured in the coma. This proposition can be explored through a variety of statistical tests. An underlying key question to address with this survey of Spitzer comets is whether Jupiter-family (JFCs, Eccentric comets) and Oort cloud comets (OCCs, Isotropic comets), two different dynamical families, have similar, or dissimilar, mineralogies and grain properties. Such a comparison can give insight to

(a) SLLL \rightarrow SLLL-SL, amor. sil. rods(b) SLLL \rightarrow SLLL-SL, cryst. sil. rods

(c) SLLL (1K MC trials)



(d) SLLL-SL (1K MC trials)

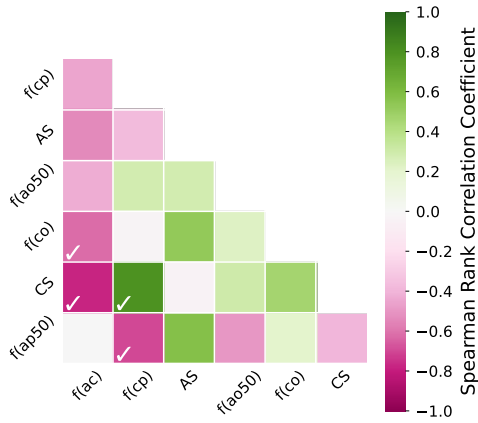
Figure 8. Projection into 3D and 2D ternary diagram of five model parameters for six comets showing changes in fitted parameters from SLLL to SLLL-SL (Figure 7). From SLLL to SLLL-SL (*shown by arrows*), crystalline silicates (CS) increase and amorphous carbon (AC) decreases, where (a, b) respectively show the changes in amorphous silicates and crystalline silicates by rods perpendicular to the {AC, AS, CS} plane in 3D. (c, d) Ternary diagrams showing changes from SLLL \rightarrow SLLL-SL, with mean model parameters as points and extent of 1000 (1K) subset of 10,000 (10K) Monte Carlo (MC) trials as dots. SLLL parameter space is less tightly constrained compared to SLLL-SL (see Section 4.5).

conditions in the early protosolar nebula, including the mixing of inner disk material into outer comet forming zones. JFCs and OCCs occupy similar regions of model parameter space in terms of relative mass fractions. A KS test comparing JFCs and OCCs does not identify any significant difference, Table 5.

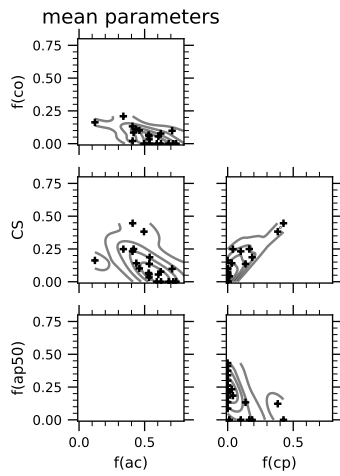
4.6.1. Dynamical populations: KS test of model sets

The Kolmogorov-Smirnov (KS) test can be used to assess if two collections of models are drawn from different populations. If the probability or pvalue of the KS test is less than 0.01 (1%) then the null hypothesis (a claim that the models are not drawn from different populations) can be rejected,

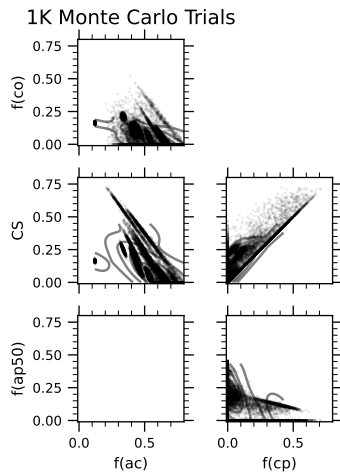
and the conclusion that the two model collections are statistically different may be reached. Sometimes 5% is used. When the pvalue is high then we cannot say that they are not drawn from the same distribution but rather say that the



(a)



(b)



(c)

Figure 9. Spearman Rank Tests (for Correlations). (a) The Spearman rank test correlation matrix for each of SLLL, with \checkmark marks where pvalue (Permutation Test) is <0.003 (3σ). (b) The kernel density distribution (KDE) plots for mean parameters for those parameter pairs where the '+' marks indicate those with permutation test pvalue <0.003 (3σ). (c) The KDE for 1000 Monte Carlo trails.

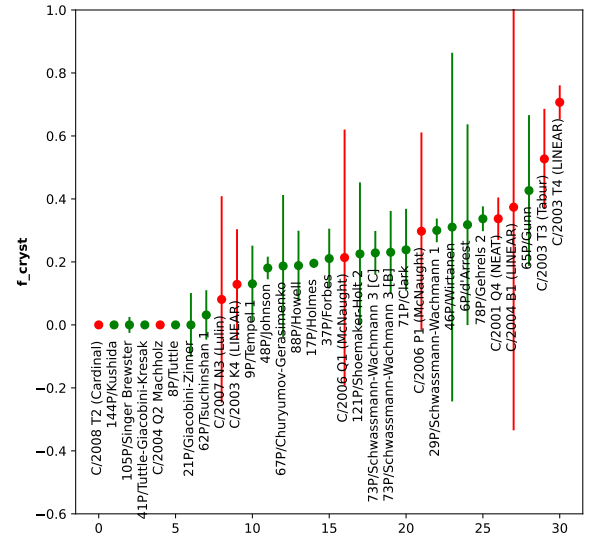


Figure 10. The derived silicate crystalline mass fraction, f_{cryst} . Filled red circles are Oort cloud comets, filled green circles are Jupiter-family comets, where each point represent the average values over all observations for the parameter f_{cryst} if multiple observations of the same comet were obtained. The vertical bars represent the range of f_{cryst} within the 95% confident interval.

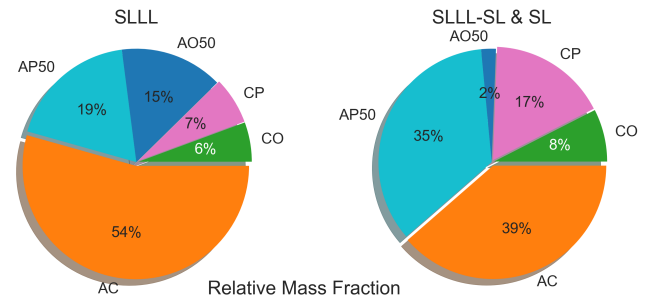


Figure 11. Relative mass fraction of five primary materials in cometary comae derived from the Spitzer comet survey. Left. SLLL. Amorphous carbon (AC) is $> 50\%$, dominating the mass fraction. Right. Combined (SLLL–SL and SL). AC is greater than one-third and is comparable to the amorphous silicate mass fraction, and the crystalline silicates (CS) (sum of the crystalline pyroxenes [CP] and crystalline olivine [CO] components) comprises 25%. The increase in CS from SLLL to (SLLL–SL & SL) is 12% to 25%, or an increase by a factor of 2. AC is a highly absorbing carbonaceous species. There could be more carbon in organics that are not as highly absorbing as AC. However, spectroscopic observations that take full advantage of JWST's S/N ratio and superior spectral resolution are necessary in order to potentially detect weaker features from organics. A complete figure set of the relative mass fraction of the five primary materials for each individual comet (some observed at multiple epochs) is available in the online journal.

distributions are not distinguishable. Table 5 shows the KS test for pairs of models (set 1 and set 2) for the five model mean parameters or mean relative mass fractions $\{f(\text{ap50}), f(\text{ao50}), f(\text{co}), f(\text{cp}), f(\text{ac})\}$, and for the sum of amorphous silicates $\text{AS} \equiv f(\text{ap50})+f(\text{ao50})$ and of crystalline silicates $\text{CS} \equiv f(\text{co})+f(\text{cp})$.

Although we focus primarily on interpreting the model outcomes from SLLL alone (section 4.5.3) for completeness we briefly comment on interpretative outcomes from the other wavelength fitted ranges contained in Table 5. For the set 1 and set 2 pair being (SLLL, SLLL–SL), the parameters that pass the KS test and thereby show significant differences include $\{f(\text{ao50}), f(\text{cp}), f(\text{ac})\}$. For the set 1 and set 2 pair being SLLL and SL, the parameters that show significant differences include $\{f(\text{ao50}), f(\text{ac})\}$. Only for the set 1 and set 2 pair of SLLL–SL and SL is no difference found in any parameter, and therefore we proceed with the analysis forming the SL-only data set from SLLL–SL & SL.

The contrast of the silicate spectral features depends on the particle size and the silicate-to-amorphous carbon ratio. Weak spectral features from crystalline silicates contribute at multiple wavelengths. With the S/N presented in the Spitzer spectra, even silicate features of low spectral contrast can reveal the mineralogy of amorphous and crystalline components. The thermal model fitting accounts for the grain size distribution dependence and radial-heliocentric dependence when deriving the relative mineral mass fractions. Thus, we discuss taxonomy based on the the model parameters of relative mass fractions.

4.7. Silicate crystalline mass fraction

Crystalline features of low spectral contrast, when fitted by the thermal models, contribute significantly to the crystal mass fraction (f_{cryst}) because (a) Mg-crystals are cooler and therefore more mass is required to account for their observed flux and (b) crystals are solid whereas the amorphous materials are considered to range from solid to porous and porous particles produce greater flux per mass (greater surface area and higher temperatures). The assessment of the crystal mass fractions may be one of the important contributions of JWST MIRI IFU to quantifying the comae dust properties and impacting our understanding of cometary materials and their origins. In Figure 10 we present all of the comets in our analysis, constrained to a 95% confidence level. This includes comets for which $f_{\text{cryst}} = 0$. There is no clear separation between comet families.

Generally, there is an increase in the relative mass of crystalline silicates when only modeling the SL modules, resulting in a higher f_{cryst} on average by a factor of about 60%. This is illustrated in Figure 11 which shows on the left the mass fraction for mean properties derived from SLLL models of 22 comet spectra in the Spitzer survey for the 5 min-

eral components in the thermal model designated in the figure as: amorphous carbon (AC), amorphous pyroxene (AP50 for Mg:Fe=50:50), amorphous olivine (AO50), crystalline olivine (CO) and crystalline pyroxene (CP) (see Section 3.1). The right is the mass fraction of the entirety of the sample (combined SLLL–SL and SL). For the population of models of SLLL versus SLLL–SL (for the same 22 comet spectra), the increase in crystalline pyroxene is what drives the increase in f_{cryst} .

4.8. Amorphous carbon

For the distribution of SLLL models, the full range of amorphous carbon is large, spanning 0.1–0.9, with the distribution of models having a mean and standard deviation of 0.54 ± 0.16 , and 16 of 22 models or 73% lie within the 1σ range of the mean as expected for a gaussian distribution.

Woodward et al. (2021) discuss the the importance of amorphous carbon as a significant component of coma refractories derived from thermal modeling and the association of these result with cometary materials observed *in situ* measurements (Rosetta on 67P/Churyumov-Gersimenko, Vega 1 and Vega 2 on 1P/Halley) and laboratory investigations on cometary samples and cometary IDPs. Carbon X-ray Absorption Near Edge Spectroscopy (C-XANES) has identified carbon in the phase of amorphous carbon in some cometary samples (Wirick et al. 2009) but many cometary samples have other forms of carbon including aromatic and aliphatic carbon bonds and rarely graphite (Matrajt et al. 2005; De Gregorio et al. 2017; Engrand et al. 2023). Optical constants for solid state organics with suitably highly absorbing properties, similar to amorphous carbon, are lacking and the available optical constants for organic solid state residues such as tholin (Brassé et al. 2015) are significantly too transparent to account for the observed near-infrared cometary flux densities and high particle temperatures of the carbonaceous dust component in cometary comae that is well modeled by amorphous carbon (Bockelée-Morvan et al. 2017b,a; Engrand et al. 2023).

Cometary IDPs are visibly very dark but when sliced or when crushed these same particles become more transparent (Flynn et al. 2000) so the optical properties of cometary IDPs may not be identical throughout the particle. Thermal models presume that the optical properties are the same throughout each particle and use of mixing theories to compute the absorptivities and emission spectra of porous amorphous particles. In support of these modeling methods, computations of porous aggregates with amorphous silicate and amorphous carbon monomers distributed though out the particle and with amorphous carbon as a fluffy mantle do not yield significantly different predicted optical properties (e.g., Figure 8 in Silsbee & Draine 2016). The interstitial porous

material that appears to hold together the crystalline silicates and amorphous silicates in cometary IDPs has long been described as the carbonaceous matrix or glue that holds the particles together (Thomas et al. 1993a; Brunetto et al. 2011; Dobrică et al. 2012). In Stardust return samples and in IDPs, carbonaceous matter appears as aromatic-rich nanoglobules (Nakamura-Messenger et al. 2006; Busemann et al. 2009; de Gregorio et al. 2011). The carbonaceous matter is where D-enrichments reside (Busemann et al. 2009; Enggrand et al. 2023) as well as rarely revealing higher N/C ratios (Fray et al. 2017), giving clues to some of its origin in cold molecular cloud environments via ion-molecule reactions that enhance D (Ishii et al. 2018).

Bulk X-ray measurements of carbon in eleven anhydrous IDPs were assessed in the 1990s and shown to be 5–25 wt% of elemental carbon with pyroxene-dominated crystalline silicates having the higher wt% carbon (Figure 3; Thomas et al. 1993b). By comparison with bulk S/Si and Fe/Si, the higher carbon, higher crystalline IDPs were suggested to be the best candidates for cometary IDPs collected in the stratosphere. From these bulk IDPs studies, the highest reported bulk C of ~ 45 wt% was reported for the pyroxene-rich IDP L2006B23, which also was characterized by $\sim 50\%$ porosity that yielded an estimated 90 vol% for its carbonaceous matter (Keller et al. 1994).

In comparison to these prior studies, Rosetta’s COSIMA *in situ* mass spectrometry of 30 particles from comet 67P/Churyumov-Gersimenko, which are representative of >250 particles, demonstrated that carbonaceous matter comprises 45wt% of the dust (Bardyn et al. 2017). From thermal models, comet 67P/Churyumov-Gersimenko (4 models) has an amorphous carbon (where amorphous carbon has optical constants that are taken as proxy for the carbonaceous matter that was measured by COSIMA) mass fraction of 0.46 ± 0.13 . Woodward et al. (2021) showed that comet C/2013 US10 (Catalina) has a mass fraction of $0.473^{+0.015}_{-0.017}$ for amorphous carbon, similar to 67P/Churyumov-Gersimenko’s *in situ* determination.

This Spitzer survey finds that the comet model population has a mass fraction of 0.54 ± 0.16 of dark and highly absorbing carbonaceous matter that is well modeled by amorphous carbon. The emerging paradigm is that most comets have a carbonaceous content of ~ 50 wt%. Furthermore, comets present an important metric of 50 wt% carbon in the solid state dust that is key to our understanding of the reservoir of the protoplanetary disk out of which comets formed and how it differed from the reservoir out of which asteroids like Ryugu (Nakamura et al. 2023) and other carbonaceous chondrites were derived (possibly by collisions with large bodies).

The fits to the mid-infrared preferentially select amorphous pyroxene over amorphous olivine. We attribute this preferential selection of amorphous pyroxene in the mid-infrared to the prevalence of a short wavelength shoulder on the 10 μm feature of comets in this Spitzer survey. However, this shoulder is not ubiquitous amongst cometary 8–13 μm spectra. Hanner et al. (1994, Table 2 and Figure 5) called attention to the mid-infrared spectrum of Oort comet C/1990 K1 (Levy) (prior designation 1990 XX, Shanklin 1995) because of its a narrower 10 μm feature with short wavelength rise at longer wavelengths. This was attributed to amorphous olivine by comparison with laboratory absorption spectra of laser-vaporized (amorphous) forsterite. Thermal modeling of 10 μm emission features using optical constants of Mg:Fe amorphous olivine (‘bronzite’) and amorphous pyroxene provided by Dorschner et al. (1995) demonstrated the need for Fe in the amorphous silicates in order to derive the required radiative equilibrium temperatures to predict and fit the spectral contrast and shape of the features (Hanner et al. 1996; Harker et al. 2002).

There is some concurrence that amorphous silicates in the ISM are Mg-rich (Min et al. 2008; Hensley & Draine 2021). However, factors of composition, shape, porosity affect 10 μm band shape (Henning 2010) and the 10 μm to 20 μm band ratio for lines-of-sight through the ISM. Determining the composition of ISM amorphous silicates is thereby challenging. In contrast, the composition of the amorphous silicates in comets is known because, given that comet comae particles are emitting in radiative equilibrium at a given distance from the sun, then the size distribution, porosity and composition of amorphous silicates can be constrained by comet thermal models. Although heritage of ISM materials into the outer protoplanetary disk is often discussed, the uncertainties in the composition of the ISM amorphous silicates then makes it difficult to presume a heritage (link) between cometary amorphous silicates and ISM amorphous silicates.

GEMS (glasses embedded in metals and sulfides) are amorphous silicates that are found in most cometary IDPs and in Ultra-Carbonaceous Antarctic Micro Meteorites (UCAMMs). GEMS are porous and have $(\text{Mg}+\text{Fe})/\text{Si} \leq 1$ (Bradley et al. 2022) and therefore are not stoichiometric. In contrast, thermal models for comets employ optical constants of stoichiometric amorphous pyroxene and olivine so one cannot compare the cometary model $(\text{Mg}+\text{Fe})/\text{Si}$ ratio to that of GEMS because of the constraints of the materials in the models. There only are a few infrared spectra of GEMS-rich regions of IDPs (Bradley 1994; Ishii et al. 2018). Therefore, there are insufficient spectra of GEMS for a robust comparison between cometary comae infrared spectra and GEMS. All cometary infrared spectra have amorphous silicate emission features and studies of cometary IDPs ubiq-

4.9. Amorphous silicates

uitously discuss GEMS. This fact does not justify nor deny a potential link between the GEMS and cometary spectral thermal models.

Amorphous pyroxene to amorphous silicates ratios in the diffuse ISM and towards protostars are based on 10 μm features only and our analyses of SLLL versus SLLL–SL indicates that the composition deduced from the 10 μm region alone may be biased towards pyroxene identifications. Thus, determining the origin and heritage of silicates in comets is challenging. The derived amorphous olivine to amorphous pyroxene compositional ratios in comets may provide clues.

4.9.1. Silicate irradiation and amorphization

The “short wavelength shoulder” on the mid-infrared 10 μm feature fitted by the amorphous pyroxene component in the model is a potential signature of amorphization by ion irradiation (cosmic rays). For irradiated amorphous Mg:Fe olivine measured in the laboratory only relative wavelengths shifts of the shoulder (Jäger et al. 2016) are reported and no optical constants are provided. Hence, assessing the amount irradiation that the amorphous silicates present in the refractory component of comet comae dust experienced is beyond the scope of this work.

Do-Duy et al. (2020) model the 10 μm feature along line-of-sight through the galactic diffuse ISM and quote the ratio of amorphous pyroxene to amorphous silicates is 17% towards the Galactic Center. In the circumstellar environments of O-rich Asymptotic Giant Branch (AGB) stars, where olivine condenses prior to pyroxene, the amorphous pyroxene to amorphous silicate ratio is low. Amorphous olivine dominates the line-of-sight towards η Ceph (Sargent et al. 2006). On the other hand, amorphous olivine and amorphous pyroxene are seen towards molecular clouds (van Breemen et al. 2011) and embedded protostars (Do-Duy et al. 2020). Irradiation by cosmic rays has been long postulated as the cause of the trend between amorphous olivine-dominated AGB circumstellar medium versus the diffuse interstellar medium and protoplanetary disks with higher amorphous pyroxene to amorphous silicate ratios. Only one laboratory experiment provides spectral measurements of both the 10 μm and 18 μm silicate features before and after irradiation of amorphous olivine. Jäger et al. (2016) shows a diminishment in the 18 μm /10 μm feature ratio after H^+ irradiation, as well as shifts to longer wavelengths due to strong interactions with the experimental substrate that they do not consider relevant.

Recent JWST MIRI spectra of Class 0 protostar provides exquisite S/N spectra and modeling of these SEDs, specifically the 10 μm absorption feature, demonstrates the dominance of amorphous pyroxene over amorphous olivine (Kóspál et al. 2023). The JWST modeling uses the same optical constants used in our comet thermal model. The Spitzer survey shows that there is a wide range of ratios of amorphous pyroxene to amorphous silicate for the SLLL mod-

els. However, additional laboratory measurements are clearly required at 10 μm and 18 μm , which is critical to breaking the degeneracy between olivine and pyroxene compositions. Measurement of the far-infrared resonances that are less overlapping than those in the mid-infrared, will enable an analyses of the potential signatures of irradiation of silicates as probed by cometary infrared SEDs and thermal models.

4.9.2. Feature Ratios: 19 μm and 10 μm

The analysis of the Spitzer comet set may provide some clues by careful assessment and comparison of the observed and model amorphous silicate feature 19 μm -to-10 μm ratios and the wavelengths of the rise of the 10 μm silicate feature. These data and the set of thermal models for this survey, which is uniquely suited because of its uniformity of data reduction and modeling methods, reveals an intriguing correlation (albeit at the 95% confidence level) between the observed and model 19 μm -to-10 μm feature ratios. The observed ratios may have a lower value than the model as well as the observed wavelength of the rise of the 10 μm feature occurs at shorter wavelengths than the model.

These differences between the data and the model are subtle: the optical constants of the amorphous Mg:Fe olivine and amorphous Mg:Fe pyroxene well represent the spectral shapes of the SLLL data (see 73P(B)-20060806.18 for amorphous pyroxene, 48P/Johnson for amorphous olivine, and 46P-20080424 for a combination of amorphous pyroxene and amorphous olivine). Also, these same optical constants are used to model amorphous silicates in many astrophysical environs (Henning 2010; Do-Duy et al. 2020; McClure et al. 2023). Optical constants for amorphous silicates made by the sol-gel method are available for compositions similar to Mg-rich pyroxene, Mg-rich olivine, and Mg-,Fe-pyroxene (Jäger et al. 2003; Demyk et al. 2022) but thermal models require amorphous Mg:Fe olivines and amorphous Mg:Fe pyroxenes.

For the populations of models SLLL versus SLLL–SL, systematically, the crystalline fraction assessed from only the mid-infrared compared to the full wavelength data is higher and the wavelength of onset of the 10 μm feature is better fitted by amorphous Mg:Fe pyroxene, which has an onset at shorter wavelengths compared to the amorphous Mg:Fe olivine feature (Mennella et al. 2020). The far-infrared crystalline features of Mg-olivine and Mg-pyroxene, which are weak in comparison to the broad far-infrared amorphous silicate features, appear in some thermal model fits to not be allowed to be ‘squeezed’ into the observed far-infrared flux level, simultaneous with the thermal model fit having a notable dearth of emission in the mid-infrared, Figure 12(a).

Aspects of the observed cometary amorphous silicate emissions may not be well-accommodated by the model and/or alternatively proffer intriguing support of a commonly

held view that in the ISM, the amorphous silicates trend from olivine to pyroxene compositions due to ion bombardment (Demyk et al. 2001; Tsuchikawa et al. 2022). Further, the laboratory experiments exploring H^+ irradiation of amorphous Mg:Fe olivine showed the 19 μm -to-10 μm feature ratio is diminished compared to the un-irradiated samples by about a factor of 0.6 (Jäger et al. 2016). Comet 8P/Tuttle is excluded from this exercise because its silicate-to-carbon ratio is 0.1 and for the purpose of the exercise its silicate feature is too weak.

Let us define $\zeta \equiv (F_\lambda - F(ac))/F(ac)$ with F_λ being observed or model flux density and $F(ac)$ being the model flux density of amorphous carbon; i.e., using the prior notation ζ is the silicate residual flux divided by the amorphous carbon (AC) flux. We characterize the 10 μm and 19 μm silicate features by assessing, $\zeta(10)_{\text{observed}}$, $\zeta(19)_{\text{observed}}$, $\zeta(10)_{\text{model}}$, $\zeta(19)_{\text{model}}$, respectively, from the mean data (with uncertainties) and mean model centered at 10.3 μm spanning the peak of the 10 μm feature and at 19.0 μm in the range where there are contributions from amorphous pyroxene, amorphous olivine, the 19.5 μm crystalline olivine and the 19–20 μm crystalline pyroxene features. A feature sampling bandwidth of $\Delta\lambda = 2 \mu\text{m}$ is used.

We assess the wavelength of the rise of the 10 μm feature at the half maximum of the feature $\lambda_{HM\ 10\mu\text{m}\ \text{rise}\ \text{observed}}$ by a linear regression to point pairs (λ, ζ) such that $7.8\mu\text{m} \leq \lambda \leq 9.3\mu\text{m}$ and $0.25\zeta(10)_{\text{observed}} \leq \zeta \leq 0.75\zeta(10)_{\text{observed}}$. Thereafter, we can define $\lambda_{HM\ 10\mu\text{m}\ \text{rise}\ \text{observed}}$ by the wavelength at which the line fit has value $\zeta(10)_{\text{observed}}/2$. For the model, the wavelength of the rise of the 10 μm feature ($\lambda_{HM\ 10\mu\text{m}\ \text{rise}\ \text{model}}$) is similarly defined. $[\zeta(10)_{\text{model}}/\zeta(19)_{\text{model}}]$ is not correlated with heliocentric distance (r_h (au)) and grain size distribution slope N because dividing the silicate residual flux by the flux of amorphous carbon model is effectively normalizing by a flux that appropriately represents the grain size distribution-weighted particle fluxes with their r_h - and size-dependent radiative equilibrium temperatures. There is no apparent correlation with the shift of the wavelength of the rise of the 10 μm feature with respect to the model.

The model feature ratio $[\zeta(10)_{\text{model}}/\zeta(19)_{\text{model}}]$ is correlated with a_p , Figure 12(b), – orange line. In contrast, $[\zeta(10)_{\text{observed}}/\zeta(19)_{\text{observed}}]/[\zeta(10)_{\text{model}}/\zeta(19)_{\text{model}}]$, is independent of a_p , Figure 12(b), – blue line, because to first order the model fits the observed 19 μm -to-10 μm feature ratio. The $[\zeta(10)_{\text{observed}}/\zeta(19)_{\text{observed}}]/[\zeta(10)_{\text{model}}/\zeta(19)_{\text{model}}]$ is independent of $f(\text{ap}50)/AS$, that is, it is not correlated with the amorphous silicate compositions. In this exercise, we are pursuing the subtle differences between the observed and model amorphous silicate features by utilizing ζ .

With these parameters established, Figure 12(c) shows that there is a relationship between $[\zeta(10)_{\text{observed}}/\zeta(19)_{\text{observed}}]/[\zeta(10)_{\text{model}}/\zeta(19)_{\text{model}}]$ and $\lambda_{HM\ 10\mu\text{m}\ \text{rise}\ \text{observed}}$, given by the linear regression (Seabold & Perktold 2010). We interpret the trend-line in Figure 12(c) to mean that when the observed 19 μm -to-10 μm ratio is smaller than the model 19 μm -to-10 μm ratio, the short-wavelength-rise of the 10 μm feature will also occur at shorter wavelengths.

There are sparse laboratory IR spectroscopic studies that measure the changes in the mid-infrared and far-infrared spectral features from ion irradiation of Mg:Fe silicates and in particular of Mg:Fe amorphous silicates. Jäger et al. (2016) shows that the 19 μm -to-10 μm ratio is lowered by a factor of about 0.6 by H^+ irradiation of amorphous Mg:Fe olivine. The decrease in the strength of the bending mode (far-infrared) relative the Si–O stretching mode (mid-infrared) is a consequence of the restructuring of the amorphous silicate matrix due to the destruction of bridging oxygen atoms. Nano-phase Fe also forms. In this experiment, the wavelength of the peak of the 10 μm feature shifts to longer wavelengths by 0.46 μm but the far-infrared absorption feature is only slightly shifted. This can be explained via a reduction of bridging oxygen by sputtering since “...10 μm band of silicates is usually a measure of the polymerization of SiO_4 tetrahedrons in the amorphous network...” (Jäger et al. 2016). Their ion irradiation of the amorphous Mg olivine resulted in nanometer-sized silicon particles and less modification to the surrounding silicate matrix as well as significantly less formation of nano-phase Fe. However, no IR spectra are shown.

For the population of SLLL models in this Spitzer survey, the minimum of $[\zeta(19)/\zeta(10)_{\text{observed}}]/[\zeta(19)/\zeta(10)_{\text{model}}]$ is about 0.6, which may be accompanied by a systematic shift towards shorter wavelengths (Figure 12(c)). The decline in the 19 μm -to-10 μm feature presented here is in agreement with the experiment but not the wavelength shift of the rise of the 10 μm feature that may be attributable to particle-irradiative processing of amorphous silicates prior to their incorporation into comets compared to the laboratory-prepared glasses from which the employed optical constants are derived. In this context, studies indicate loss of Mg and O with ion irradiation and discuss trends towards pyroxene compositions upon irradiation (Carrez et al. 2002a; Demyk et al. 2001; Carrez et al. 2001).

Various laboratory irradiation experiments (Carrez et al. 2002b; Jäger et al. 2003; Demyk et al. 2004; Brucato et al. 2004; Szenes et al. 2010; Christoffersen & Keller 2011; Rietmeijer 2009; Jäger et al. 2016) have interesting implications for ISM silicate evolution and studies of cometary refractories. The origins the amorphous silicates in cometary

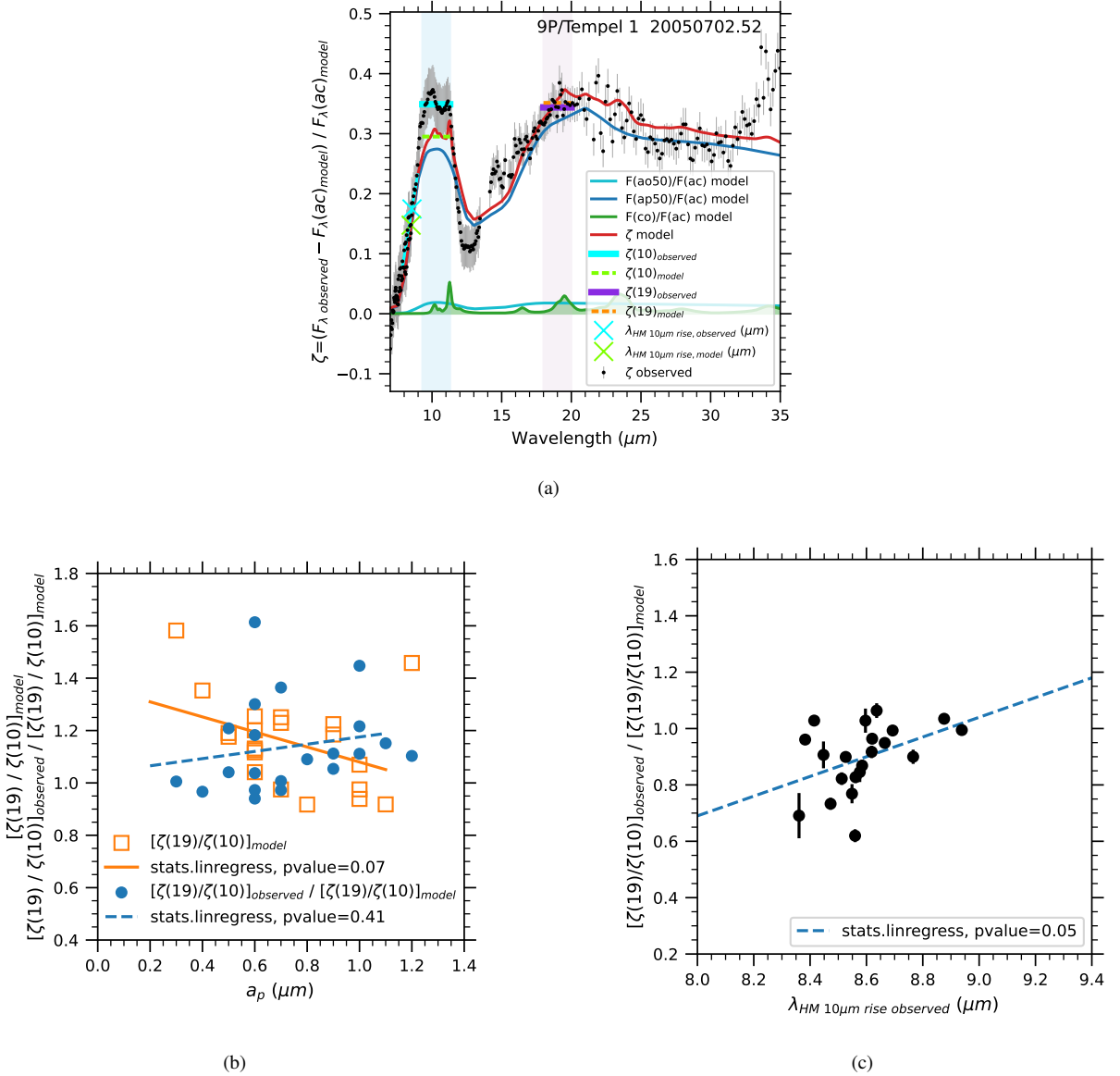


Figure 12. Analyses of the silicate feature ratios of 10 μm -to-19 μm . (a) ζ versus λ 9P/Tempel 1 (20050702.52). For 9P/Tempel 1, we define $\zeta_{\text{model}} = (F_{\lambda, \text{total}} - F(ac))/F(ac)$ and $\zeta_{\text{observed}} = (F_{\lambda, \text{observed}} - F(ac))/F(ac)$. $\zeta(10)$ is the flux averaged over $\Delta\lambda = 2 \mu\text{m}$ centered at $10.3\mu\text{m}$, and $\zeta(19)$ uses $\Delta\lambda = 2 \mu\text{m}$ centered at $19.02 \mu\text{m}$. (b) Silicate feature ratios of 19 μm -to-10 μm versus a_p . The models' silicate feature ratio 19 μm -to-10 μm ($[\zeta(19)/\zeta(10)]_{\text{model}}$) is dependent upon the grain size distribution peak grain size a_p . However, $[\zeta(19)/\zeta(10)]_{\text{observed}} / [\zeta(19)/\zeta(10)]_{\text{model}}$ is independent of a_p . (c) $[\zeta(19)/\zeta(10)]_{\text{observed}} / [\zeta(19)/\zeta(10)]_{\text{model}}$ versus $\lambda_{HM} 10\mu\text{m rise observed}$. A linear regression using the python statsmodels linregress (Seabold & Perktold 2010) yields a slope of 0.350 ± 0.170 and intercept of -2.109 ± 1.462 , and pvalue of 0.05. A firm correlation requires a pvalue of ≤ 0.007 (97.3% probability of the failure of the null hypothesis of a zero-valued slope) so the pvalue of 5% indicates there is only 95% confidence that this non-zero-valued slope represents a correlation.

Table 7. C/Si Ratio

Comet	C/Si
6P/d' Arrest	4.255 ± 1.384
8P/Tuttle	86.146 ± 13.179
9P/Tempel 1	4.716 ± 1.715
17P/Holmes	0.672 ± 0.133
21P/Giacobini-Zinner	6.353 ± 1.904
29P/Schwassmann-Wachmann 1	1.791 ± 0.464
37P/Forbes	3.835 ± 1.017
41P/Tuttle-Giacobini-Kresak	20.276 ± 3.961
46P/Wirtanen	10.075 ± 7.152
48P/Johnson	2.558 ± 0.606
62P/Tsuchinshan 1	3.515 ± 1.599
65P/Gunn	3.214 ± 1.002
67P/Churyumov-Gerasimenko	9.087 ± 5.426
71P/Clark	6.757 ± 1.953
73P/Schwassmann-Wachmann 3 [B]	4.552 ± 1.716
73P/Schwassmann-Wachmann 3 [C]	2.318 ± 0.509
78P/Gehrels 2	2.703 ± 0.642
88P/Howell	4.222 ± 1.120
105P/Singer Brewster	5.059 ± 1.850
121P/Shoemaker-Holt 2	1.025 ± 0.473
144P/Kushida	7.194 ± 1.999
C/2001 Q4 (NEAT)	1.475 ± 0.347
C/2003 K4 (LINEAR)	6.264 ± 2.230
C/2003 T3 (Tabur)	1.250 ± 0.360
C/2003 T4 (LINEAR)	1.086 ± 0.428
C/2004 B1 (LINEAR)	6.391 ± 4.178
C/2004 Q2 Machholz	2.709 ± 0.593
C/2006 P1 (McNaught)	3.972 ± 1.955
C/2006 Q1 (McNaught)	4.471 ± 2.260
C/2007 N3 (Lulin)	8.826 ± 2.896
C/2008 T2 (Cardinal)	10.936 ± 3.470

samples, the GEMS, is highly debated between potential solar system, cold cloud, and ISM origins (Bradley & Ishii 2008; Min et al. 2008; Keller & Messenger 2011, 2013; Bradley et al. 2022). Regardless of whether the source of ion irradiation is local or ISM, this Spitzer comet survey is a unique set of data that suggests the complexity of cometary materials as probed by thermal modeling of IR SEDs may be able to be enhanced by additional laboratory IR spectroscopic studies of ion bombardment of amorphous Mg:Fe silicates to assess the shifts in wavelengths of the rise of the

10 μm spectral features and the 19 μm -to-10 μm feature ratios.

4.10. Carbon/Silicon elemental ratios

The atomic C/Si ratio for each of our spectra is based on the relative mass fraction of submicron grains for each material used in the best-fit thermal model (Section 3; Table 3). The method for calculating the atomic C/Si ratio is based on the methodology presented in Woodward et al. (2021). They make some suppositions related to their calculation of atomic C/Si ratio. One, is that the amorphous carbon used in the thermal dust model is considered to be a good representation of the highly absorbing carbonaceous based material in comet comae. And two, that the relative mass fraction of carbon calculated from the model fits is a good representation of the bulk of the solid state carbon (not the carbon in the gases of ices) material within the comet comae. When comparing our results with *in situ* and laboratory studies, we are comparing our spectroscopic observations of a mix of thermally radiating grains of various radii to studies of single or isolated domains.

As in Woodward et al. (2021), to allow for error propagation in our calculation of C/Si, we “symmetrize” the relative mass fractions in Table 3 using Method #2 of Audi et al. (2017), being aware of the limitations of using this method (Possolo et al. 2019). The C/Si ratio is calculated by assuming the mass fraction in the numerator is 100% carbon, and the denominator is the sum of the mass fractions of the silicate bearing species with a atomic Si mass fraction of 24.2%, 16.3%, 20.0%, and 28.8% for amorphous pyroxene, amorphous olivine, crystalline olivine, and orthopyroxene, respectively. Table 7 lists the values of C/Si for each spectrum in our sample.

The C/Si elemental ratio derived for comets (Table 7) in the Spitzer survey are near the ISM values and higher than those of carbonaceous chondrites. In the Spitzer survey, comets with higher amorphous carbon relative mass fractions are more numerous than comets with lower amorphous carbon, Figure 11 (left). That is, comets with AC \lesssim 40%, like 17P/Holmes in outburst and Hale-Bopp, appear to be uncommon. Comet 67P, which can be seen in the ternary diagram to have thermal model parameter (mass fraction) AC \gtrsim 50%, was assessed by Rosetta COSMIA mass spectrometry to be 45 wt% organics. Thermal models derive a similar C/Si ratio from the mass fraction of amorphous carbon (Woodward et al. 2021). The C/Si elemental ratios that are near the ISM value suggest comets either efficiently sequestered carbonaceous materials from the ISM or the outer disk produced refractory organics as recorded by comets. The high C/Si in comets is not seen in the carbonaceous chondrites, which are considered to be the most carbon-rich of the asteroid populations.

To look for any trends or differences between comet families, Figure 13 shows the atomic C/Si ratio versus f_{cryst} for all of the spectra in our sample. This includes comets for which $f_{cryst} = 0$. In Figure 13(a), we present all of the spectra in our analysis, and in Figure 13(b), we present those spectra for which f_{cryst} has been constrained to a 95% confidence level. In neither plot is there a clear separation between comet families.

4.11. Comets spectra of special interest

4.11.1. 17P/Holmes

The spectrum of comet 17P was obtained less than about 20 days after a mega-outburst, and soon after a possible mini-outburst (Reach et al. 2010). During the Spitzer observations 17P was centered in each of the modules using the peak-up array. Subsequent background observations were taken off-set from the comet center. Details of the observations are presented in Kelley et al. (2021).

The resulting spectrum of 17P exhibits a large silicate feature in the $10\ \mu\text{m}$ region as well as smaller, but distinctive crystalline silicate peaks at longer wavelengths. The initial attempt to model the spectrum of 17P did not produce a particularly good fit to the spectrum. The $10\ \mu\text{m}$ silicate feature was fit poorly as well as the continuum less than about $7.8\ \mu\text{m}$. However, the fit revealed what is possibly an absorption feature between $6.2\ \mu\text{m}$ and $7.8\ \mu\text{m}$. Careful examination of the observing sequence shows that the sky background was measured in a diffuse region of the coma prior to the primary science coma-centered observation. In the non-background subtracted image cubes, there appears excess emission in this offset coma position but only at these wavelengths and not at $\gtrsim 8\ \mu\text{m}$. We speculate that a potential source of emission at these extended coma distances could be from PAHs but the S/N ratio is poor as well as the spectral resolution insufficient to model and subtract any cometary water vapor emission. Alternatively, the outburst may have released grains of unknown composition that is generating an absorption feature.

In summary, the ambiguity of the identification of the ‘dust continuum’ shortward of $7.5\ \mu\text{m}$ led us to model the SED longward of $7.5\ \mu\text{m}$, which results in the appearance of an absorption feature in Figure 7. Future observations of comets with JWST in this wavelength regime will provide SEDs with superior spectral resolution and sensitivity to explore whether such absorption features are extant.

As for possible absorption sources in the coma, since the comet was observed after a major outburst on 2007 October 23 UT (Reach et al. 2010), less than a month before it was observed by Spitzer. This outburst could have released grains of some unknown composition that lingered in the coma for an extended period of time. JWST has superior sensitive and spectral resolution in the $6.2\text{--}7.8\ \mu\text{m}$ region, enabling

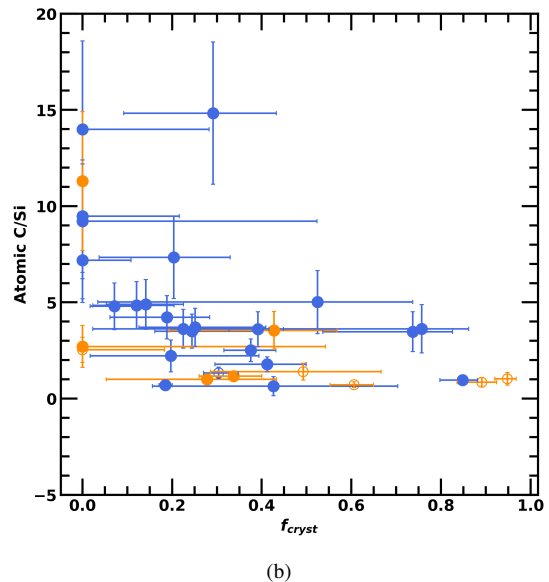
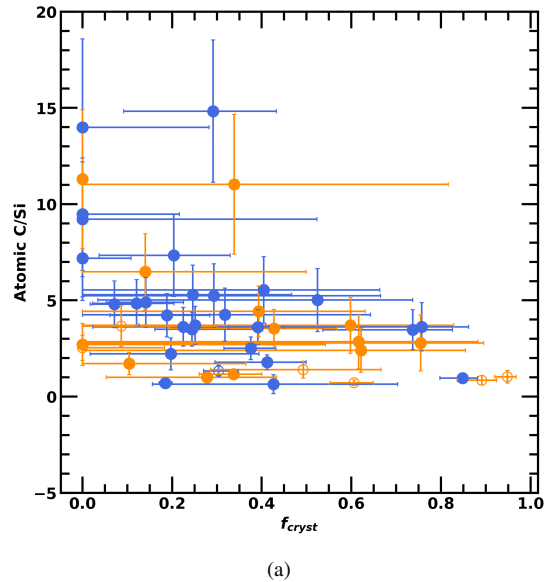


Figure 13. Atomic carbon-to-silicate ratio versus f_{cryst} for the comet spectra in our sample. JFC (short period) comets are shown in blue, and OC (long period) comets in orange. (a) All comet spectra in the survey. (b) Comet spectra where f_{cryst} is constrained to the 95% confidence level.

not only detect of water lines (Woodward et al. 2023), but when subtracted from the spectrum, residuals that may show potential spectral feature of grains of unknown composition that might be contributing to emission or absorption features in comets. Accounting for, and modeling the nature of, this possible absorption feature is outside the scope of this paper. We are primarily concerned with the refractory materials in the coma, so for our purposes, we modeled our SEDs long-

ward of $7.5 \mu\text{m}$ and will explore the origins of this absorption in future analyses.

4.11.2. 73P/SW

Comet 73P(C)-20060806.05 also has a unique model fit. The grains were very fractally porous with $D = 2.607$ and with a large peak to the HGSD of $a_p = 2.3 \mu\text{m}$. The resulting $f_{cryst} = 99.4\%$, which is extremely large and we think is not a robust determination. There is nothing strange with the observation or the spectral extraction. It is possible for the comet to have changed its grain properties post-perihelion, but and if so, then it is likely the model is challenged to adequately represent the properties of large, possible crystalline grains. To match the rounded feature shape strength, the amorphous grains had to be fairly porous with a relative large peak to the grain size distribution. Given that we model crystalline grains as solids, to match the feature shape contrast, a significantly more crystalline material have to be compacted into an equivalent grain of radius of a , resulting in such a large f_{cryst} . Hence, based the shape of spectral feature observed in the SED, the model approach is not applicable and results in a non-physical outlier.

4.12. Implications for protoplanetary disk processes

Cometary dust compositions probe the conditions in the protoplanetary disk in the realms of icy small body accumulation because the temperatures experienced by refractory dust particles in cometary nuclei are too low to change their composition and structure and there is no significant evidence of aqueous alteration of minerals in the Stardust return samples from comet 81P/Wild 2. Cometary dust particles are probed by laboratory examinations of chondritic anhydrous IDPs (CA IDPs, [Engrand et al. 2023](#)), which vary in porosity, organic matter content and composition, and the Mg:Fe-content of their crystalline silicates.

Stardust return samples and giant IDPs contain crystalline olivine with a wide range of Mg:Fe-contents from Mg:Fe=100:0–0:100. Studies of their minor element abundances confirm their compositional links to Type II (Fe-rich) micro-chondrules ([Ogliore et al. 2009](#); [Frank et al. 2014b](#); [Wooden et al. 2017](#); [Brownlee & Joswiak 2017](#)), with one age-dated at ≥ 3 My after CAI formation ([Ogliore et al. 2012](#)). Oxygen isotope studies of crystalline olivine in Stardust return samples and CA IDPs shows that the highest Mg-content crystalline olivines (Mg:Fe=100:0–80:20) are ^{16}O -rich with $\Delta^{17}\text{O} \approx -23$ ([Defouilloy et al. 2016, 2017](#)). This finding suggests the formation (condensation) of Mg-rich crystalline olivine occurs in early ^{16}O -rich reservoir in the protoplanetary disk. Minor element studies also reveal Low-Iron-Manganese Enriched (LIME) olivine crystals in Stardust return samples (Mg:Fe=100:0–90:10), which characterize them as condensates ([Klöck & Stadermann 1994](#); [Joswiak et al. 2017](#)). Thermal models presented here of 42 Spitzer IR

SEDs successfully fit crystalline olivine with Mg:Fe=100:0–80:20 and do not find features from higher Fe-contents crystalline olivine ([Koike et al. 2003](#)). By comparison to these laboratory studies, the crystalline olivine fitted in thermal models in these 42 comets are early-forming condensates and not later-forming micro-chondrules.

Disk models for radial transport via diffusion have achieved f_{cryst} of 10%–20% ([Bockelée-Morvan et al. 2002](#); [Keller et al. 2004](#); [Dullemond et al. 2006](#); [Ciesla 2010](#)). Disk models with annealing during infall, crystal condensation in the inner disk, and radial transport can produce f_{cryst} of 40% but the refractory materials that formed after infall are abundant in the 2–5 au region ([Yang & Ciesla 2012](#)), which is interior to the comet-forming zone. Magnetically driven disk wind transport may produce f_{cryst} of 1 out to 20 au ([Arakawa et al. 2021](#)). Disk models may consider annealing of amorphous silicates as a mechanism to explain enhanced f_{cryst} because annealing happens at lower temperatures and thus over larger disk volumes. However, the amorphous silicates in cometary thermal models must have Mg:Fe \approx 50:50 to explain their radiative equilibrium temperatures ([Harker et al. 2002](#)). Highly specialized circumstances such as annealing of only micron-sized and smaller Fe-bearing glasses under low oxygen fugacity conditions that allows for inter-diffusion and loss of Fe metal could explain Mg-rich cometary crystals ([Wooden et al. 2007](#)). The crystal mass fraction for the population of models f_{cryst} is 35–39% and ubiquitously the crystals are Mg-rich so this study implies there was significant and efficient radial transport of Mg-rich crystals, which likely are condensates, from the hot inner disk out to the comet-forming regime.

Mg:Fe amorphous silicates are modeled in all cometary IR spectra. Based on laboratory studies of cometary CA IDPs, the amorphous silicates in cometary samples are the so-called GEMS, with FeS inclusions, non-stoichiometric compositions, substantial porosities, as well as some evidence for ion irradiation. The subtle spectral behaviors of the amorphous silicate 18 μm -to-10 μm ratios in 21 SLLL models (Section 4.9.2) together with the wavelength of the rise of the 10 μm feature suggests the Mg:Fe amorphous silicates may have experienced differing degrees of ion irradiation. Optical constants of irradiated amorphous Mg:Fe silicates are a future necessity.

The crystalline pyroxene to crystalline olivine ratios ($f(\text{cp})/f(\text{co})$) assessed from thermal models for individual comets have a large range of values, spanning 0 to ∞ . The mean and standard deviation of the ratios of $f(\text{cp})$ to $f(\text{co})$ per comet model that are not at these two extremes is approximately equal to the ratio and propagated uncertainties of the model population Mean and Std of $f(\text{cp})$ to $f(\text{co})$ (Table 5). These values are for $f(\text{cp})/f(\text{co})$: 1.9 ± 2.6 (SL), 1.2 ± 2.6 (SLLL), 2.5 ± 2.6 (SLL–SL), 2.2 ± 2.7 (SLLL–SL &

SL), which are greater than 1. Crystalline Mg-pyroxene has a greater mass fraction in models fitted only to the short wavelength mid-infrared data (SLLL–SL and SL models). Comparison of model-derived crystalline pyroxene-to-crystalline olivine ratios to those assessed for carbonaceous chondrites (< 1), UCAMMs (> 1), and for Stardust return samples (~ 1) (Dobrică et al. 2012) are affected by the bias towards higher ratio values for comet spectra models fitted only to the mid-infrared data. Dobrică et al. (2012) discuss the evidence of higher crystalline pyroxene to crystalline olivine ratios with increased disk radii from observations and from UCAMM studies. They suggest high pyroxene/olivine ratios may trace small body accretion at the greater disk radii. The population of comet models presented here and UCAMMs share similarly high values of crystalline pyroxene-to-crystalline olivine ratios.

The cometary amorphous carbon mass fraction (Sections 4.8, 4.10) is high compared to carbonaceous chondrites, which supports the concept of a carbon gradient in the solar system as well as offering support to the growing evidence of the effects of a gap in the disk created by Jupiter formation (Woodward et al. 2021). In UCAMMs, which are compared to CA IDPs yet may be particles from a N-rich parent body, crystalline Mg-pyroxene is correlated with higher wt% of carbonaceous matter (Dobrică et al. 2012). In this study, crystalline Mg-olivine is anti-correlated with amorphous carbon, which is similar to bulk studies of limited numbers of CA IDPs (Thomas et al. 1994). Without this anti-correlation between Mg-rich crystalline olivine and amorphous carbon in the thermal models, the reservoirs of Mg:Fe amorphous silicates, Mg-crystalline silicates and dark carbonaceous matter might appear to be separate and unrelated reservoirs in the disk. Taking together the anti-correlation of amorphous carbon with crystalline olivine and the model populations’ having crystalline pyroxene-to-crystalline olivine ≥ 1 suggests that amorphous carbon and crystalline pyroxene may have been together more abundant in the outer disk.

Each comet offers a probe of disk conditions. The populations of thermal models of the Spitzer survey reveal a significant range in compositions between individual comets as well as these intriguing trends. The JWST era of comet observations will compliment this extensive data set and offer more information and constraints on protoplanetary disk conditions under which comet nuclei agglomerated.

5. CONCLUSION

Thermal dust models of 57 spectral energy distributions from 5–35 μm covering 33 individual comets (some observed at multiple epochs) obtained from the Spitzer Heritage Archive uniquely allow the assessment of the compositional properties and trends for a significant number of comets from

the application of thermal models to data reduced by consistent methods from the same instrument.

Analyses of the population of thermal model compositions utilize the relative mass fractions (defined as $f(\text{material})$) of the five mineral components: amorphous carbon, amorphous Mg:Fe pyroxene, amorphous Mg:Fe olivine, crystalline Mg olivine, and crystalline Mg pyroxene ($f(\text{ac})$, $f(\text{ap50})$, $f(\text{ao50})$, $f(\text{co})$, $f(\text{cp})$). The population of models for compositional analyses is restricted to $r_h < 3.5$ au and utilizes only data with Spitzer IRS full wavelength coverage (SLLL) or mid-infrared data (SL), which yields 22 SLLL and 20 SL infrared spectral energy distribution (SED) models for model compositional population studies. Detailed comparisons of thermal models fitted to SLLL and to only the mid-infrared data points of the same data sets (SLLL–SL) elucidate aspects of the data and of the model that contribute to wavelength-dependent compositional differences, which is possible for the first time given this large set. Systematically, amorphous pyroxene is fitted to SL compared to SLLL without change in the amorphous silicate mass fraction.

Empirical analysis of the survey comet spectra reveals a range of 10 μm silicate feature shapes, generalized into three broad categories: nearly trapezoidal (indicating emission from amorphous silicates), rounded/triangular with strong emission at 8.2 μm (also indicative of amorphous silicate emission with the possible inclusion of crystalline silicates), and strong narrow features with a stronger 9 μm shoulder (indicative of emission from crystalline silicates).

The rise of the 10 μm feature occurs at shorter wavelengths, better modeled using the optical properties for amorphous Mg:Fe pyroxene. Also, increased crystalline Mg-pyroxene mass fractions are assessed for SL or SLLL–SL with a significant change in the crystalline mass fraction f_{cryst} . The average crystalline fraction of the submicron grain component, f_{cryst} , is 25% for SLLL and $\simeq 35$ –39% for SL-only. Because crystalline silicates are hot nebular products formed in the inner regions of the protoplanetary disk, high values of f_{cryst} demonstrate that efficient radial transport of these materials to the region where comet nuclei aggregated occurred.

The survey comet spectra and models indicate the wavelength of the rise of the 10 μm feature occurs at shorter wavelengths when the observed 18 μm -to-10 μm feature ratio appears weaker than the modeled feature ratio. This difference may result from variable ion irradiation exposure of the cometary amorphous Mg:Fe silicates.

For the populations of models, the crystalline Mg-pyroxene to crystalline Mg-olivine ratio is > 1 , which agrees with laboratory studies of ultra-carbonaceous micro-meteorites (UCAMMs) and is larger than this ratio for carbonaceous chondrites. This outcome suggests that the population of comet models is revealing that the disk distances at

which comets agglomerated are greater for comets than for carbonaceous chondrites.

The crystalline pyroxene to crystalline olivine mass fraction ratios ($f(\text{cp})/f(\text{co})$) assessed from thermal models for individual comets have a large range of values, spanning 0 to ∞ . High pyroxene/olivine ratios may trace small body accretion at the greater disk radii. The population of comet models derived from the Spitzer survey analysis exhibit ratios similar to those measured in laboratory UCAMM samples. Combined with the result that we find an anti-correlation of amorphous carbon with crystalline olivine and the model populations' having crystalline pyroxene-to-crystalline olivine $\gtrsim 1$. These findings suggest that amorphous carbon and crystalline pyroxene may have been more abundant in the outer disk.

The Spitzer comet model population has an average mass fraction of 0.54 ± 0.16 of dark highly absorbing carbonaceous material that is well modeled by amorphous carbon. Jupiter-family comets (JFCs) and Oort cloud comets (OCCs) occupy similar regions of the amorphous carbon–amorphous silicate–crystalline silicate ternary diagram and many comets have a carbonaceous content of order 45 wt% or greater. We find that Jupiter-family and Oort cloud comets occupy similar regions of model parameter space in terms of relative mass fractions. A Kolmogorov–Smirnov (KS) test comparing JFCs and OCCs does not identify any significant difference. Hence, we cannot definitively conclude that there is a distinct difference in the dust composition between OCC and JFC population as a whole. Thus, the development of a robust dust taxonomy scheme based on dynamical family is not yet possible.

The analysis of comet dust characteristics from the Spitzer survey of objects makes it possible to investigate general characteristics of these solar system small body population. These analysis also advance insights into the origin of comets. In the context of the diversity demonstrated by this Spitzer survey, comets exhibit a silicate to carbon ratio and crystalline mass fraction (f_{cryst}) that were more similar (to each other) than diverse. Each observation and model of a given comet is sampling and assessing the dust compositions of cometary materials in the coma.

Remote sensing studies of heliocentric driven activity changes in an individual comet's coma dust characteristics at mid-infrared wavelengths (such as those observable with Spitzer) are few. The limited secular studies primarily are those of in-situ measurements of comet 67P/Churyumov-Gerasimenko by Rosetta, and those of comet C/1996 O1 (Hale-Bopp). The latter, which had had moderate sampling epochs (i.e., heliocentric distance) cross its apparition showed differences in its mid-infrared spectral features and derived refractory composition (e.g., Hayward et al. 2000; Harker et al. 2002; Moreno et al. 2003)

Without the broad IR spectral grasp of Spitzer, Rosetta's VIRTIS-M and VIRTIS-H assessed the comae dust compositions and particle properties by modeling the scattered light color, albedo, and the color temperature of the thermal rise (Rinaldi et al. 2017; Bockelée-Morvan et al. 2019). Rosetta's COSIMA mass spectrometer measured a diversity of dust particle compositions but reporting is limited to dozens of particles (Sansberro et al. 2022). The in-situ Rosetta studies show that within the coma and during the activity cycle of a single comet that there were variations in dust properties. Complimentary to Rosetta's in-situ studies are the dust properties assessed from thermal models fitted to Spitzer IR spectral measurements discussed herein that also show that comae reveal a diversity of dust compositions.

In summary, every individual solar system comet observed offers a probe that reveals insight into conditions extant in our early disk. The findings here will both guide future JWST investigation of comets and provide a link to the JWST study of the nascent evolutionary stages of protoplanetary disk in the infrared. These studies will further advance our understanding of the evolution of planetary disks and the accretion process in the outer solar system.

ACKNOWLEDGMENTS

The coauthors wish to thank the referees for insights and detailed critiques that improved the manuscript and the clarity of the graphical presentations. This work is based in part on observations made with the Spitzer Space Telescope, obtained from the NASA/IPAC Infrared Science Archive (doi: 10.26131/IRSA433), both of which are operated by the Jet Propulsion Laboratory, California Institute of Technology under a contract with the National Aeronautics and Space Administration. Support for this work was, in part, provided by NASA through an award issued by JPL/Caltech. CEW, DEH, and MSPK acknowledge support from NASA grant 80NSSC19K0868. DHW acknowledges support from the STT Branch of NASA Ames Research Center.

Facilities: Spitzer (IRS), IRSA (Spitzer Heritage Archive, doi: 10.26131/IRSA433), NASA Planetary Data System

Software: CUBISM, Astropy (Astropy Collaboration et al. 2018), Numpy (Harris et al. 2020), SciPy (Virtanen et al. 2020), scikit-learn (Pedregosa et al. 2011)

APPENDIX

A. AKAIKE INFORMATION CRITERION (AICC)

The Akaike Information Criterion (AIC) is well-used and can be derived from properties of the statistical distribution (cite derivation reference). The AIC is used to compare two sets of models fitted to data points and allows one to ask: Is the information content of one model fitted to one set of data points greater to or lesser than a second model fitted to a second (and possibly different) set of data points? What is the probability that $model_A$ for data set A is more robust than $model_B$ for data set A?

To define the AIC, a **partition function** is required, which represents the volume of data space that has significant probability:

$$Z_D(\alpha) = (2\pi)^{N/2} \prod_{i=1}^N \sigma_i(\alpha). \quad (A1)$$

To maximize the Likelihood $L(\alpha)$ for a model dependent upon a vector of parameters α or v_{param} , we minimize $-2 \ln L(\alpha)$ (see Eqn. 4.17, Ivezic et al. 2014). The Likelihood $L(\alpha)$ also can be defined as:

$$L \equiv \prod_{i=1}^{N_{data}} \{(2\pi)^{-0.5} \sigma_i^{-1} \exp(-((x_i - model_i)/(\sqrt{2}\sigma_i))^2)\}. \quad (A2)$$

Maximizing the Likelihood is equivalent to minimizing χ^2 for data with Gaussian distributed uncertainties σ (Ivezic et al. 2014). The Likelihood is related to AIC by $-2 \ln L(\alpha) = AIC + 2k$. Expanding,

$$\begin{aligned} AIC &= -2 \ln L(\alpha) + 2k \\ &= \chi^2(\alpha) + 2 \ln Z_D + 2k \\ &= \sum_{i=1}^{N_{data}} \left(\frac{x_i - model_i(\alpha)}{\sigma_i(\alpha)} \right)^2 \\ &+ 2 \sum_{i=1}^{N_{data}} \ln \sigma_i(\alpha) + \frac{N_{data}}{2} \ln 2\pi + 2k. \end{aligned} \quad (A3)$$

yeilding

$$\begin{aligned} AIC &= \sum_{i=1}^{N_{data}} \left(\frac{x_i - model_i}{\sigma_i} \right)^2 \\ &+ 2 \sum_{i=1}^{N_{data} - N_{outliers}} \ln \sigma_i(\alpha) \\ &+ 2 \sum_{i=1}^{N_{outliers}} \ln \sigma_{i,outlier}(\alpha) + \frac{N_{data}}{2} \ln 2\pi + 2k. \end{aligned} \quad (A4)$$

If outliers are defined as having $\sigma_{i,outlier} = f_{mult} \times \sigma_i$, then the $\sum_{i=1}^{N_{outliers}} \ln(\sigma_{i,outlier}) = N_{outliers} \ln(f_{mult}) + \sum_{i=1}^{N_{outliers}} \ln(\sigma_i)$, produces an additive term in AIC such that

$$\begin{aligned} AIC &= \chi^2 + 2 \sum_{i=1}^{N_{data}} \ln \sigma_i(\alpha) + 2 \ln(f_{mult}) N_{outliers} \\ &+ \frac{N_{data}}{2} \ln 2\pi + 2k. \end{aligned} \quad (A5)$$

and therefore

$$\begin{aligned} AIC_A - AIC_B &= (\chi_A^2 - \chi_B^2) \\ &+ (2 \ln(f_{mult}) (N_{A, outliers} - N_{B, outliers})) \\ &+ (2 k_A - 2 k_B) \end{aligned} \quad (A6)$$

If both models have the same number of parameters and both sets of data points are equal, meaning no distinction in outliers, then the AIC reduces to the difference in their χ^2 values. For small numbers of parameters, a correction term is included such that $AICc = AIC + 2k(k+1)/(N_{data} - k + 1)$, which in our case contributes a small correction and is included for completeness.

When comparing 2 models fitted to the SED data for one comet at one epoch, $model_A$ and $model_B$, with different number of outlier points ($N_{A, outliers}$, $N_{B, outliers}$) and potentially different numbers of parameters k_A and k_B , we define the difference $\Delta AICc \equiv AICc_A - AICc_B$ because the relative likelihood of $model_B$ with respect to $model_A$ is $\exp((\Delta AICc)/2)$. Hence,

$$\begin{aligned} \Delta AICc &= (\chi_A^2 - \chi_B^2) \\ &+ (2 \ln(f_{mult}) (N_{B, outliers} - N_{A, outliers})) \\ &+ (2 k_A - 2 k_B) \\ &+ \frac{(2 k_A(k_A + 1))}{(N_{A, data} - k_A + 1)} - \frac{(2 k_B(k_B + 1))}{(N_{B, data} - k_B + 1)} \end{aligned} \quad (A7)$$

For $model_B$, we have found that $f_{mult} \approx 20$ yields approximately the same χ_B^2 as omitting the points. Since we are using AIC that contains the partition function, we need to penalize the outlier points by increasing their uncertainties (an factor f_{mult}) that lessens the influence of these data points on the models).

Since outliers are decided from the original data set that has the same number of data points then the difference in the correction terms depends on the number of parameters in the two models and if equal then the correction terms cancel between the two models. If only $model_B$ has outliers and both models have the same number of parameters ($k_B = k_A$), then

$$\Delta AICc = (\chi_A^2) - (\chi_B^2 + 2 \ln(f_{mult})N_{B, outliers}) \quad (A8)$$

Considering a case where χ_B^2 is less than χ_A^2 by exactly the penalty term for the outliers of $2 \ln(f_{mult})N_{B, outliers}$, then $\Delta AICc$ is zero and the models have equal relative probability. In general, this functional form of $AICc$ assumes $model_A$ is associated with $AICc_{min}$. However, if χ_B^2 is yet lower than $(\chi_A^2) - 2 \ln(f_{mult})N_{B, outliers}$ then the $\Delta AICc > 0$ and relative likelihood is greater than unity and $model_B$ is more likely to hold more information, even though it holds fewer data points.

Let us compare comet 8P with $N_{data}=304$, $model_A=SLLL$ with $N_{A, outliers} = 0$ and $\chi_A^2 = 229.69$, and $model_B=SLLL-SL$ that is fitted to 159 data points such that $N_{B, outliers} = 145$ and $\chi_B^2 = 118.39$. Their χ^2 differ and their reduced- χ^2 are about equal (0.7708, 0.7738). We find $-\Delta AICc = (\chi_B^2 + 2 \ln(f_{mult})N_{B, outliers}) - (\chi_A^2) = (118.39 + 2 \ln(20) \times (145)) - (229.69) = (118.39 + 2 \times 3.00 \times 145) - 229.69 = (118.39 + 870) - 229.69 = 758.7$. For 8P, the probability of $model_B$ fitted to only the mid-infrared data SL compared to $model_A$ fitted to the full-wavelength data SLLL is $\exp(-\Delta AICc/2) = \exp(-379)$, which is really small. Omitting 145 data points can achieve a similar reduced- χ^2 but the information contained in the model fitted to data with 145 outliers (SLLL-SL that is chosen so as to only include SL1 and SL2) has less information content in comparison to the model fitted to all the available data points.

The AIC analysis is applied to the selection of data sets to be fitted by the thermal models for analyses as discussed in Section 4.5 and representative outcomes highlight in Table A1.

Table A1. $\Delta AIC_c = AIC_c(\text{SLLL}) - AIC_c(\text{SLLL-SL})$

Comet Name	Date Obs (UT)	ΔAIC_c
8P/Tuttle	2007-11-02	-757.5
9P/Tempel 1	2005-07-02	-486.5
9P/Tempel 1	2005-07-03	4.5
17P/Holmes	2007-11-10	468.2
37P/Forbes	2005-10-14	-566.5
46P/Wirtanen	2008-04-24	-578.9
46P/Wirtanen	2008-05-24	-594.7
46P/Wirtanen	2008-07-02	-597.6
48P/Johnson	2004-10-04	-775.5
67P/Churyumov-Gerasimenko	2008-11-30	-188.6
67P/Churyumov-Gerasimenko	2008-11-29	-213.9
67P/Churyumov-Gerasimenko	2008-11-29	-471.1
67P/Churyumov-Gerasimenko	2008-11-28	-198.8
71P/Clark	2006-05-27	-436.3
73P/Schwassmann-Wachmann 3 [B]	2006-08-06	-431.6
78P/Gehrels 2	2004-09-01	-494.0
88P/Howell	2004-09-01	-607.7
C/2004 B1 (LINEAR)	2006-07-26	-559.9
C/2006 P1 (McNaught)	2007-05-04	-301.8
C/2006 Q1 (McNaught)	2008-07-02	-725.7
C/2006 Q1 (McNaught)	2008-01-17	-824.6
C/2008 T2 (Cardinal)	2009-04-04	-470.7

Table A2. Comets Observed with SLLL and Only Modeled Over (SLLL-SL): Best-Fit Thermal Emission Model Parameters

Comet Name	N	M	a_p	α	D	Amorphous			Amorphous			Crystalline			χ^2_c
						Pyroxene	Olivine	Carbon	Pyroxene	Olivine	Carbon	Olivine	Orthopyroxene		
8P	3.4	6.8	0.3	2.857	6.659e + 01	+3.461e+02	0.000e + 00	+2.023e+02	6.845e + 03	+8.637e+01	2.880e + 02	+2.199e+02	1.010e + 03	+3.514e+02	0.77
9P-20050702	3.4	10.2	0.4	2.727	2.525e + 03	+2.306e+01	4.135e + 01	+3.077e+02	5.054e + 03	+5.989e+01	3.283e + 02	+2.572e+02	4.364e + 02	+5.046e+02	0.73
9P-20050703	3.5	14.0	0.5	2.727	1.604e + 03	+1.273e+02	0.000e + 00	+9.972e+01	3.393e + 03	+3.886e+01	1.941e + 02	+2.215e+02	3.783e + 02	+4.296e+02	0.59
17P	3.5	7.0	0.3	2.857	6.970e + 05	+4.803e+04	1.798e + 05	+2.620e+04	1.783e + 05	+5.546e+03	1.080e + 05	+1.653e+04	3.154e + 04	+3.116e+04	5.36
21P	3.6	14.4	0.5	2.727	7.449e + 02	+3.591e+01	0.000e + 00	+4.500e+01	1.138e + 03	+2.004e+01	1.078e + 02	+5.713e+01	0.000e + 00	+1.100e+02	0.50
29P	4.0	8.0	0.3	2.727	2.093e + 06	+3.186e+05	0.000e + 00	+2.742e+05	4.355e + 05	+3.982e+04	2.695e + 05	+1.385e+05	5.067e + 05	+3.815e+05	0.60
37P	3.4	10.2	0.4	2.727	3.279e + 02	+3.169e+01	9.612e + 00	+2.814e+01	4.322e + 02	+7.490e+00	4.180e + 01	+2.447e+01	3.140e + 01	+4.523e+01	1.79
46P-20080424	4.0	28.0	0.8	2.727	1.563e + 01	+7.437e+00	5.736e + 00	+4.397e+00	1.263e + 02	+9.310e+01	7.830e + 00	+1.526e+01	1.410e + 01	+1.870e+01	0.63
46P-20080524	4.3	43.0	1.1	2.727	1.923e + 01	+2.699e+00	0.000e + 00	+0.000e+00	1.310e + 02	+8.747e+01	0.000e + 00	+0.000e+00	6.564e + 01	+4.201e+01	1.55
46P-20080702	3.4	17.0	0.6	3.0	4.189e + 01	+8.498e+00	0.000e + 00	+1.430e+01	1.613e + 02	+8.525e+01	0.000e + 00	+2.626e+00	1.542e + 01	+1.940e+01	2.35
48P	3.8	19.0	0.6	2.727	1.277e + 03	+3.784e+02	1.036e + 02	+2.389e+02	1.992e + 03	+8.253e+01	3.746e + 02	+2.357e+02	4.036e + 02	+5.502e+02	0.66
65P	3.3	26.4	0.9	3.0	6.573e + 02	+5.040e+01	0.000e + 00	+0.000e+00	1.316e + 02	+3.471e+01	0.000e + 00	+0.000e+00	0.000e + 00	+1.714e+02	2.48
67P-20081128.38	4.3	43.0	1.1	2.727	1.184e + 02	+5.697e+00	0.000e + 00	+0.000e+00	1.942e + 02	+3.105e+00	0.000e + 00	+3.306e+01	0.000e + 00	+9.067e+01	1.38
67P-20081129.11	4.2	42.0	1.1	2.727	7.895e + 01	+5.708e+00	0.000e + 00	+6.333e+00	1.617e + 02	+2.886e+00	2.307e + 01	+5.032e+01	3.606e + 01	+1.063e+02	0.49
67P-20081129.70	4.3	47.3	1.2	2.727	7.663e + 01	+4.425e+00	0.000e + 00	+0.000e+00	1.402e + 02	+2.008e+00	0.000e + 00	+2.307e+01	4.907e + 01	+1.222e+02	0.88
67P-20081130.48	4.2	42.0	1.1	2.727	8.305e + 01	+4.480e+00	0.000e + 00	+0.000e+00	1.718e + 02	+2.653e+00	5.067e + 00	+5.545e+01	1.129e + 01	+1.052e+02	0.78
71P	4.3	30.1	0.8	2.727	2.225e + 02	+9.586e+01	5.810e + 01	+5.672e+01	1.833e + 03	+1.251e+01	7.017e + 01	+1.088e+02	2.381e + 02	+2.038e+02	0.89
73P(B)-20060806.18	3.5	10.5	0.4	2.727	1.569e + 02	+6.229e+00	0.000e + 00	+0.000e+00	3.498e + 02	+2.443e+00	1.150e + 01	+9.362e+00	0.000e + 00	+8.785e+00	1.75
78P	4.3	43.0	1.1	2.727	1.169e + 03	+8.371e+01	0.000e + 00	+3.097e+01	2.099e + 03	+2.887e+01	5.010e + 02	+4.749e+02	1.199e + 03	+9.488e+02	1.00
88P	3.3	19.8	0.7	3.0	2.924e + 02	+2.888e+01	0.000e + 00	+4.504e+01	5.520e + 02	+2.146e+01	2.157e + 01	+6.102e+01	2.265e + 02	+9.263e+01	0.79
132P	3.3	33.0	1.1	2.609	6.374e + 00	+3.495e+00	6.364e - 01	+2.661e+00	9.691e + 00	+8.236e-01	0.000e + 00	+3.044e+01	6.645e + 01	+9.345e+01	0.61
C2003K4-20050913	3.4	40.8	1.3	3.0	4.892e + 03	+3.149e+02	0.000e + 00	+0.000e+00	2.858e + 03	+1.992e+02	0.000e + 00	+1.755e+03	0.000e + 00	+2.627e+02	3.45
C2003T3	3.6	36.0	1.1	2.727	2.164e + 02	+6.347e+01	0.000e + 00	+3.920e+01	6.243e + 02	+3.110e+01	1.629e + 02	+4.262e+02	8.271e + 02	+9.748e+02	0.81
C2003T4-20051122	3.4	23.8	0.8	2.857	0.000e + 00	+0.000e+00	4.913e + 02	+7.809e+01	2.057e + 03	+5.366e+01	1.450e + 03	+3.605e+02	1.423e + 03	+5.538e+02	5.04
C2003T4-20060129	3.3	29.7	1.0	2.857	6.020e + 02	+2.255e+02	0.000e + 00	+0.000e+00	1.303e + 03	+1.346e+02	3.139e + 02	+6.151e+02	4.487e + 03	+1.215e+03	3.54
C2004B1-20060726	3.3	23.1	0.8	3.0	5.372e + 02	+3.374e+01	0.000e + 00	+0.000e+00	3.306e + 02	+2.541e+01	2.460e + 00	+7.997e+01	3.747e + 01	+1.226e+02	1.39
C2004B1-20070308	3.3	33.0	1.1	2.857	0.000e + 00	+2.127e+02	6.743e + 00	+1.498e+02	1.533e + 03	+2.528e+01	0.000e + 00	+0.000e+00	1.919e + 03	+1.739e+03	1.26
C2006P1-20070504	3.9	35.1	1.0	2.727	2.313e + 03	+2.109e+02	0.000e + 00	+1.375e+02	8.186e + 03	+6.031e+01	1.173e + 03	+1.539e+03	3.946e + 03	+2.773e+03	0.97
C2006P1-20070802	3.3	26.4	0.9	3.0	2.762e + 03	+1.179e+03	6.453e + 02	+6.356e+02	1.954e + 03	+1.971e+02	1.911e + 03	+9.285e+02	1.524e + 03	+1.486e+03	2.08
C2006P1-20070906	3.3	36.3	1.2	3.0	0.000e + 00	+5.046e+02	1.657e + 03	+1.549e+01	0.000e + 00	+0.000e+00	0.000e + 00	+8.857e+02	1.466e + 03	+1.972e+03	8.44

Table A2 continued

Table A2 (continued)

Comet Name	N	M	a_p^a	D	Amorphous				Crystalline		χ^2_{ν}
					Pyroxene	Olivine	Carbon	Olivine	Olivine	Orthopyroxene	
C2006Q1-20080117	3.3	26.4	0.9	2.857	$7.906e + 02^{+1.990e+02}_{-1.906e+02}$	$0.000e + 00^{+4.059e+02}_{-0.000e+00}$	2.943e + 03 ^{+2.117e+02} _{-1.178e+02}	$3.815e + 02^{+7.693e+02}_{-3.815e+02}$	$4.240e + 02^{+1.229e+03}_{-4.240e+02}$	1.08	
C2006Q1-20080702	3.3	23.1	0.8	3.0	1.628e + 03 ^{+5.376e+02} _{-5.509e+02}	3.930e + 02 ^{+3.314e+02} _{-3.305e+02}	2.471e + 03 ^{+7.833e+01} _{-7.808e+01}	6.524e + 02 ^{+4.946e+02} _{-4.928e+02}	1.331e + 03 ^{+7.770e+02} _{-7.930e+02}	1.16	
C2008T2	3.9	27.3	0.8	2.727	8.959e + 01 ^{+1.729e+01} _{-3.597e+01}	$2.387e + 00^{+1.866e+01}_{-2.387e+00}$	6.202e + 02 ^{+6.374e+00} _{-5.568e+00}	$1.885e + 01^{+4.254e+01}_{-1.885e+01}$	$5.143e + 01^{+8.455e+01}_{-5.143e+01}$	0.79	

NOTE— Bold values indicate values constrained to a confidence level of 95%.

^a Derived parameter.

Table A3. Comets Observed with SLLL and Only Modeled Over (SLLL-SL): Mass of Submicron Grains

Comet Name	Total Mass ($\times 10^7$ kg)	Mass Relative to Total Mass						Silicate/Carbon Ratio	f_{cryst}^a
		Amorphous Pyroxene	Amorphous Olivine	Amorphous Carbon	Crystalline Olivine	Crystalline Orthopyroxene			
8P	$3.414e + 04^{+3.094e+03}_{-3.414e+04}$	$0.014^{+0.076}_{-0.014}$	$0.000^{+0.046}_{-0.000}$	$0.638^{+0.093}_{-0.057}$	$0.077^{+0.057}_{-0.067}$	$0.271^{+0.072}_{-0.134}$	$0.568^{+0.154}_{-0.200}$	$0.962^{+0.038}_{-0.255}$	
9P-20050702	$5.974e + 04^{+8.005e+03}_{-5.974e+04}$	$0.409^{+0.081}_{-0.081}$	$0.007^{+0.057}_{-0.007}$	$0.372^{+0.071}_{-0.044}$	$0.091^{+0.063}_{-0.082}$	$0.121^{+0.111}_{-0.121}$	$1.685^{+0.358}_{-0.432}$	$0.337^{+0.149}_{-0.240}$	
9P-20050703	$5.470e + 04^{+9.963e+03}_{-5.470e+04}$	$0.388^{+0.102}_{-0.086}$	$0.000^{+0.026}_{-0.000}$	$0.373^{+0.075}_{-0.057}$	$0.081^{+0.082}_{-0.081}$	$0.158^{+0.134}_{-0.158}$	$1.682^{+0.487}_{-0.450}$	$0.381^{+0.171}_{-0.265}$	
17P	$7.719e + 06^{+2.460e+03}_{-7.719e+06}$	$0.611^{+0.033}_{-0.032}$	$0.158^{+0.030}_{-0.028}$	$0.071^{+0.005}_{-0.004}$	$0.124^{+0.016}_{-0.017}$	$0.036^{+0.033}_{-0.036}$	$13.072^{+0.900}_{-0.883}$	$0.173^{+0.038}_{-0.040}$	
21P	$1.896e + 04^{+3.457e+05}_{-1.896e+04}$	$0.514^{+0.039}_{-0.099}$	$0.000^{+0.032}_{-0.000}$	$0.357^{+0.029}_{-0.040}$	$0.129^{+0.055}_{-0.068}$	$0.000^{+0.124}_{-0.000}$	$1.800^{+0.349}_{-0.210}$	$0.200^{+0.179}_{-0.091}$	
29P	$1.621e + 07^{+1.971e+06}_{-1.621e+07}$	$0.585^{+0.157}_{-0.165}$	$0.000^{+0.093}_{-0.000}$	$0.055^{+0.017}_{-0.007}$	$0.125^{+0.063}_{-0.068}$	$0.235^{+0.147}_{-0.186}$	$17.071^{+2.720}_{-4.238}$	$0.381^{+0.147}_{-0.191}$	
37P	$6.372e + 03^{+7.870e+02}_{-6.372e+03}$	$0.498^{+0.078}_{-0.082}$	$0.015^{+0.048}_{-0.015}$	$0.299^{+0.044}_{-0.032}$	$0.107^{+0.054}_{-0.064}$	$0.081^{+0.099}_{-0.081}$	$2.350^{+0.408}_{-0.430}$	$0.269^{+0.133}_{-0.161}$	
46P-20080424	$2.055e + 03^{+7.159e+02}_{-2.055e+03}$	$0.133^{+0.075}_{-0.062}$	$0.049^{+0.075}_{-0.041}$	$0.488^{+0.192}_{-0.126}$	$0.118^{+0.112}_{-0.118}$	$0.212^{+0.173}_{-0.212}$	$1.049^{+0.710}_{-0.578}$	$0.645^{+0.161}_{-0.460}$	
46P-20080524	$2.701e + 03^{+1.079e+03}_{-2.701e+03}$	$0.098^{+0.072}_{-0.037}$	$0.000^{+0.000}_{-0.000}$	$0.303^{+0.171}_{-0.086}$	$0.000^{+0.127}_{-0.000}$	$0.599^{+0.112}_{-0.261}$	$2.302^{+1.311}_{-1.190}$	$0.860^{+0.182}_{-0.182}$	
46P-20080702	$3.644e + 03^{+4.239e+02}_{-3.644e+03}$	$0.321^{+0.081}_{-0.204}$	$0.000^{+0.125}_{-0.000}$	$0.561^{+0.117}_{-0.058}$	$0.000^{+0.020}_{-0.000}$	$0.118^{+0.122}_{-0.118}$	$0.782^{+0.207}_{-0.308}$	$0.269^{+0.246}_{-0.269}$	
48P	$5.693e + 04^{+1.488e+04}_{-5.693e+04}$	$0.350^{+0.164}_{-0.155}$	$0.028^{+0.085}_{-0.028}$	$0.249^{+0.083}_{-0.049}$	$0.179^{+0.088}_{-0.108}$	$0.193^{+0.182}_{-0.193}$	$3.024^{+0.996}_{-1.008}$	$0.496^{+0.190}_{-0.282}$	
65P	$2.192e + 04^{+4.661e+03}_{-2.192e+04}$	$0.917^{+0.021}_{-0.196}$	$0.000^{+0.000}_{-0.000}$	$0.083^{+0.025}_{-0.023}$	$0.000^{+0.000}_{-0.000}$	$0.000^{+0.198}_{-0.000}$	$10.986^{+4.598}_{-2.754}$	$0.000^{+0.215}_{-0.000}$	
67P-20081128.38	$2.838e + 03^{+2.275e+03}_{-2.838e+03}$	$0.573^{+0.014}_{-0.270}$	$0.000^{+0.000}_{-0.000}$	$0.427^{+0.014}_{-0.189}$	$0.000^{+0.210}_{-0.000}$	$0.000^{+0.441}_{-0.000}$	$1.341^{+1.860}_{-0.076}$	$0.000^{+0.602}_{-0.000}$	
67P-20081129.11	$3.572e + 03^{+2.926e+03}_{-3.572e+03}$	$0.305^{+0.223}_{-0.155}$	$0.000^{+0.028}_{-0.000}$	$0.284^{+0.193}_{-0.127}$	$0.160^{+0.251}_{-0.160}$	$0.250^{+0.335}_{-0.250}$	$2.518^{+2.841}_{-1.421}$	$0.573^{+0.246}_{-0.573}$	
67P-20081129.70	$2.705e + 03^{+2.864e+03}_{-2.705e+03}$	$0.335^{+0.224}_{-0.183}$	$0.000^{+0.000}_{-0.000}$	$0.279^{+0.177}_{-0.142}$	$0.000^{+0.315}_{-0.000}$	$0.386^{+0.296}_{-0.386}$	$2.590^{+3.757}_{-1.393}$	$0.536^{+0.288}_{-0.536}$	
67P-20081130.48	$2.632e + 03^{+2.981e+03}_{-2.632e+03}$	$0.436^{+0.092}_{-0.247}$	$0.000^{+0.000}_{-0.000}$	$0.410^{+0.082}_{-0.217}$	$0.048^{+0.319}_{-0.048}$	$0.106^{+0.440}_{-0.106}$	$1.440^{+2.746}_{-0.405}$	$0.261^{+0.504}_{-0.261}$	
71P	$2.882e + 04^{+7.508e+03}_{-2.882e+04}$	$0.134^{+0.068}_{-0.059}$	$0.035^{+0.048}_{-0.035}$	$0.502^{+0.162}_{-0.104}$	$0.075^{+0.093}_{-0.075}$	$0.254^{+0.134}_{-0.208}$	$0.992^{+0.520}_{-0.485}$	$0.661^{+0.137}_{-0.360}$	
73P(B)-20060806.18	$3.189e + 03^{+1.691e+02}_{-3.189e+03}$	$0.468^{+0.030}_{-0.035}$	$0.000^{+0.000}_{-0.000}$	$0.474^{+0.021}_{-0.024}$	$0.058^{+0.043}_{-0.048}$	$0.000^{+0.043}_{-0.000}$	$1.110^{+0.112}_{-0.088}$	$0.111^{+0.096}_{-0.088}$	
78P	$7.107e + 04^{+2.704e+04}_{-7.107e+04}$	$0.226^{+0.157}_{-0.072}$	$0.000^{+0.006}_{-0.000}$	$0.184^{+0.112}_{-0.050}$	$0.174^{+0.140}_{-0.171}$	$0.416^{+0.163}_{-0.295}$	$4.424^{+2.019}_{-2.049}$	$0.723^{+0.099}_{-0.270}$	
88P	$2.427e + 04^{+2.946e+03}_{-2.427e+04}$	$0.369^{+0.071}_{-0.095}$	$0.000^{+0.063}_{-0.000}$	$0.317^{+0.052}_{-0.033}$	$0.027^{+0.072}_{-0.027}$	$0.286^{+0.081}_{-0.108}$	$2.154^{+0.365}_{-0.446}$	$0.459^{+0.113}_{-0.144}$	
132P	$1.865e + 03^{+2.639e+03}_{-1.865e+03}$	$0.039^{+0.598}_{-0.039}$	$0.004^{+0.101}_{-0.004}$	$0.027^{+0.313}_{-0.015}$	$0.000^{+0.540}_{-0.000}$	$0.931^{+0.044}_{-0.931}$	$36.293^{+48.777}_{-34.353}$	$0.956^{+0.035}_{-0.956}$	
C2003K4-20050913	$1.236e + 05^{+3.623e+04}_{-1.236e+05}$	$0.790^{+0.020}_{-0.190}$	$0.000^{+0.000}_{-0.000}$	$0.210^{+0.023}_{-0.047}$	$0.000^{+0.223}_{-0.000}$	$0.000^{+0.040}_{-0.000}$	$3.767^{+1.379}_{-0.464}$	$0.000^{+0.280}_{-0.000}$	
C2003T3	$3.256e + 04^{+2.996e+04}_{-3.256e+04}$	$0.095^{+0.288}_{-0.067}$	$0.000^{+0.019}_{-0.000}$	$0.125^{+0.277}_{-0.057}$	$0.128^{+0.277}_{-0.128}$	$0.652^{+0.184}_{-0.652}$	$7.012^{+6.837}_{-5.523}$	$0.891^{+0.075}_{-0.540}$	
C2003T4-20051122	$1.231e + 05^{+2.142e+04}_{-1.231e+05}$	$0.000^{+0.000}_{-0.000}$	$0.093^{+0.036}_{-0.025}$	$0.176^{+0.036}_{-0.025}$	$0.369^{+0.072}_{-0.067}$	$0.362^{+0.082}_{-0.108}$	$4.670^{+0.921}_{-0.968}$	$0.887^{+0.032}_{-0.050}$	
C2003T4-20060129	$1.630e + 05^{+4.014e+04}_{-1.630e+05}$	$0.078^{+0.054}_{-0.040}$	$0.000^{+0.000}_{-0.000}$	$0.077^{+0.017}_{-0.012}$	$0.055^{+0.092}_{-0.055}$	$0.790^{+0.066}_{-0.088}$	$11.991^{+2.384}_{-2.312}$	$0.915^{+0.044}_{-0.060}$	
C2004B1-20060726	$2.282e + 04^{+4.205e+03}_{-2.282e+04}$	$0.739^{+0.057}_{-0.147}$	$0.000^{+0.000}_{-0.000}$	$0.207^{+0.023}_{-0.031}$	$0.003^{+0.100}_{-0.003}$	$0.052^{+0.137}_{-0.052}$	$3.840^{+0.867}_{-0.483}$	$0.069^{+0.205}_{-0.069}$	
C2004B1-20070308	$6.364e + 04^{+4.541e+04}_{-6.364e+04}$	$0.000^{+0.136}_{-0.000}$	$0.002^{+0.158}_{-0.002}$	$0.211^{+0.724}_{-0.089}$	$0.000^{+0.000}_{-0.000}$	$0.787^{+0.090}_{-0.787}$	$3.740^{+3.490}_{-3.677}$	0.997^{+nan}_{nan}	
C2006P1-20070504	$2.383e + 05^{+8.932e+04}_{-2.383e+05}$	$0.152^{+0.103}_{-0.051}$	$0.000^{+0.010}_{-0.000}$	$0.245^{+0.143}_{-0.066}$	$0.138^{+0.150}_{-0.138}$	$0.464^{+0.155}_{-0.269}$	$3.079^{+1.517}_{-1.502}$	$0.798^{+0.077}_{-0.219}$	
C2006P1-20070802	$2.364e + 05^{+6.120e+04}_{-2.364e+05}$	$0.357^{+0.130}_{-0.130}$	$0.083^{+0.123}_{-0.083}$	$0.115^{+0.046}_{-0.028}$	$0.247^{+0.100}_{-0.106}$	$0.197^{+0.126}_{-0.195}$	$7.703^{+2.826}_{-2.495}$	$0.502^{+0.106}_{-0.171}$	
C2006P1-20070906	$7.249e + 04^{+5.180e+04}_{-7.249e+04}$	$0.000^{+0.119}_{-0.000}$	$0.531^{+0.427}_{-0.267}$	$0.000^{+0.000}_{-0.000}$	$0.000^{+0.241}_{-0.000}$	$0.469^{+0.194}_{-0.469}$	inf^{+nan}_{nan}	$0.469^{+0.210}_{-0.454}$	
C2006Q1-20080117	$7.276e + 04^{+4.321e+04}_{-7.276e+04}$	$0.246^{+0.158}_{-0.246}$	$0.000^{+0.173}_{-0.000}$	$0.416^{+0.249}_{-0.145}$	$0.160^{+0.223}_{-0.160}$	$0.178^{+0.300}_{-0.178}$	$1.405^{+1.283}_{-0.901}$	$0.579^{+0.315}_{-0.579}$	
C2006Q1-20080702	$1.609e + 05^{+3.166e+04}_{-1.609e+05}$	$0.317^{+0.090}_{-0.090}$	$0.077^{+0.091}_{-0.066}$	$0.219^{+0.058}_{-0.037}$	$0.127^{+0.080}_{-0.092}$	$0.260^{+0.098}_{-0.132}$	$3.565^{+0.942}_{-0.961}$	$0.495^{+0.098}_{-0.160}$	
C2008T2	$8.726e + 03^{+2.809e+03}_{-8.726e+03}$	$0.180^{+0.082}_{-0.081}$	$0.005^{+0.045}_{-0.005}$	$0.566^{+0.179}_{-0.136}$	$0.067^{+0.125}_{-0.067}$	$0.183^{+0.197}_{-0.183}$	$0.768^{+0.558}_{-0.425}$	$0.575^{+0.220}_{-0.575}$	

^a Defined as $f_{silicates}^{cryst} \equiv (\text{crystalline})/(\text{crystalline} + \text{amorphous})$.

REFERENCES

- A'Hearn, M. F., Millis, R. C., Schleicher, D. O., Osip, D. J., & Birch, P. V. 1995, *Icarus*, 118, 223, doi: [10.1006/icar.1995.1190](https://doi.org/10.1006/icar.1995.1190)
- Arakawa, S., Matsumoto, Y., & Honda, M. 2021, *ApJ*, 920, 27, doi: [10.3847/1538-4357/ac157e](https://doi.org/10.3847/1538-4357/ac157e)
- Astropy Collaboration, Price-Whelan, A. M., Sipőcz, B. M., et al. 2018, *AJ*, 156, 123, doi: [10.3847/1538-3881/aabc4f](https://doi.org/10.3847/1538-3881/aabc4f)
- Audi, G., Kondev, F. G., Wang, M., Huang, W. J., & Naimi, S. 2017, *Chinese Physics C*, 41, 030001, doi: [10.1088/1674-1137/41/3/030001](https://doi.org/10.1088/1674-1137/41/3/030001)

- Bardyn, A., Baklouti, D., Cottin, H., et al. 2017, *MNRAS*, 469, S712, doi: [10.1093/mnras/stx2640](https://doi.org/10.1093/mnras/stx2640)
- Bockelée-Morvan, D., & Biver, N. 2017, *Philosophical Transactions of the Royal Society of London Series A*, 375, 20160252, doi: [10.1098/rsta.2016.0252](https://doi.org/10.1098/rsta.2016.0252)
- Bockelée-Morvan, D., Gautier, D., Hersant, F., Huré, J. M., & Robert, F. 2002, *A&A*, 384, 1107, doi: [10.1051/0004-6361:20020086](https://doi.org/10.1051/0004-6361:20020086)
- Bockelée-Morvan, D., Rinaldi, G., Erard, S., et al. 2017a, *MNRAS*, 469, S842, doi: [10.1093/mnras/sty533](https://doi.org/10.1093/mnras/sty533)
- . 2017b, *MNRAS*, 469, S443, doi: [10.1093/mnras/stx1950](https://doi.org/10.1093/mnras/stx1950)
- Bockelée-Morvan, D., Leyrat, C., Erard, S., et al. 2019, *A&A*, 630, A22, doi: [10.1051/0004-6361/201834764](https://doi.org/10.1051/0004-6361/201834764)
- Bohren, C. F., & Huffman, D. R. 1983, *Absorption and scattering of light by small particles*
- Bonev, B. P., Mumma, M. J., Villanueva, G. L., et al. 2007, *ApJL*, 661, L97, doi: [10.1086/518419](https://doi.org/10.1086/518419)
- Bradley, J. P. 1994, *Science*, 265, 925, doi: [10.1126/science.265.5174.925](https://doi.org/10.1126/science.265.5174.925)
- Bradley, J. P., & Ishii, H. A. 2008, *A&A*, 486, 781, doi: [10.1051/0004-6361:20078710](https://doi.org/10.1051/0004-6361:20078710)
- Bradley, J. P., Ishii, H. A., Bustillo, K., et al. 2022, *GeoCoA*, 335, 323, doi: [10.1016/j.gca.2022.06.036](https://doi.org/10.1016/j.gca.2022.06.036)
- Bradley, J. P., Keller, L. P., Snow, T. P., et al. 1999, *Science*, 285, 1716, doi: [10.1126/science.285.5434.1716](https://doi.org/10.1126/science.285.5434.1716)
- Brassé, C., Muñoz, O., Coll, P., & Raulin, F. 2015, *Planet. Space Sci.*, 109, 159, doi: [10.1016/j.pss.2015.02.012](https://doi.org/10.1016/j.pss.2015.02.012)
- Brownlee, D. 2014, *Annual Review of Earth and Planetary Sciences*, 42, 179, doi: [10.1146/annurev-earth-050212-124203](https://doi.org/10.1146/annurev-earth-050212-124203)
- Brownlee, D., Tsou, P., Aléon, J., et al. 2006, *Science*, 314, 1711, doi: [10.1126/science.1135840](https://doi.org/10.1126/science.1135840)
- Brownlee, D. E., & Joswiak, D. J. 2017, *M&PS*, 52, 471, doi: [10.1111/maps.12804](https://doi.org/10.1111/maps.12804)
- Brucato, J. R., Strazzulla, G., Baratta, G., & Colangeli, L. 2004, *A&A*, 413, 395, doi: [10.1051/0004-6361:20031574](https://doi.org/10.1051/0004-6361:20031574)
- Brunetto, R., Borg, J., Dartois, E., et al. 2011, *Icarus*, 212, 896, doi: [10.1016/j.icarus.2011.01.038](https://doi.org/10.1016/j.icarus.2011.01.038)
- Busemann, H., Nguyen, A. N., Cody, G. D., et al. 2009, *Earth and Planetary Science Letters*, 288, 44, doi: [10.1016/j.epsl.2009.09.007](https://doi.org/10.1016/j.epsl.2009.09.007)
- Carrez, P., Demyk, K., Cordier, P., et al. 2002a, *M&PS*, 37, 1599, doi: [10.1111/j.1945-5100.2002.tb00814.x](https://doi.org/10.1111/j.1945-5100.2002.tb00814.x)
- Carrez, P., Demyk, K., Leroux, H., et al. 2002b, *M&PS*, 37, 1615, doi: [10.1111/j.1945-5100.2002.tb00815.x](https://doi.org/10.1111/j.1945-5100.2002.tb00815.x)
- Carrez, P., Leroux, H., Cordier, P., & Guyot, F. 2001, *Meteoritics and Planetary Science Supplement*, 36, A37
- Chihara, H., Koike, C., & Tsuchiyama, A. 2001, *Publ. Astron. Soc. Japan*, 53, 243, doi: [10.1093/pasj/53.2.243](https://doi.org/10.1093/pasj/53.2.243)
- Chihara, H., Koike, C., Tsuchiyama, A., Tachibana, S., & Sakamoto, D. 2002, *A&A*, 391, 267, doi: [10.1051/0004-6361:20020791](https://doi.org/10.1051/0004-6361:20020791)
- Christoffersen, R., & Keller, L. P. 2011, *M&PS*, 46, 950, doi: [10.1111/j.1945-5100.2011.01203.x](https://doi.org/10.1111/j.1945-5100.2011.01203.x)
- Ciesla, F. J. 2010, *Icarus*, 208, 455, doi: [10.1016/j.icarus.2010.02.010](https://doi.org/10.1016/j.icarus.2010.02.010)
- de Gregorio, B. T., Stroud, R. M., Cody, G. D., et al. 2011, *M&PS*, 46, 1376, doi: [10.1111/j.1945-5100.2011.01237.x](https://doi.org/10.1111/j.1945-5100.2011.01237.x)
- De Gregorio, B. T., Stroud, R. M., Nittler, L. R., & Kilcoyne, A. L. D. 2017, *ApJ*, 848, 113, doi: [10.3847/1538-4357/aa8c07](https://doi.org/10.3847/1538-4357/aa8c07)
- Defouilloy, C., Nakashima, D., Joswiak, D. J., et al. 2016, in 47th Annual Lunar and Planetary Science Conference, Lunar and Planetary Science Conference, 1584
- Defouilloy, C., Nakashima, D., Joswiak, D. J., et al. 2017, *Earth and Planetary Science Letters*, 465, 145, doi: [10.1016/j.epsl.2017.02.045](https://doi.org/10.1016/j.epsl.2017.02.045)
- Dello Russo, N., Kawakita, H., Vervack, R. J., & Weaver, H. A. 2016, *Icarus*, 278, 301, doi: [10.1016/j.icarus.2016.05.039](https://doi.org/10.1016/j.icarus.2016.05.039)
- Demyk, K., d'Hendecourt, L., Leroux, H., Jones, A. P., & Borg, J. 2004, *A&A*, 420, 233, doi: [10.1051/0004-6361:20040091](https://doi.org/10.1051/0004-6361:20040091)
- Demyk, K., Carrez, P., Leroux, H., et al. 2001, *A&A*, 368, L38, doi: [10.1051/0004-6361:20010208](https://doi.org/10.1051/0004-6361:20010208)
- Demyk, K., Gromov, V., Meny, C., et al. 2022, *A&A*, 666, A192, doi: [10.1051/0004-6361/202243815](https://doi.org/10.1051/0004-6361/202243815)
- Do-Duy, T., Wright, C. M., Fujiyoshi, T., et al. 2020, *MNRAS*, 493, 4463, doi: [10.1093/mnras/staa396](https://doi.org/10.1093/mnras/staa396)
- Dobrić, E., Engrand, C., Leroux, H., Rouzard, J. N., & Duprat, J. 2012, *GeoCoA*, 76, 68, doi: [10.1016/j.gca.2011.10.025](https://doi.org/10.1016/j.gca.2011.10.025)
- Dorschner, J., Begemann, B., Henning, T., Jaeger, C., & Mutschke, H. 1995, *A&A*, 300, 503
- Dullemond, C. P., Apai, D., & Walch, S. 2006, *ApJL*, 640, L67, doi: [10.1086/503100](https://doi.org/10.1086/503100)
- Engrand, C., Lasue, J., Wooden, D. H., & Zolensky, M. E. 2023, *arXiv e-prints*, arXiv:2305.03417, doi: [10.48550/arXiv.2305.03417](https://doi.org/10.48550/arXiv.2305.03417)
- Fabian, D., Henning, T., Jäger, C., et al. 2001, *A&A*, 378, 228, doi: [10.1051/0004-6361:20011196](https://doi.org/10.1051/0004-6361:20011196)
- Flynn, G., Keller, L. P., Jacobsen, C., Wirick, S., & Miller, M. A. 2000, in *Astronomical Society of the Pacific Conference Series*, Vol. 213, *Bioastronomy 99*, ed. G. Lemarchand & K. Meech, 191
- Frank, D. R., Zolensky, M. E., & Le, L. 2014a, *GeoCoA*, 142, 240, doi: [10.1016/j.gca.2014.05.037](https://doi.org/10.1016/j.gca.2014.05.037)
- Frank, D. R., Westphal, A. J., Zolensky, M. E., et al. 2014b, *M&PS*, 49, 1522, doi: [10.1111/maps.12147](https://doi.org/10.1111/maps.12147)
- Fray, N., Bardyn, A., Cottin, H., et al. 2017, *MNRAS*, 469, S506, doi: [10.1093/mnras/stx2002](https://doi.org/10.1093/mnras/stx2002)
- Güttler, C., Mannel, T., Rotundi, A., et al. 2019, *A&A*, 630, A24, doi: [10.1051/0004-6361/201834751](https://doi.org/10.1051/0004-6361/201834751)

- Hanner, M. S., Lynch, D. K., & Russell, R. W. 1994, *ApJ*, 425, 274, doi: [10.1086/173984](https://doi.org/10.1086/173984)
- Hanner, M. S., Lynch, D. K., Russell, R. W., et al. 1996, *Icarus*, 124, 344, doi: [10.1006/icar.1996.0209](https://doi.org/10.1006/icar.1996.0209)
- Harker, D. E., Wooden, D. H., Woodward, C. E., & Lisse, C. M. 2002, *ApJ*, 580, 579, doi: [10.1086/343091](https://doi.org/10.1086/343091)
- . 2004, *ApJ*, 615, 1081, doi: [10.1086/424592](https://doi.org/10.1086/424592)
- Harker, D. E., Woodward, C. E., Kelley, M. S., et al. 2011, *AJ*, 141, 26, doi: [10.1088/0004-6256/141/1/26](https://doi.org/10.1088/0004-6256/141/1/26)
- Harker, D. E., Woodward, C. E., & Wooden, D. H. 2005, *Science*, 310, 278, doi: [10.1126/science.1119143](https://doi.org/10.1126/science.1119143)
- Harker, D. E., Woodward, C. E., Wooden, D. H., Fisher, R. S., & Trujillo, C. A. 2007, *Icarus*, 190, 432, doi: [10.1016/j.icarus.2007.03.008](https://doi.org/10.1016/j.icarus.2007.03.008)
- Harris, C. R., Millman, K. J., van der Walt, S. J., et al. 2020, *Nature*, 585, 357, doi: [10.1038/s41586-020-2649-2](https://doi.org/10.1038/s41586-020-2649-2)
- Hayward, T. L., Hanner, M. S., & Sekanina, Z. 2000, *ApJ*, 538, 428, doi: [10.1086/309117](https://doi.org/10.1086/309117)
- Henning, T. 2010, *ARA&A*, 48, 21, doi: [10.1146/annurev-astro-081309-130815](https://doi.org/10.1146/annurev-astro-081309-130815)
- Hensley, B. S., & Draine, B. T. 2021, *ApJ*, 906, 73, doi: [10.3847/1538-4357/abc8f1](https://doi.org/10.3847/1538-4357/abc8f1)
- Houck, J. R., Roellig, T. L., van Cleve, J., et al. 2004, *ApJS*, 154, 18, doi: [10.1086/423134](https://doi.org/10.1086/423134)
- Ishii, H. A., Bradley, J. P., Bechtel, H. A., et al. 2018, *Proceedings of the National Academy of Science*, 115, 6608, doi: [10.1073/pnas.1720167115](https://doi.org/10.1073/pnas.1720167115)
- Ivezić, Ž., Connolly, A. J., VanderPlas, J. T., & Gray, A. 2014, *Statistics, Data Mining, and Machine Learning in Astronomy: A Practical Python Guide for the Analysis of Survey Data*, doi: [10.1515/9781400848911](https://doi.org/10.1515/9781400848911)
- Jäger, C., Fabian, D., Schrempel, F., et al. 2003, *A&A*, 401, 57, doi: [10.1051/0004-6361:20030002](https://doi.org/10.1051/0004-6361:20030002)
- Jäger, C., Molster, F. J., Dorschner, J., et al. 1998, *A&A*, 339, 904
- Jäger, C., Sabri, T., Wendlner, E., & Henning, T. 2016, *ApJ*, 831, 66, doi: [10.3847/0004-637X/831/1/66](https://doi.org/10.3847/0004-637X/831/1/66)
- Joswiak, D. J., Brownlee, D. E., Nguyen, A. N., & Messenger, S. 2017, *M&PS*, 52, 1612, doi: [10.1111/maps.12877](https://doi.org/10.1111/maps.12877)
- Juhász, A., Henning, T., Bouwman, J., et al. 2009, *ApJ*, 695, 1024, doi: [10.1088/0004-637X/695/2/1024](https://doi.org/10.1088/0004-637X/695/2/1024)
- Keller, L. P., & Messenger, S. 2011, *GeoCoA*, 75, 5336, doi: [10.1016/j.gca.2011.06.040](https://doi.org/10.1016/j.gca.2011.06.040)
- . 2013, *GeoCoA*, 107, 341, doi: [10.1016/j.gca.2012.11.012](https://doi.org/10.1016/j.gca.2012.11.012)
- Keller, L. P., Messenger, S., Flynn, G. J., et al. 2004, *GeoCoA*, 68, 2577, doi: [10.1016/j.gca.2003.10.044](https://doi.org/10.1016/j.gca.2003.10.044)
- Keller, L. P., Thomas, K. L., & McKay, D. S. 1994, *Meteoritics*, 29, 480
- Kelley, M. S. P., Harker, D. E., Woodward, C. E., & Wooden, D. H. 2021, *NASA Planetary Data System*, 1, doi: [urn:nasa:pds:spitzer:spitzer-spec-comet::1.0](https://doi.org/urn:nasa:pds:spitzer:spitzer-spec-comet::1.0)
- Kelley, M. S. P., Woodward, C. E., Gehrz, R. D., Reach, W. T., & Harker, D. E. 2017, *Icarus*, 284, 344, doi: [10.1016/j.icarus.2016.11.029](https://doi.org/10.1016/j.icarus.2016.11.029)
- Kemper, F., Vriend, W. J., & Tielens, A. G. G. M. 2004, *ApJ*, 609, 826, doi: [10.1086/421339](https://doi.org/10.1086/421339)
- Klöck, W., & Stadermann, F. J. 1994, in *American Institute of Physics Conference Series*, Vol. 310, *Analysis of Interplanetary Dust Particles*, ed. E. Zolensky, T. L. Wilson, F. J. M. Rietmeijer, & G. J. Flynn, 51, doi: [10.1063/1.46523](https://doi.org/10.1063/1.46523)
- Koike, C., Chihara, H., Tsuchiyama, A., et al. 2003, *A&A*, 399, 1101, doi: [10.1051/0004-6361:20021831](https://doi.org/10.1051/0004-6361:20021831)
- Kolokolova, L., Hanner, M. S., Lvasseur-Regourd, A. C., & Gustafson, B. Å. S. 2004, in *Comets II*, ed. M. C. Festou, H. U. Keller, & H. A. Weaver, 577
- Kóspál, Á., Ábrahám, P., Diehl, L., et al. 2023, *ApJL*, 945, L7, doi: [10.3847/2041-8213/acb58a](https://doi.org/10.3847/2041-8213/acb58a)
- Lindsay, S. S., Wooden, D. H., Harker, D. E., et al. 2013, *ApJ*, 766, 54, doi: [10.1088/0004-637X/766/1/54](https://doi.org/10.1088/0004-637X/766/1/54)
- Lippi, M., Villanueva, G. L., Mumma, M. J., & Faggi, S. 2021, *AJ*, 162, 74, doi: [10.3847/1538-3881/abfdb7](https://doi.org/10.3847/1538-3881/abfdb7)
- Lisse, C. M., VanCleve, J., Adams, A. C., et al. 2006, *Science*, 313, 635, doi: [10.1126/science.1124694](https://doi.org/10.1126/science.1124694)
- Mannel, T., Bentley, M. S., Schmied, R., et al. 2016, *MNRAS*, 462, S304, doi: [10.1093/mnras/stw2898](https://doi.org/10.1093/mnras/stw2898)
- Matrajt, G., Muñoz Caro, G. M., Dartois, E., et al. 2005, *A&A*, 433, 979, doi: [10.1051/0004-6361:20041605](https://doi.org/10.1051/0004-6361:20041605)
- McClure, M. K., Rocha, W. R. M., Pontoppidan, K. M., et al. 2023, *Nature Astronomy*, 7, 431, doi: [10.1038/s41550-022-01875-w](https://doi.org/10.1038/s41550-022-01875-w)
- Mennella, V., Ciarniello, M., Raponi, A., et al. 2020, *ApJL*, 897, L37, doi: [10.3847/2041-8213/ab919e](https://doi.org/10.3847/2041-8213/ab919e)
- Min, M., Hovenier, J. W., de Koter, A., Waters, L. B. F. M., & Dominik, C. 2005, *Icarus*, 179, 158, doi: [10.1016/j.icarus.2005.05.015](https://doi.org/10.1016/j.icarus.2005.05.015)
- Min, M., Waters, L. B. F. M., de Koter, A., et al. 2008, *A&A*, 486, 779, doi: [10.1051/0004-6361:20065436e](https://doi.org/10.1051/0004-6361:20065436e)
- Moreno, F., Muñoz, O., Vilaplana, R., & Molina, A. 2003, *ApJ*, 595, 522, doi: [10.1086/377340](https://doi.org/10.1086/377340)
- Mumma, M. J., Disanti, M. A., Bonev, B. P., et al. 2011, in *42nd Annual Lunar and Planetary Science Conference, Lunar and Planetary Science Conference*, 2428
- Nakamura, T., Matsumoto, M., Amano, K., et al. 2023, *Science*, 379, abn8671, doi: [10.1126/science.abn8671](https://doi.org/10.1126/science.abn8671)
- Nakamura-Messenger, K., Messenger, S., Keller, L. P., Clemett, S. J., & Zolensky, M. E. 2006, *Science*, 314, 1439, doi: [10.1126/science.1132175](https://doi.org/10.1126/science.1132175)
- Ogliore, R. C., Westphal, A. J., Gainsforth, Z., et al. 2009, *M&PS*, 44, 1675, doi: [10.1111/j.1945-5100.2009.tb01198.x](https://doi.org/10.1111/j.1945-5100.2009.tb01198.x)
- Ogliore, R. C., Huss, G. R., Nagashima, K., et al. 2012, *ApJL*, 745, L19, doi: [10.1088/2041-8205/745/2/L19](https://doi.org/10.1088/2041-8205/745/2/L19)

- Olofsson, J., Augereau, J. C., van Dishoeck, E. F., et al. 2010, *A&A*, 520, A39, doi: [10.1051/0004-6361/200913909](https://doi.org/10.1051/0004-6361/200913909)
- Pedregosa, F., Varoquaux, G., Gramfort, A., et al. 2011, *Journal of Machine Learning Research*, 12, 2825, doi: [10.48550/arXiv.1201.0490](https://doi.org/10.48550/arXiv.1201.0490)
- Possolo, A., Merktas, C., & Bodnar, O. 2019, *Metrologia*, 56, 045009, doi: [10.1088/1681-7575/ab2a8d](https://doi.org/10.1088/1681-7575/ab2a8d)
- Reach, W. T., Vaubaillon, J., Lisse, C. M., Holloway, M., & Rho, J. 2010, *Icarus*, 208, 276, doi: [10.1016/j.icarus.2010.01.020](https://doi.org/10.1016/j.icarus.2010.01.020)
- Rietmeijer, F. J. M. 2009, *ApJ*, 705, 791, doi: [10.1088/0004-637X/705/1/791](https://doi.org/10.1088/0004-637X/705/1/791)
- Rinaldi, G., Della Corte, V., Fulle, M., et al. 2017, *MNRAS*, 469, S598, doi: [10.1093/mnras/stx1873](https://doi.org/10.1093/mnras/stx1873)
- Sansberro, I., Fray, N., Cottin, H., et al. 2022, in 44th COSPAR Scientific Assembly. Held 16-24 July, Vol. 44, 175
- Sargent, B., Forrest, W. J., D'Alessio, P., et al. 2006, *ApJ*, 645, 395, doi: [10.1086/504283](https://doi.org/10.1086/504283)
- Seabold, S., & Perktold, J. 2010, in *Proceedings of the 9th Python in Science Conference*, ed. Stéfan van der Walt & Jarrod Millman, 92 – 96, doi: [10.25080/Majora-92bf1922-011](https://doi.org/10.25080/Majora-92bf1922-011)
- Shanklin, J. D. 1995, *Journal of the British Astronomical Association*, 105, 295
- Silsbee, K., & Draine, B. T. 2016, *ApJ*, 818, 133, doi: [10.3847/0004-637X/818/2/133](https://doi.org/10.3847/0004-637X/818/2/133)
- Sitko, M. L., Lynch, D. K., Russell, R. W., & Hanner, M. S. 2004, *ApJ*, 612, 576, doi: [10.1086/421991](https://doi.org/10.1086/421991)
- Sugita, S., Ootsubo, T., Kadono, T., et al. 2005, *Science*, 310, 274, doi: [10.1126/science.1119091](https://doi.org/10.1126/science.1119091)
- Szenes, G., Kovács, V. K., Pécz, B., & Skuratov, V. 2010, *ApJ*, 708, 288, doi: [10.1088/0004-637X/708/1/288](https://doi.org/10.1088/0004-637X/708/1/288)
- Thomas, K. L., Blanford, G. E., Keller, L. P., Klock, W., & McKay, D. S. 1993a, *GeoCoA*, 57, 1551, doi: [10.1016/0016-7037\(93\)90012-L](https://doi.org/10.1016/0016-7037(93)90012-L)
- Thomas, K. L., Keller, L. P., Blanford, G. E., & McKay, D. S. 1994, in *American Institute of Physics Conference Series*, Vol. 310, *Analysis of Interplanetary Dust Particles*, ed. E. Zolensky, T. L. Wilson, F. J. M. Rietmeijer, & G. J. Flynn, 165, doi: [10.1063/1.46532](https://doi.org/10.1063/1.46532)
- Thomas, K. L., Klock, W., Keller, L. P., Blanford, G. E., & McKay, D. S. 1993b, *Meteoritics*, 28, 448
- Tsuchikawa, T., Kaneda, H., Oyabu, S., et al. 2022, *ApJ*, 941, 50, doi: [10.3847/1538-4357/ac9b23](https://doi.org/10.3847/1538-4357/ac9b23)
- van Breemen, J. M., Min, M., Chiar, J. E., et al. 2011, *A&A*, 526, A152, doi: [10.1051/0004-6361/200811142](https://doi.org/10.1051/0004-6361/200811142)
- Virtanen, P., Gommers, R., Oliphant, T. E., et al. 2020, *Nature Methods*, 17, 261, doi: [10.1038/s41592-019-0686-2](https://doi.org/10.1038/s41592-019-0686-2)
- Werner, M., Fazio, G., Rieke, G., Roellig, T. L., & Watson, D. M. 2006, *ARA&A*, 44, 269, doi: [10.1146/annurev.astro.44.051905.092544](https://doi.org/10.1146/annurev.astro.44.051905.092544)
- Werner, M. W., Roellig, T. L., Low, F. J., et al. 2004, *ApJS*, 154, 1, doi: [10.1086/422992](https://doi.org/10.1086/422992)
- Wirick, S., Flynn, G. J., Keller, L. P., et al. 2009, *M&PS*, 44, 1611, doi: [10.1111/j.1945-5100.2009.tb01194.x](https://doi.org/10.1111/j.1945-5100.2009.tb01194.x)
- Wooden, D., Desch, S., Harker, D., Gail, H. P., & Keller, L. 2007, in *Protostars and Planets V*, ed. B. Reipurth, D. Jewitt, & K. Keil, 815
- Wooden, D. H. 2008, *SSRv*, 138, 75, doi: [10.1007/s11214-008-9424-2](https://doi.org/10.1007/s11214-008-9424-2)
- Wooden, D. H., Butner, H. M., Harker, D. E., & Woodward, C. E. 2000, *Icarus*, 143, 126, doi: [10.1006/icar.1999.6240](https://doi.org/10.1006/icar.1999.6240)
- Wooden, D. H., Harker, D. E., Woodward, C. E., et al. 1999, *ApJ*, 517, 1034, doi: [10.1086/307206](https://doi.org/10.1086/307206)
- Wooden, D. H., Ishii, H. A., & Zolensky, M. E. 2017, *Philosophical Transactions of the Royal Society of London Series A*, 375, 20160260, doi: [10.1098/rsta.2016.0260](https://doi.org/10.1098/rsta.2016.0260)
- Wooden, D. H., Woodward, C. E., & Harker, D. E. 2004, *ApJL*, 612, L77, doi: [10.1086/424593](https://doi.org/10.1086/424593)
- Woodward, C. E., Bockelee-Morvan, D., Harker, D. E., et al. 2023, in *American Astronomical Society Meeting Abstracts*, Vol. 55, *American Astronomical Society Meeting Abstracts*, 136.06
- Woodward, C. E., Wooden, D. H., Harker, D. E., et al. 2021, *Planetary Sci. J.*, 2, 25, doi: [10.3847/PSJ/abca3e](https://doi.org/10.3847/PSJ/abca3e)
- Yang, L., & Ciesla, F. J. 2012, *M&PS*, 47, 99, doi: [10.1111/j.1945-5100.2011.01315.x](https://doi.org/10.1111/j.1945-5100.2011.01315.x)
- Zolensky, M. E., & Barrett, R. 1994, in *Analysis of Interplanetary Dust Particles*, ed. M. E. Zolensky, 54